UNIVERSITAT POLITÈCNICA
DE CATALUNYA
BARCELONATECH

Atomic imaging of complex molecular structures with laser-induced electron diffraction

Xinyao Liu

ADVERTIMENT La consulta d'aquesta tesi queda condicionada a l'acceptació de les següents condicions d'ús: La difusió d'aquesta tesi per mitjà del repositori institucional UPCommons (http://upcommons.upc.edu/tesis) i el repositori cooperatiu TDX (http://www.tdx.cat/) ha estat autoritzada pels titulars dels drets de propietat intel·lectual **únicament per a usos privats** emmarcats en activitats d'investigació i docència. No s'autoritza la seva reproducció amb finalitats de lucre ni la seva difusió i posada a disposició des d'un lloc aliè al servei UPCommons o TDX. No s'autoritza la presentació del seu contingut en una finestra o marc aliè a UPCommons (*framing*). Aquesta reserva de drets afecta tant al resum de presentació de la tesi com als seus continguts. En la utilització o cita de parts de la tesi és obligat indicar el nom de la persona autora.

ADVERTENCIA La consulta de esta tesis queda condicionada a la aceptación de las siguientes condiciones de uso: La difusión de esta tesis por medio del repositorio institucional UPCommons (http://upcommons.upc.edu/tesis) y el repositorio cooperativo TDR (http://www.tdx.cat/?locale-attribute=es) ha sido autorizada por los titulares de los derechos de propiedad intelectual **únicamente para usos privados enmarcados** en actividades de investigación y docencia. No se autoriza su reproducción con finalidades de lucro ni su difusión y puesta a disposición desde un sitio ajeno al servicio UPCommons No se autoriza la presentación de su contenido en una ventana o marco ajeno a UPCommons (*framing)*. Esta reserva de derechos afecta tanto al resumen de presentación de la tesis como a sus contenidos. En la utilización o cita de partes de la tesis es obligado indicar el nombre de la persona autora.

WARNING On having consulted this thesis you're accepting the following use conditions: Spreading this thesis by the institutional repository UPCommons (http://upcommons.upc.edu/tesis) and the cooperative repository TDX (http://www.tdx.cat/?locale- attribute=en) has been authorized by the titular of the intellectual property rights **only for private uses** placed in investigation and teaching activities. Reproduction with lucrative aims is not authorized neither its spreading nor availability from a site foreign to the UPCommons service. Introducing its content in a window or frame foreign to the UPCommons service is not authorized (framing). These rights affect to the presentation summary of the thesis as well as to its contents. In the using or citation of parts of the thesis it's obliged to indicate the name of the author.

Atomic imaging of complex molecular structures with laser-induced electron diffraction

DISSERTATION

submitted in partial fulfilment of the
requirements for the degree of
Doctor of Philosophy
by

Xinyao Liu

ICFO - Institut de Ciències Fotòniques
UPC - Universitat Politècnica de Catalunya
Thesis Advisor: Prof. Dr. Jens Biegert

Thesis committee:
1) Prof. Rosario Gonzalez-Ferez
2) Prof. Maciej Lewenstein
3) Prof. Stefanie Gräfe

Barcelona, June 2022

Contents

ACKNOWLEDGEMENTS

First of all, I would like to express my sincere gratitude to my supervisor Jens Biegert for his guidance and suggestions throughout my PhD study. Offering me a PhD opportunity after my master's study and provided generous support and encouragement in my research. His help and advice guided me through the world of ultrafast physics pushing me to learn more, especially ultrafast molecular dynamics.

I would like to acknowledge with much appreciation the ReMi team with whom I have been working for more than four years. I would like to give an especial thanks to Tobias Steinle, Kasra Amini, and Aurelien Sanchez, from whom I learnt almost everything about Reaction microscope systems and imaging of molecular structures. They shared all their experience with me and fully supported my PhD. I would like to thank Katharina Chirvi and Meng Jie for their full support at the end of my PhD.

Furthermore, thanks to all my colleagues who worked with me in the AUO group: Blanca Belsa, Hung-Wei Sun, Ying-Hao Chien, Lenard Vamos, Igor Tyulnev, Julita Poborska, Stefano Severino, Ugaitz Elu, Nicola di Palo, Julius Huijts, Maurizio Reduzzi, Adam Summers, Luke Maidment, Daniel Rivas, Florian Haberstroh, Michael Enders.

Furthermore, I would like to acknowledge the jury members and my thesis committee members, who offered valuable suggestions and help for my PhD study.

Again, a great thanks to all my friends in Europe and China, who gave me numerous support and encouragement both in life and study.

Last but not least, I would like to take this opportunity to thank my family for all their support and love, especially my parents and my wife Qi, who never said a no to my dreams.

Thank you.

ABSTRACT

One of the significant challenges of modern science is to track and image chemical reactions as they occur. The molecular movies, the precise spatiotemporal tracking of changes in their molecular dynamics, will provide a wealth of actionable insights into how nature works. Experimental techniques need to resolve the relevant molecular motions in atomic resolution, which includes (10^{-10} m) spatial dimensional and few- to hundreds of femtoseconds (10^{-15} s) temporal resolution.

Laser-induced electron diffraction (LIED), a laser-based electron diffraction technique, images even singular molecular structures with combined sub-atomic picometre and femto- to attosecond spatiotemporal resolution. Here, a laser-driven attosecond electron wave packet scatters the parent's ion after photoionization. The measured diffraction pattern of the electrons provides a unique fingerprint of molecular structure. Taking snapshots of molecular dynamics via the LIED technique is proved to be a potent tool to understand the intertwining of molecules and how they react, change, break, bend, etc.

This thesis is especially interested in exploiting advanced LIED imaging techniques to retrieve large complex molecular structures. So far, LIED has successfully retrieved molecular information from small gas-phase molecules like oxygen (O_2), nitrogen (N_2), acetylene (C_2H_2), carbon disulfide (CS_2), ammonia (NH_3) and carbonyl sulfide (OCS). Nevertheless, most biology interesting organic molecules typically exist as liquid or solid at room temperature. In order to accomplish the final goal to extract these larger complex molecular structural information, we need to overcome two main challenges: delivering the liquid or solid samples as a gas-phase jet with sufficient gas density in the experiment and developing a new retrieval algorithm to extract the geometrical information from the diffraction pattern. We tested one of the most simple liquid molecules - water H_2O in the reaction chamber as a primary step. We traced the variation of H_2O^+ cation structure under the different electric fields. To solve the problem of unsatisfactory gas density, we present a novel delivery system utilizing Tesla valves that generates more than an order-of-magnitude denser gaseous beam. Machine learning is well qualified to solve difficulties with manifold degrees of freedom. We use convolutional neural networks (CNNs) combined with LIED techniques to enable atomic-resolution imaging of the complex chiral molecule Fenchone ($C_{10}H_{16}O$).

Chapter 1

Introduction

Contents

1.1 Context

Ultrafast technology with high time resolution could trace back to the 19th century. In 1872, Leland Stanford, a former Governor of California and racehorse owner, hired an English photographer named Eadweard Muybridge [1] to depict his richness, including his racehorse. He wanted a decent picture to describe a horse running at full speed and did not trust the existing depictions. Because the human eye could not break down the motion of the house at a gallop, at that time, most people thought the horse was running with the front legs extended forward and the hind legs extended to the rear, the four feet away from the ground. In June 1878, Muybridge utilized 12 cameras along the race track, the camera's shutters were triggered when the legs of a horse tripped wires connected to an electromagnetic circuit, and the shutter exposure time was 10^{-3} s, which captured the hoof of the horse during the race.

Subsequently, high-speed photography technology developed rapidly. In 1930, Professor Harold Edgerton [2] invented stroboscopic flash technology, which used a short pulse source to freeze the motion picture to observe the details of the change. Its time resolution depended on pulse width rather than the speed of the mechanical shutter. In order to further study the various changes in nature, people were focusing on finding shorter probes to detect these changes. With the development of laser technology, it was possible to obtain probe pulse with ultrashort bandwidth. In 1960, Maiman [3] successfully developed the first ruby laser, and since then, humans have owned the ultrashort pulse laser technology. In 1961, Hellwarth et al. [4] used Q-switching technology to achieve a pulse output with a pulse width of tens of nanoseconds on a ruby laser. However, due to the limitation of the resonator's length and the speed of light, the laser pulse cannot be compressed to lower than the nanosecond order. People needed to find new ways to achieve shorter pulses. Mode-locking technology was born two years later, and laser pulse duration achieved to sub-picosecond in the subsequent 20 years. In the 1980s, chirped-pulse amplification tech-

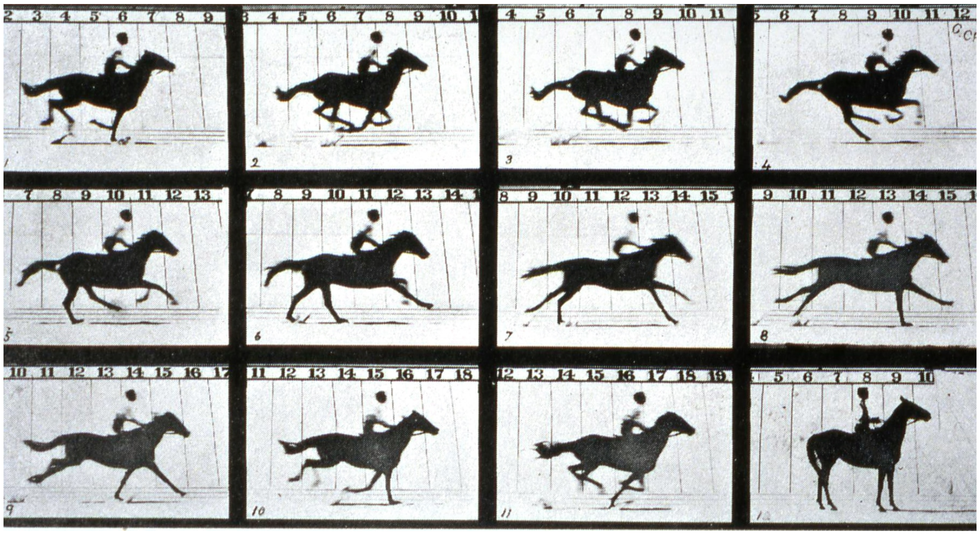

Figure 1.1: **Muybridge's The Horse in Motion, 1878.** Muybridge designed consecutive series of photographs with a battery of 12 cameras along the race track, imaging the first dynamic motion that could not trace by human eyes.

nology emerged, combined with self-mode locking, and lasers entered the ultrashort pulses era. Femtosecond pulse lasers have become powerful tools [5] for people to study ultrafast phenomena and generate new domains like femtochemistry. Femtochemistry, stated by Manfred Eigen awarded the Nobel prize in Chemistry in 1967 to measure fast chemical reactions. As a pioneered work in the 1980s and 1990s, Ahmed Zewail and his group first implemented pump-probe type time-resolved measurements in structure deformation, charge immigration, and energy transfer domain. Due to his outstanding contribution, Zewail was awarded the Nobel prize in Chemistry in 1999 [2].

The process of studying ultra-fast response has high requirements for the temporal and spatial resolution of the detected method. The spatial resolution presents the ability to distinguish the minimum distance between two points. The minimum spatial resolution of the general human eye is 0.1 mm, so the naked eye can see 0.1 mm hair strands. The minimum spatial resolution of an optical microscope is 200 nm (10^{-9} m), according to Abbe's equation as:

$$d = \frac{0.61\lambda}{NA} \tag{1.1}$$

where λ is light wavelength and NA presents numerical aperture.

The spatial resolution of the optical microscope depends on incident beam wavelength, the minimum of the visible light around 400 nm, so we perceive the limitation around 200 nm in the optimal situation. For example, cells with a size of 1 µm cannot be discerned with the naked eye but an optical microscope is able to capture them. Nevertheless, an optical microscope's spatial resolution is insufficient to satisfy its requirements for the spatial scale of 1 Å (0.1 nm as biological macromolecules and molecules).

In order to obtain a higher spatial resolution, an illumination source with a wavelength much smaller than visible light must be found. X-rays and electrons as good candidates.

X-ray is high-energy electromagnetic radiation with a wavelength ranging from 10 pm 10^{-12} to 10 nm, corresponding to frequencies in the range 30×10^{15} Hz to 30×10^{18} Hz and energies in the range 124 eV to 124 keV. The wavelength is much shorter than ultraviolet in visible light. Another interesting candidate is the electron, which was treated as a particle only for a long time until 1924. Louis de Broglie proposed in his doctoral thesis that electrons can also have wave properties in addition to the properties of particles, which is the De Broglie hypothesis. He believed that all substances have wave-like properties and connected the wavelength λ and momentum p of matter as

$$\lambda = \frac{h}{p} = \frac{h}{\sqrt{2E}} \tag{1.2}$$

where h = 6.63×10^{-34} J·s is Planck's constant, p is electron momentum, m_e is the mass of the electron, E is the kinetic energy of the electron. If we consider electron energy in range 100 eV to 1000 eV related to the wavelength in range 0.4 to 1.2 Å (10^{-10}m).

The temporal resolution directs to the discrete resolution of measurement concerning time scale. Nature is changing all the time with various reaction time scales. An instrument with an adequate temporal resolution is essential to help us understand the basics of reactions. Here are the various reaction time scales to present: The motion of valence electrons as ionization process happens typically on the sub-fs (10^{-15} s) level; the vibration and dissociation reactions of molecule occur on the level of several 100 fs; the rotation of molecules occur on the time scales of µs to ps; the breaking of chemical bonds occurs on the time scale of fs to ps (10^{-12} s); the structural phase changes of objects occur on the scales of ps to ns (10^{-9} s); the tissue growth changes of organisms occur in the ps to ms (10^{-3} s) or even longer time range [6]. Although the time scale of these processes spans more than a dozen orders of magnitude, they are essentially changes in the original or sub-position. In order to fundamentally understand the changes in nature and control the evolution of specific processes, people have invested great interest in finding the shorter time and higher spatial precision probes to detect this fundamental process.

One of the most exciting photochemicals is to investigate the formation of vision. Retinal, also known as retinaldehyde, is the chemical foundation of animal vision. Light can convert 11-cis retinal into all-trans-retinal, which is essential for forming vision. The vision production causes the decomposition of rhodopsin to happen on is hundred femtosecond scale, which is pretty challenging to visualize the process due to its fast time scale.

To provide revolutionary insights into critical transition points such as transition states [7], electron and nuclear dynamics in conical intersections [8], proton migration [9] and isomerization [10], an imaging method that could achieve the femtosecond temporal resolution and sub-Ångström spatial resolution is highly demanded. X-ray diffraction (XRD) and ultrafast electron diffraction (UED) appeared to be good candidates to solve the problems. In the last decades, these two methods have achieved atomic spatio-temporal resolutions as promising techniques, but both have unavoidable shortcomings. For X-ray diffraction imaging to achieve a few-nm wavelength and sub-fs X-ray pulse, usually a large scale facility like free-electron laser is needed, meanwhile, due to the lower cross-section of the photons, it needs a careful balance between sufficient beam brightness and threshold of the sample damaging and challenge to capture the motion of hydrogen atom. For the

UED, electrons have a much higher cross-section than photons, but the space charge issue limited the temporal resolution of the technique. An alternative, laser-induced electron diffraction (LIED), is a table-top, laser-based UED method that combines the sub-atomic picometre and femtosecond-to-attosecond spatiotemporal resolution imaging of a single molecular geometry. Here, a laser-driven attosecond electron wave packet (EWP) scatters the parent's ion after photoionization. The measured diffraction pattern of the electrons contains molecular interference signal is typically characterized by interference between an EWP and the nuclei of atoms which provide a unique fingerprint of molecular structure. Therefore, the information about the parent ion's structure and ultra-fast dynamic evolution can be extracted by measuring the scattered electron momentum. Taking snapshots of molecular dynamics via the LIED technique is proved to be a potent tool to understand the intertwining of molecules and how they react, change, break, bend, etc. On the other hand, the attosecond electron beam driven by the long-wavelength laser will have higher energy. It corresponds to a shorter De Broglie wavelength providing higher spatial resolution for the LIED method, directly promoting molecular ultrafast dynamic imaging.

This thesis is especially interested in exploiting advanced LIED imaging techniques to retrieve large complex molecular structures. So far, LIED has successfully retrieved molecular information from small gas-phase molecules like oxygen (O_2), nitrogen (N_2), acetylene (C_2H_2), carbon disulfide (CS_2), ammonia (NH_3) and carbonyl sulfide (OCS). Nevertheless, most biology interesting organic molecules typically exist as liquid or solid at room temperature, like retinal and azobenzene. LIED is based on the diffraction of the gas phase molecules. In order to accomplish the final goal to extract these larger complex molecular structural information, we need to overcome two main challenges: delivering the liquid or solid samples as a gas-phase jet with sufficient gas density in the experiment and developing a new retrieval algorithm to extract the geometrical information from the diffraction pattern.

As a primary step, we deliver one of the most simple liquid molecules - water H_2O in the reaction chamber. We trace the variation of H_2O^+ cation structure under the different electric fields (Chapter 3). H_2O owns vapour pressure of 23 mbar at room temperature. However, most organic molecules have much lower vapour pressure (e.g. <1 mbar for cis-stilbene), producing insufficient gas density in the interaction zone and not detecting adequate signals to perform a LIED measurement. To solve the problem of unsatisfactory gas density, we present a novel delivery system utilizing Tesla valves that generates more than an order-of-magnitude denser gaseous beam of cis-stilbene molecules at the interaction region by ensuring a fast, unidirectional flow of the gaseous sample in chapter 4.

Since the 1930s, the retrieval of gas-phase molecular structures using electron diffraction requires the interpretation of molecular interference patterns and the extraction of information based on fitting algorithms. Worse, LIED needs to first convert field-dressed information into field-free cross-sections before applying extraction algorithms. These complications negatively impact widespread adoption and advance for time-resolved investigations. Current retrieval algorithms are limited to few-atom molecular systems, becoming more challenging to identify extremum in a multi-dimensional solution space as the structural complexity increases. Machine learning (ML) is well qualified to solve difficulties with manifold degrees of freedom. Chapter 5 presents a remedy based on a specific implementation of a convolutional neural network (CNN) to retrieve the large and complex molecular structures. The solution is based on a pre-calculated and sufficiently large ensemble of structural solutions, which the network can identify as matching the measured structure. Furthermore, the established database only considers the changes of a few essential groups and a molecule-wide global change in the structure. We train the ML model following such a reduced database to let the machine figure out the relationship between the molecular structures and their corresponding interference signals. This proposition drastically depreciates computational time. The ML-LIED framework overcomes the above-stated convergence issues and shows the capability to accurately predict the three-dimensional larger complex chiral molecule (+)-Fechone ($C_{12}H_{14}O$; 27 atoms) measured with LIED.

Chapter 2

Background and Fundamental

Contents

2.1 Fundamentals of Strong-field Physics

The photoelectric effect is one of the most common and fundamental interactions between light and matter. Einstein won the Nobel Prize in Physics for successfully explaining the photoelectric effect more than a century ago. Einstein believed that light energy should be shared as one portion, and each portion of light energy is called a photon. The bound state electron can only absorb one photon's energy to execute a transition. Photoionization occurs when the photon's energy is larger than the energy of the bound electron, the electron will absorb a photon and then escape. The theory does not deny the possibility of atoms absorbing multiple photons. Using low-order perturbation theory can predict that electrons can absorb two photons and be ionized [61, 18]. Just in terms of the experimental conditions at the time, the light intensity is generally low and the physical phenomena are linear with lower light intensity. Therefore, Einstein's description of electrons absorbing one photon at that time is almost true. Laser sources have developed rapidly [15] since the first ruby laser was built in the 1960s [100], which greatly enhanced light source interactions with matter producing many nonlinear physical phenomena. As the laser intensity rises, the laser electric field will increasingly affect the Coulomb field, causing revision in the mechanism of the electron ionization performance. Due to different laser intensities, the ionization process can be roughly divided into multiphoton ionization, tunnelling, and over-barrier ionization.

2.1.1 Multiphoton ionization

The ionization behaviour of atoms and molecules in an intense laser field is one of the essential research contents in strong fields. At present, the centre wavelength of numerous high power lasers is around 800 nm, mainly extending to the mid-infrared (larger than 800 nm wavelength) appreciations to the OPA technology develops. The corresponding photon energy is much smaller than the energy level difference of the atom's ground state to the continuum. The atom must absorb multiple photons simultaneously to be ionized, leading to the multiphoton ionization (MPI) process. Soon after the invention of the laser, the phenomenon of MPI was discovered when Voronov et al. excited the Xenon by the ruby laser with seven photon ionizations [11] and Hall et al. [12] to measure the dissociation of iodide ions(I^-). MPI is a process in which the electrons absorb multiple photons and then ionize when the laser light interacts with atoms and molecules with a higher frequency and a lower intensity ($I < 10^{13}$ W/cm^2).

$$E = N\hbar\omega - I_{\mathrm{p}}, \tag{2.1}$$

where N is the minimum number of photons required for ionization. Since MPI occurs when the light intensity is relatively weak, utilizing low-order perturbation theory is adequate to describe ionization probability. It takes the first term in the time-dependent perturbation theory, describing total ionization probability by the absorption of n photons Γ_n[13, 14, 15] as:

$$\Gamma_n \propto I^n \sigma_n \tag{2.2}$$

Where σ_n is the generalized absorption cross-section of n photons, the MPI probability rises nonlinearly with light intensity change. The MPI of the He atom experimentally confirmed consistently with the Eq. 2.2 at n=22. However, it was later proved that exist a maximum laser intensity (I_s) called the saturation intensity [16]. The ionization no longer increases when the light intensity exceeds I_s since atoms are fully ionized before the laser intensity approaches its maximum. Meanwhile, the ionization probability no longer follows the Eq. 2.2.

σ_n is a one-fraction formula that may encounter a situation where the denominator is zero [17]. It can be understood that a ground-state electron absorbs multiple photons then reaches a particular intermediate Rydberg energy level of the atom. Consequently, resonance occurs, causing the higher probability of multiphoton ionization called resonant-enhanced multiphoton ionization (REMPI) [17] shown in Fig. 2.1.

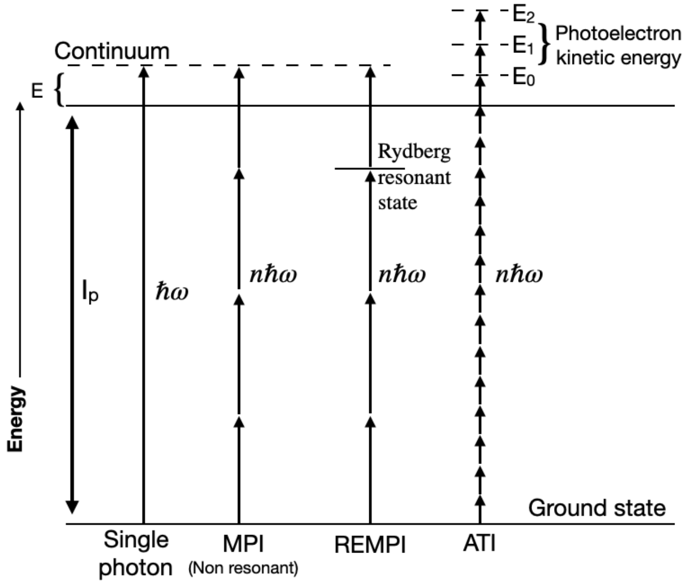

Figure 2.1: Schematic diagram of single-photon, multi-photon and above threshold ionization process.

2.1.2 Above threshold ionization

One of the most critical pieces of experimental evidence for the non-perturbation of multiphoton ionization is the photoelectron spectrum measurement by Agostini's team in 1979 [18]. The energy spectrum contains a series of separated peaks. The peak-to-peak distance is equal to photon energy, reflecting that the number of photons absorbed can be far plenty than the minimum number of photons required for ionization. It is later well known as the above-threshold ionization (ATI), was first named by Karule in 1978 [19], and became an essential topic in strong field research. Initially, the longer laser pulse and the weaker light intensity offer the final kinetic energy of the photoelectrons as:

$$E = (N + S)\hbar\omega - I_{\mathrm{p}}, \tag{2.3}$$

S is the number of additional photons absorbed.

However, with the light peak intensity improved and the appearance of higher resolution time-of-flight spectrometers [20]. Kruit et al. [21] found that as the laser intensity increased, the first peak of the ATI spectrum disappeared. The amplitude of the other peaks no longer follow the formula Eq. 2.2, which is contradictory with the previous results. Later experiments found that more ATI peaks disappeared [16, 22]. When the pulse energy changes raised from 3.4 mJ to 6.8 mJ, the low order peaks gradually decrease while the high-order peaks continuously increase and shift toward the lower energy area. The phenomenon of low-order ATI peaks being "suppressed" is a non-perturbative effect where the eigenstate of the atom is disturbed, which is understood as an AC-Stark shift [23] because the atomic bound state moves as the laser become intense.

The electrons moving freely in the laser field have vibrational kinetic energy due to the action of the laser's electric field, which is the so-called Ponderomotive energy (U_p).

$$U_\mathrm{p} = \frac{e^2E^2}{4m\omega^2} = 9.33\lambda^2(\mu\mathrm{m}) \times I(10^{14}\ \mathrm{W/cm^2})(\mathrm{eV}), \tag{2.4}$$

where e is the charge of the electron, E is the laser's electric field, m is the electron mass and ω is the laser frequency. An intense electric field affects the weakly bound Rydberg state, shifting its energy level close to the Ponderomotive energy. In contrast, the electron close to the nucleus has small polarizability and is adversely affected by the external field. The movement in the low energy state is negligible compared with the high Rydberg state, driving to the I_p is approximately expand a U_p. The significant increment of ionization potential will suppress the ionization from lower-order channels. At this time, the energy of the electron after ionization becomes:

$$E = (N + S)\hbar\omega - (I_\mathrm{p} + U_\mathrm{p}), \tag{2.5}$$

Suppose the pulse duration is longer than the picoseconds order [24], the ionized electrons will undergo an uneven electric field $-\nabla U_\mathrm{p}$ [25] to become free electrons, where the energy of electrons gained from the laser field offsets the expanded potential energy, and then Eq. 2.3 is valid. If the pulse duration is shorter than the picoseconds order, the electrons cannot obtain adequate energy from the laser field, then Eq. 2.5 is established. With the Eq. 2.5 and Eq. 2.4, electron kinetic energy is decreased with raising the U_p, higher laser intensity pointing to the ATI peaks moved to the low-energy edge.

At a particular moment, the energy level interval between the ground state and a particular shifted Rydberg state is equal to an integer multiple of the photon energy. The ground state electrons may resonantly transit to the Rydberg state, next ionized after absorbing photons. It is called Freeman resonance manifested in the energy spectrum where the peak is split into many narrow resonance peaks [26].

2.1.3 Tunneling ionization/ Quasi-static regime

MPI happed in the region where the light intensity is about 10^{13} W/cm^2. In general, the multiphoton excitation path of electrons is realized through intermediate states. Suppose the laser intensity is adequate and the frequency is relatively low (longer wavelength), the laser field can be regarded as quasi-static. The intense laser field distorts the Coulomb potential and formes a potential barrier along with the polarization of the field. Hence, the electrons in the bound state could penetrate potential turned to free electrons as shown in Fig. 2.2c, called tunnelling ionization (TI).

As early as 1965, Keldysh [27] realized that the electrons ionization mechanism can be developed with the varieties of laser intensity and wavelength. He proposed an adiabatic constant γ to describe the two different ionization mechanisms of MPI and TI. This constant is the so-called Keldysh parameter reflects the ratio of the time of the bound electron tunnelling from the barrier to the period of the laser field as:

$$\gamma = \frac{\omega_{\text{laser}}}{\omega_{\text{tunnel}}} = \sqrt{\frac{I_{\text{p}}}{2U_{\text{p}}}} \tag{2.6}$$

Generally, $\gamma = 1$ is used as the dividing border between the two ionization mechanisms. It is commonly believed that when the $\gamma > 1$, i.e. the light intensity is weak and the laser frequency is higher (the shorter wavelength), the multiphoton ionization plays a leading role. In contrast, when $\gamma < 1$, as the light intensity is intense and the laser frequency is lower (longer wavelength), the tunnelling ionization leads the process.

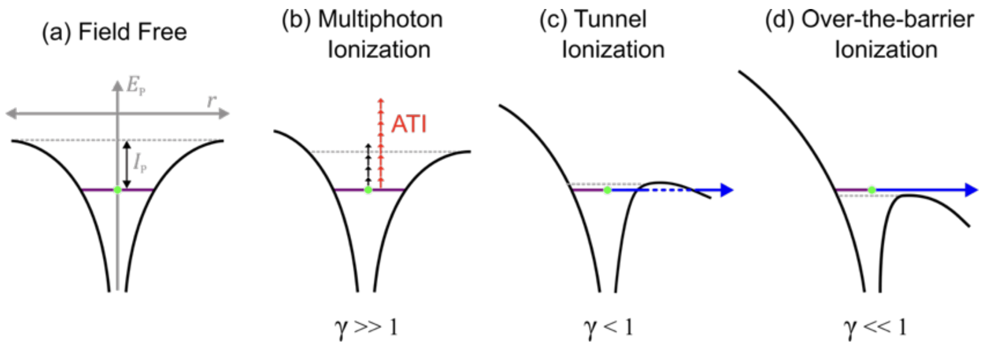

Figure 2.2: **Nonlinear ionization mechanisms.** **(a)** Potential in the field free. **(b)** Multi-photon ionisation: electrons absorb multiple photons and ionise when the laser light interacts with atoms or molecules with a higher frequency and a lower intensity ($I < 10^{13}$ W/cm^2). In case of gain extra kinetic energy by absorbing additional photons is called above-threshold ionisation. **(c)** Intense laser field distorts the Coulomb potential, and the electrons in the bound state could penetrate potential turned to free electrons. **(d)** Over the barrier ionization: ground state electrons can directly cross the potential barrier, escape the atomic core's bondage and become free electrons.

2.1.4 Over the barrier ionization

It is not difficult to imagine that with the further increase of laser intensity, the potential barrier in the Fig. 2.2c will be suppressed lower and lower. When the light intensity progresses to a certain critical point, the ground state electrons can directly cross the potential barrier, escape the atomic core's bondage and become free electrons (Fig. 2.2d). Therefore, the tunnelling ionization transitions to the over the barrier ionization (OBI).

$-2\sqrt{Z_{\mathrm{eff}}E_{\mathrm{OB}}}$ is the highest point of the potential barrier determined by the superposition of the laser field and the Coulomb potential, where $\mathrm{Z}_{\mathrm{eff}}$ is the number of charges of the atom. The OBI will happen when $-2\sqrt{Z_{\mathrm{eff}}E_{\mathrm{OB}}}$ below (I_{p}), means the electric field of laser:

$$E_{\mathrm{OB}} = \frac{\pi\epsilon_0 I_{\mathrm{p}}^2}{Z_{\mathrm{eff}}e^3}, \tag{2.7}$$

for the laser intensity:

$$\begin{aligned} I_{\mathrm{OB}} &= \frac{\pi\epsilon_0^3 c I_{\mathrm{p}}^4}{2\mathrm{Z}_{\mathrm{eff}}{}^2 e^6} \\ &= 4\times 10^9 I_{\mathrm{p}}{}^4(\mathrm{eV})/\mathrm{Z}_{\mathrm{eff}}{}^2\ (\mathrm{W/cm^2}) \end{aligned} \tag{2.8}$$

Taking hydrogen atoms as an example, concerning a laser pulse with a wavelength of 3.2 µm, the intensity of 2.2×10^{13} ($\mathrm{W/cm^2}$) is the boundary between MPI and TI, and 1.4×10^{14} ($\mathrm{W/cm^2}$) is the critical value for the transition from TI to OBI.

When the laser intensity extends further, the ionization suppression of atoms [28, 29], the excitation and ionization of the inner shell electrons, the generation of hard X-rays and γ rays, and relativistic plasmas may occur. Moreover, nuclear excitation and nuclear reactions may occur at a much higher intensity [13].

2.2 Quantitative models

The introduced the quantum theory of light initiated up people's minds and made people realize that the world may not be continuous. Quantum mechanics can explain most atomic and molecular scale microscopic physical phenomena like electron ionization. A wave function describes the electronic state in quantum mechanics. The electrons bound in the atom are stably in the eigenstate of the atomic Hamiltonian. If an electromagnetic field is applied, the system Hamiltonian will appear as the interaction term between the electron and the electromagnetic field. The electrons in the continuous state can be regarded as ionized free electrons. In this way, Quantum mechanics provides a systematic method to obtain the evolution of the electronic wave function by solving the time-dependent Schrödinger equation (TDSE), obtaining the probability of ionized electrons (the ionization rate) or the probability of electrons with specific energies or momentum (momentum spectrum of the electron).

However, it is not a simple task to solve the TDSE. The equation itself is hard to figure out an accurate analytical solution and mainly be solved numerically with the help of a computer. Even with the help of larger computer clusters, it can only accurately solve the TDSE of atomic and molecular systems with very few electrons (around 2 electrons). An appropriate approximation has to be made to perform numerical calculations for multibody systems. This is why people continue to develop simple models to get results quickly and efficiently.

In the era of no high-speed computer, people always need to adopt various reasonable approximations when dealing with quantum mechanics theory in order to obtain results applicable under certain conditions. In 1964, Keldysh [27] proposed a unique idea that utilizing the transition matrix elements to calculate strong fields ionization, the transition matrix from the initial ground state to the final approximated free-electron state in the electromagnetic field, ignores the influence of the Coulomb potential. This is because ionized electrons influenced by the Coulomb force are negligible compared to the external electric field. Therefore this method is named strong-field approximation (SFA). Keldysh theory can give the law of electron ionization probability under strong fields and predict non-perturbative ionization phenomena, such as ATI peaks. However, more phenomena could not be observed experimentally limited by insufficient laser intensity to satisfy the requirements. The value of Keldysh's theory was temporarily buried until 1979 when the ATI phenomenon was first experimentally confirmed. In 1973 and 1980, Faisal [30] and Reiss [31] respectively calculated the transition matrix elements from the initial state to the final state under the same starting point following the velocity gauge and received the analytical expressions of the transition matrix elements expanded by the Bessel function. Later, with the help of chirp amplification technology [32], the laser light intensity reached the tunnelling zone predicted by Keldysh. Keldysh, Faisal and Reiss (KFR theory) theory began to be widely used to explain the experimental phenomenon under the tunnelling region. The KFR theory has been developed more thoroughly, including various situations such as short laser pulses and Coulomb potential effect correction. The methods developed from the KFR theory can be collectively called the SFA method.

On the other hand, in contrast to Keldysh's model neglecting the Coulomb interaction, Perelomov et al. [33] calculated the ionization rate of an arbitrary bound state of the electron under the short-range potential (PPT rate) in 1966. This method obtains the same exponential term as Keldysh and gives the analytical expression of the pre-exponential factor. The PPT theory also obtained the ionization rate of the atomic Coulomb potential system following non-adiabatic conditions. In 1986, Ammosov et al. [34] used quasi-static conditions to simplify the expression of the PPT rate to obtain the atomic ionization rate (ADK rate) under adiabatic approximation. These early works laid a solid foundation for the later semi-classical theory and became indispensable in strong fields.

2.2.1 Solving time-dependent Schrödinger equation

Direct numerical integration of TDSE can study the interaction between atoms or molecules and laser fields of different pulse types in any frequency and any range of light intensity. It can accurately describe experimental results and predict new effects. By numerically integrating the TDSE, the evolution of the wave function of the system and the atomic dipole moment with time can be obtained. The Fourier transform can be applied to obtain the value of the photoelectron energy spectrum and high-order harmonic radiation.

Despite its many advantages, numerical integration methods have only been strictly applied in recent years. Because of the large amount of computation required to calculate the proper pulse wavelength has only recently been possible to do it in a reasonable time. Such an enormous amount of calculation is mainly caused by the transition of electrons from the ground state to the continuous state or the relatively high speed driven by an oscillating laser field. These high-speed electronic wave packets can travel a long distance in a short time. This requires that each integration grid in the spatial integration is large enough and the grid spacing is sufficient to simulate the motion equation of the wave packet. The exact requirements apply to time integration. Therefore, in order to reduce the amount of calculation, methods such as dimensionality reduction and single-electron approximation are applied to the actual calculation simulation.

On the other hand, in the numerical integration process of solving the TDSE, the problem of the singularity of the natural atomic potential will be encountered. Therefore, in actual calculations, people often use different atomic potentials to replace the real atomic potentials. These different alternative potentials can reduce calculation time and also be used as an essential parameter to study the relationship between different potentials and certain physical phenomena.

At present, solving the TDSE is an essential method for the theoretical research of strong-field physics. However, it has inherent shortcomings: First, due to the limitation of computer technology, it is currently necessary to simultaneously calculate real atomic problems, including three-dimensional space and time. It is not easy to do this, even with a supercomputer. It is more difficult for molecules with more complex structures. Second, TDSE includes most of the factors of the physical problem, which makes some physical phenomena hard to obtain through numerical simulation, let alone give the corresponding physical process intuitively.

2.2.2 Three steps model

For a long time after discovering electrons in the 19th century, people generally believed that electrons were charged particles with a relatively small volume and a non-zero mass following the classical law of motion on a macroscopic scale. The motion of an electron in the electromagnetic field can also be fully predicted and observed through the Wilson cloud chamber. Many types of measuring instruments are designed based on the classic motion of electrons, such as electron accelerators, electron velocity selectors, velocity map imaging (VMI), Reaction Microscope (ReMi) or cold target recoil electrons ion momentum spectrometer (COLTRIMS) etc. The design of these instruments is based on the recognition that electrons are charged particles. Newton's second law can describe the motion of electrons subjected to an electromagnetic field, thus having a definite trajectory.

The proposal of quantum mechanics has given people a new perception of electrons. Planck's wave-particle duality points out that all particles have volatility. The small mass of electrons' volatility is even more prominent and confirmed by electron diffraction and electron double-slit interference experiments. It is worth noting that the classical behaviour of electrons and quantum are not contradictory, and their quantum actions occur at a microscopic scale, and the macroscopic electron motion is indeed classical. So how small is the scale at which the classical orbit description is no longer applicable, and the volatility of electrons are considered? This can be roughly estimated using the uncertainty principle of quantum mechanics. In the atomic unit, there is $\delta p \delta x \approx 1$, the magnitude of the thermal motion speed of the electron in the macroscopic order is c/1000, and the speed of light in the atomic unit is c = 137. If the electron has a velocity error of 0.1%, then it can be estimated that the error range of the electron position is about

10^4 *a.u.* ≈ 200 nm, which is almost a tiny amount for macroscopic measurement. However, it is much larger than the molecular and atomic scale or the lattice spacing (on the order of 10 a.u.), reflecting by electrons entering the crystal will be diffracted. In principle, the classical description is no longer valid to determine the electrons' position at the atomic scale. We need to use quantum mechanics to describe that electrons are no longer treated as particles but in probability waves. Quantum mechanics can explain almost all physical phenomena on the atomic scale, including ionization in the strong field studied in this thesis.

As mentioned in the last subsection, although the description of quantum mechanics is theoretically the most correct, it is too complicated to be calculated in practice. Especially when the laser intensity is raised to a highly nonlinear physical process, the perturbation theory of quantum mechanics can no longer be used to perform calculations. Developing other methods to solve the Schrödinger equation or establish a new model under these conditions is necessary.

Corkum et al. [35, 36] innovatively proposed a method that re-uses classic images to describe electrons. He believes that under the action of a strong laser field, the electrons in atoms undergo the following processes: In the first step, a sufficiently strong laser field lowers the Coulomb barrier so that electrons tunnel out into free electrons. The ADK rate gives the tunnelling probability; In the second step, the electrons become free electrons with an initial position of zero and travel in the laser field, ignoring the effect of the nuclear Coulomb force, the Newtonian equation of motion can solve the trajectory of the electron. If the laser field is circularly polarised light, it will be found that the electron's trajectory is no longer returned to the origin. After the laser is terminated, the electrons gain energy from the electric field and fly directly to the detector without interaction with the nucleus. The finally detected electron ionization rate is the electron tunnelling probability of the first step, so people often use circularly polarized light to study the electron ionization rate or tunnelling probability [37, 38]. In the case of linearly polarised light, there will be more abundant physical phenomena in the third step, where the light field drives the free electrons at certain moments to return to the origin. Three physical processes may occur during the interaction between the electron and the nucleus: the first is the elastic scattering of the electron and the nucleus, and the magnitude of the speed remains the same. At the same time, the exit direction is deflected or even reversed. After that, the electrons continue to be driven by the laser field and finally achieve relatively high energy. This process explains the generation of the high-energy plateau region of the electron spectrum; The second is when the electron returns and interacts with the residual nucleus, transferring part of the energy to another electron to cause a double ionization process; The third is that the nucleus capture the returning electron, and the electron energy is converted into optical radiation releasing high-order harmonics. The classical equation of motion determines the electron returning to the nucleus with maximum energy of $3.17U_\mathrm{p}$. Theoretically, the maximum energy of the radiated photon should be $3.17U_\mathrm{p} + I_\mathrm{p}$. The above prediction is consistent with the high-order harmonic cut-off frequency observed in the experiment. The above model refines the physical process in the strong field into three main steps, so it is called the three-step model. Since the electrons in the second step are regarded as classical particles, the model is also called the quasi-classical method.

The essence of the three-step model lies in openly treating electrons as particles on the atomic scale. We discussed the limitations of this processing method at the beginning of the chapter. However, it can be qualitatively or even quantitatively in line with experimental observations. Under which conditions, electrons can be regarded as particles becomes an important issue. As mentioned earlier, the positional dispersion is as high as 200 nm for relatively low-velocity electrons on a macroscopic scale, which is impossible to be considered as particles at the atomic scale. However, the situation in a strong field is acceptable. When the laser wavelength is 2000 nm and intensity is 2×10^{14} W/cm^2, the maximum reachable speed that the electron driven by the light field can be estimated by the vector potential $A = E/\omega \approx 3.3$ $a.u.$, and the electron's range of motion is about $E/\omega^2 \approx 145$ $a.u.$. We assume 5% is uncertainty the electron speed, then momentum uncertainty is $\delta p = 0.165$ $a.u.$. According to the uncertainty principle, position uncertainty is estimated as $\Delta x \approx 6$ $a.u.$. It can be seen that the uncertainty of the electron wave packet is indeed a small amount relative to the range of movement of the electron driven by the electric field, so it is feasible to treat the electron as a particle under this condition. It is the basis for using classical particle images to describe the motion of electrons in a strong field. The fundamental reason is that a strong laser field can accelerate electrons sufficiently, causing a tiny position uncertainty range. On the other hand, the electrons have a more extensive span of motion driven by a strong field, so the trajectory can be approximated to describe the action of the electron. On the contrary, the classic image is invalid when the field is too small, the electron of position uncertainty is larger than the span of the movement. The longer the laser wavelength and the higher the light intensity offer a more accurate classic image describing electronic behaviour.

2.2.3 Tunneling probability

The first step of the three-step model is that the most critical action that the tunnelling probability and initial momentum distribution directly affect the final momentum spectrum. Landau and Lifshits [39] gave the tunnelling probability of electrons in a hydrogen atom system following an electrostatic field which is the basis for solving the ionization probability under quasi-static conditions, and the PPT rate and ADK rate are derived from there (Eq. 2.9).

$$W_{\text{stat}}(E) = \frac{4}{E}\ \exp(-\frac{2}{3E}) \tag{2.9}$$

Subsequently, Smirnov and Chibisov [40] used the same method to calculate the ionization probability of any bound state of a hydrogen-like atom under an electrostatic field. Soon Perelomov et al. [33] improved their results to a simple harmonic light field, assuming that the light field satisfies the quasi-static condition $\gamma = \omega/\omega T \ll 1$ (same as Eq. 2.6), then the electric field could be recognized as constant during the tunnelling process. Assuming the external harmonic electric field at each tunnelling moment is approximated as an electrostatic field, tunnelling probability for the electrostatic field is accepted. For the hydrogen-like atom with a nuclear charge of Z, $E_n = Z^2/(2n^{*2})$ is the energy level with effective principal quantum number n^* is , and the field strength is defined as $E_0 = (2E_n)^{3/2}$.

The ionization probability of arbitrary principal quantum number n^*, angular quantum l and magnetic quantum number m is expressed as:

$$W_{\mathrm{stat}}(E) = EC_{n^*l}^2 \frac{(2l+1)(l+|m|)!}{2^{|m|}(|m|)!(l-|m|)!} (\frac{2E_0}{E})^{2n*-|m|-1} \exp(-\frac{2E_0}{3E}) \tag{2.10}$$

The above equation also needs to satisfy the condition $E \ll E_0$. Considering a linearly polarized monochromatic field as $E(t) = E\cos(\omega t)$, its ionization rate contains one more coefficient $W_{\mathrm{lin}} = (3E/\pi E_0)^{1/2} W_{\mathrm{stat}}$ comparing with an electrostatic field due to the averaged within a period. The general situation for circularly polarised light is quite complicated because of the varied direction of the electric field changing so that the magnetic quantum number m is not constant. Nevertheless, the magnitude of the electric field is a constant for the s state, and the ionization rate should be the same as that of the electrostatic field as $W_{\mathrm{cir}} = W_{\mathrm{stat}}$. In the Eq. 2.10, C_{n^*l} is the asymptotic coefficient related to various types of atoms, part of which can be found in the literature [41]. As early as 1927, Hartree [42] gave an analytical expression suitable for certain situations:

$$C_{n^*l}^2 = \frac{2^{2n^*}}{n^*(n^*+l)!(n^*-l-1)!} \tag{2.11}$$

The formula is well-defined for hydrogen atoms. For hydrogen-like atoms, it only needs to replace the principal quantum numbers. For the ground state of hydrogen atoms with $E_n = 1/2, n^* = 1, l = m = 0$, it is simple to get $C_{10} = 2$ and ionisation rate will be same as Eq. 2.9.

In 1986, Ammosov et al. [34] considered the condition $n^* \ll l^*$ is satisfied, and the asymptotic coefficient is the only function of the quantum number n under the quasi-classical limit. The ionization rate has a scale factor $En^{*3}/2Z^3 \ll 1$ for a state with a higher magnetic quantum number |m| + 1 compared to a state with |m| , thus the ionization rate is dominant a state at m = 0 . For the s state of the hydrogen atom, the formula can be simplified to Eq. 2.9. Concerning the s state of an arbitrary atom, the ionization rate of linearly polarized light is:

$$W_{\mathrm{lin}}^{\mathrm{adk}} = \sqrt{\frac{3E}{\pi E_0}} \frac{ED^2}{8\pi Z} \exp(-\frac{2Z^3}{3n^{*3}E}), \tag{2.12}$$

where the constant D defined as:

$$D = (\frac{4eZ^3}{En^{*4}})^{n^*} \tag{2.13}$$

This is the commonly used ADK ionization rate. The above description is the total ionization rate of the atom. In addition, we could study electron momentum distribution according to the electron ionization probability at a specific final momentum. For the atom with the ground s state in linearly polarized light, Delone and Krainov [43] applied the Laudau-Dyhne adiabatic approximation of the transition probability amplitude form [44], reaching the electron momentum distribution accurate to the exponential term. Then Krainov [45] started from the KFR theory received the exact same conclusion and provided the exponential antecedent:

$$W(p_{\parallel},p_{\perp}) = \frac{p\omega D^2}{8\pi^3 n^* E}\exp(\frac{2Z^3}{3n^{*3}E})\cdot\exp(-\frac{p_{\perp}^2 Z}{n^* E})\exp(-\frac{p_{\parallel}^2\gamma^3}{3\omega}) \tag{2.14}$$

$p_{\parallel}$ and $p_{\perp}$ are components of photoelectron momentum parallel and perpendicular to the axis of polarization of laser field. Integrates the momentum of Eq. 2.14 will obtain Eq. 2.12.

Alternatively, the Eq. 2.14 could re-write to a convenient way as:

$$\begin{aligned} W(p_{\parallel},p_{\perp}) &= W_0(E)\exp(-\frac{p_{\parallel}^2\omega^2(2I_{\mathrm{p}})^{3/2}}{3E^3} - \frac{p_{\perp}^2(2I_{\mathrm{p}})^{1/2}}{E}) \\ W_0(E) &= \frac{|\mathbf{p}|\omega^2 D^2}{8\pi^3 n^* E}\exp(-\frac{2(2I_{\mathrm{p}})^{3/2}}{3E}) \end{aligned} \tag{2.15}$$

Eq. 2.14 and Eq. 2.15 describe the final momentum distribution of tunnelling electrons. Generally, when the adiabatic condition is satisfied and the Coulomb potential is ignored, the distribution of the final state momentum in the perpendicular electric field direction does not change compared to the tunnel exit. Meanwhile, the transverse distribution could be considered as the Gaussian distribution at the tunnelling exit like Eq. 2.14. Derived from the Eq. 2.14, assuming the initial longitudinal momentum at the exit of the tunnel is 0 [46, 47], the initial distribution of electrons at the exit of the tunnel is expressed as:

$$\begin{aligned} W(E,p_{\perp}) &= W_0(E)W_1(p_{\perp}) \\ W_0(E) &= \frac{ED^2}{8\pi Z}\exp(-\frac{2(2I_{\mathrm{p}})^{3/2}}{3E}) \\ W(p_{\perp}) &= \frac{\sqrt{2I_{\mathrm{p}}}}{\pi E}\exp(-\frac{p_{\perp}^2(2I_{\mathrm{p}})^{1/2}}{E}) \end{aligned} \tag{2.16}$$

where the ionization potential $I_{\mathrm{p}} = Z^2/2n^{*^2}$. The normalization factor of the transverse momentum distribution W_1 is to satisfy $\int_0^{\infty} W_1 2\pi p_{\perp} dp_{\perp} = 1$, that is, the quasi-static ADK rate $W_0(E)$ after integrating the momentum. For the time-dependent field $E(t)$, each moment has a corresponding tunnelling probability $W(t;p_{\perp}) = W(E(t),p_{\perp})$. In particular, we need to emphasiz once more about the different between Eq. 2.14 and Eq. 2.16.

Eq. 2.14 is the final detected momentum distribution, and Eq. 2.16 is the initial distribution of electrons at the tunnel exit derived from the former. Eq. 2.14 is comprised of the transverse and the longitudinal momentum. Eq. 2.16 is only a function of the transverse momentum because the initial longitudinal momentum at the exit of the tunnel is 0. Integrating the momentum in the two directions of Eq. 2.14 obtain the ADK total ionization rate of linearly polarized light (Eq. 2.12). However, Eq. 2.16 integrates the transverse momentum to obtain the ADK rate in a quasi-static field (Eq. 2.10; without period averaged).

2.2.4 Strong-field approximation (SFA)

To achieve an accurate analytical solution utilizing Schrödinger's equation is often impossible. According to specific conditions, people attempt various approximate methods to obtain relevant results of quantum mechanics. For example, the perturbation theory can explain many quantum processes in a weak external field, but it is no longer applicable for the stronger laser field. If we consider the laser field is much stronger than the Coulomb field, then a mathematical processing method using this condition is called the strong-field approximation method (SFA). KFR is the initials of the authors' names of the three papers [27, 30, 31] Keldysh, Faisal, and Reiss. These three articles have carried out pioneering derivation calculations from the same starting point. Later publications regarded them as the foundation of SFA methods (more details see [48]). In addition, other theories deal with ionisation problems in strong fields, such as time-dependent effective range (TDER) [49, 50], Floquet theory [51, 52], and analytical R-matrix theory [53, 54] etc. Each theory makes a corresponding approximation based on its own starting point and applies to different scenarios. In this section, we will briefly present the SFA and the saddle-point method. According to the principles of quantum mechanics, the light field of the Hamiltonian is respectively written as the velocity gauge and the length gauge:

$$H^{\text{vol}} = \frac{1}{2}[-i\nabla + \mathbf{A}(t)]^2 + V_a(r) \tag{2.17}$$

$$H^{\text{len}} = -\frac{\nabla^2}{2} + V_a(r) + \mathbf{E}\cdot\mathbf{r} \tag{2.18}$$

Where $V_a(r)$ is the atomic potential, for hydrogen-like atoms $V_a(r) = -Z/r$, $\mathbf{A}$ is the vector potential, and $\mathbf{E}$ is the electric field. We define the interaction potential between electron and light field as:

$$V_{\text{int}}^{\text{vol}} = i\mathbf{A}\cdot\nabla + A^2/2, V_{\text{int}}^{\text{len}} = \mathbf{E}\cdot\mathbf{r} \tag{2.19}$$

The system Hamiltonian can be written in general:

$$H = -\frac{1}{2}\nabla^2 + V_a(r) + V_{\text{int}} \tag{2.20}$$

The evolution of the wave function of the system satisfies the Schrödinger equation.

$$i\frac{\partial}{\partial t}|\psi\rangle = H|\psi\rangle \tag{2.21}$$

For an atomic system starting from an initial state $|\psi_0\rangle$ evolve to the final state $|\psi_{\text{f}}\rangle = U(t_{\text{f}}, t_0)|\psi_0\rangle$ driven by a laser field, where

$$U(t_{\text{f}}, t_0) = \exp(-i\int_{\text{t}_0}^{t_{\text{f}}} Hdt), \tag{2.22}$$

is the evolution operator from the initial state t_0 to the time t_{f} following the action of the system Hamiltonian in Eq. 2.20.

When an external field is absent from the Hamiltonian, $H_a = -\frac{1}{2}\nabla^2 + V_a(r)$, the corresponding eigenstate can be achieved by solving the stationary Schrödinger equation. The state with energy less than zero is called the bound state, where the initial electron in the ground state is located. Latter, the electronic state will be stimulated by the laser to a higher energy bound state, or the energy higher than zero becomes a free-electron captured by the detector. The free-electron state $|\psi_{\mathbf{p}}\rangle$ with momentum $\mathbf{p}$ is also called a continuous state due to its continuously distributed energy. The measured momentum spectrum in the experiment arises from the free electron, and the probability of detecting an electron with momentum $\mathbf{p}$ is proportional to the composition of the free state $|\psi_{\mathbf{p}}\rangle$ in the final state, that is:

$$M_{\mathbf{p}} = \langle\psi_{\mathbf{p}}|\psi_{\mathrm{f}}\rangle = \langle\psi_{\mathbf{p}}|U(t_{\mathrm{f}}, t_0)|\psi_0\rangle \tag{2.23}$$

Eq. 2.23 is also a strict definition of electron transition amplitude(also called probability amplitude). When performing accurate calculations, it is generally to directly solve the TDSE to obtain the final state wave function $|\psi_{\mathrm{f}}\rangle$, and then apply the Eq. 2.23 to calculate the projection to achieve the momentum spectrum.

Next, we will perform some mathematical processing to get the SFA result. Define the Hamiltonian neglecting the Coulomb potential:

$$H_{\mathrm{f}} = -\frac{1}{2}\nabla^2 + V_{\mathrm{int}}(t) \tag{2.24}$$

It describes the evolution of free electrons in the external field. U_{f} is the corresponding evolution operator, and the eigenstate state is Gordon-Volkov state $|\phi_{\mathbf{p}}^{\mathrm{V}}\rangle$ [55, 56, 57, 58]. The velocity gauge and the length gauge can be revealed in different forms in the non-relativity case:

$$\psi_{\mathbf{p}}^{\mathrm{V,vol}} = |\mathbf{p}\rangle \exp(-iS_{\mathbf{p}}(t)), \tag{2.25}$$

$$\psi_{\mathbf{p}}^{\mathrm{V,len}} = |\mathbf{p} + \mathbf{A}(t)\rangle \exp(-iS_{\mathbf{p}}(t)), \tag{2.26}$$

where

$$S_{\mathbf{p}}(t) = \int^{t} d\tau \frac{[\mathbf{p} + \mathbf{A}(\tau)]^2}{2} \tag{2.27}$$

$|\mathbf{p}\rangle$ represents the plane wave with momentum $\mathbf{p}$. Following the coordinate representation, there is:

$$\langle\mathbf{r}|\mathbf{p}\rangle = \frac{1}{(2\pi)^{3/2}} \exp(i\mathbf{p}\cdot\mathbf{r}) \tag{2.28}$$

Utilizing the Dyson equation[59], the evolution operator of the total Hamiltonian can be expressed as the following equivalent form:

$$U(t, t') = U_a(t, t') - i\int_{t'}^{t} d\tau U(t, \tau)V_{\mathrm{int}}(\tau)U_a(\tau, t') \tag{2.29}$$

$$U(t, t') = U_{\mathrm{f}}(t, t') - i\int_{t'}^{t} d\tau U_{\mathrm{f}}(t, \tau)V_{\mathrm{a}}U(\tau, t') \tag{2.30}$$

Substituting Eq. 2.29 into the Eq. 2.23, another precise expression for transition amplitude can be obtained:

$$M_{\mathbf{p}} = -i\int_{t_0}^{t_{\mathrm{f}}} \langle\psi_{\mathbf{p}}(t_{\mathrm{f}})|U(t_{\mathrm{f}}, \tau)V_{\mathrm{int}}(\tau)|\psi_0(\tau)\rangle d\tau \tag{2.31}$$

The critical step of SFA is to assume that the Coulomb potential effect can be neglected after the electron is ionized and an external electric field drives the electron's motion. Hence, we dismissed the Coulomb potential in the evolution operator and replaced the final electron state with the Volkov state. Eq. 2.31 will be simplified to

$$M_{\mathbf{p}} = -i\int_{t_0}^{t_{\mathrm{f}}} \langle \psi_{\mathbf{p}}^{\mathrm{V}}(\tau)|V_{\mathrm{int}}(\tau)|\psi_0(\tau)\rangle d\tau, \tag{2.32}$$

which is the exact starting point of the KFR theory. The three articles started from Eq. 2.32 and calculated the transition amplitude under a monochromatic light field. Amidst them, Keldysh calculated following the length gauge to achieve the famous Keldysh ionization rate:

$$M_{\mathrm{Keldysh}} \sim \exp\{-\frac{2I_{\mathrm{p}}}{\omega}[(1+\frac{1}{2\gamma^2})\,\mathrm{arsinh}\,\gamma - \frac{\sqrt{1+\gamma^2}}{2\gamma}]\} \tag{2.33}$$

The Keldysh parameter is defined as $\gamma = \omega\sqrt{2I_{\mathrm{p}}}/E$, which can be understood as the ratio of the electron tunnelling time to the light field period. The exponential term is the same as a result achieved via the short-range potential in the PPT article [12]. The physical connotation of this formula is that it can describe the tunnelling limit and the multiphoton process. For the tunnelling limit, the quasi-static approximation, $\gamma \ll 1$, and the Eq. 2.33 can be transformed into the same exponential form as the quasi-static tunnelling probability in Eq. 2.10. The case of $\gamma \gg 1$ performs a multiphoton process, and the ionization probability can be converted into Eq. 2.2.

2.2.5 Saddle-point method

The KFR theory discussed in the previous section started from the approximate ionization rate of the strong field Eq. 2.32, which is an integral function that can be directly calculated mathematically. Fifty years ago, because computers were just started and could not perform complex calculations, people were more inclined to use analytical methods to solve mathematical problems. Nowadays, well-developed processors help us numerically integrate functions with explicit expressions, so Eq. 2.32 following the SFA has been widely used to deal with the problem of atom ionization under an arbitrary finite-length envelope light field. Next, we will introduce a method to transform the integral of Eq. 2.32 into a summation form for approximate processing, providing a classic physical connotation, which method is called the saddle point method in mathematics (for complex numbers also is called the steepest descent method) [60]. Early literature [61, 62] using this mathematical method to solve the integral equation Eq. 2.32, and expanded and summarized by later literature [63, 64] . For the length gauge, substituting the Volkov state and the interaction potential, the Eq. 2.32 can be written as

$$M_{\mathbf{p}} = -i\int_{t_0}^{t_{\mathrm{f}}} e^{i\widetilde{S}_{\mathbf{p}}(t')}\langle \mathbf{p}+\mathbf{A}(t')|\mathbf{r}\cdot\mathbf{E}(t')|\psi_0\rangle dt' \tag{2.34}$$

and the phase given by

$$\widetilde{S}_{\mathbf{p}}(t) = \int^{t} d\tau\{\frac{[\mathbf{p}+\mathbf{A}(\tau)]^2}{2} + I_{\mathrm{p}} \tag{2.35}$$

Suppose the phase $\widetilde{S}_{\mathbf{p}}(t)$ varies much faster than the function $\langle \mathbf{p}+\mathbf{A}(t')|\mathbf{r}\cdot\mathbf{E}(t')|\psi_0\rangle$, the Eq. 2.34 is a rapidly oscillating integral function. The significant contribution of the integral value that appears at the phase changes very slowly called a stable phase point, which shape on the complex plane is like a saddle called a saddle point, satisfying the first derivative of phase concerning time to be zero:

$$\frac{\partial \widetilde{S}_{\mathbf{p}}(t)}{\partial t}|_{t=t_s} = \frac{[\mathbf{p}+\mathbf{A}(t_s)]^2}{2} + I_{\mathrm{p}} = 0 \tag{2.36}$$

It is the saddle point equation. The general idea of the saddle point method is to approximately express Eq. 2.34 as the sum of the integrals near each saddle point, and the integral near the saddle point can be denoted as the production of the integrand function at the saddle point and a specific coefficient. After calculation, the transition amplitude can be expressed as a summation form:

$$M_{\mathbf{p}} \backsim \sum_s \sqrt{\frac{2i\pi}{\widetilde{S}''_{\mathbf{p}}(t_s)}} \langle \mathbf{p}+\mathbf{A}(t_s)|\mathbf{r}\cdot\mathbf{E}(t_s)|\psi_0\rangle e^{i\widetilde{S}_{\mathbf{p}}(t_s)} \tag{2.37}$$

The summation traverses all saddle points. In using the saddle point method, some approximation conditions are often not well satisfied and not strict, so the final formula is numerically not wholly consistent with the original formula. However, the approximated formula is sufficient to describe the performance of the original function, or it can be considered that only a coefficient factor is missing. In the case of considering the Coulomb potential, the reference [64] gives correction of the transition amplitude with Coulomb potential:

$$\begin{aligned} M_{\mathbf{p}} &\backsim P(t_s) e^{i\widetilde{S}_{\mathbf{p}}(t_s)} \\ P(t_s) &= \sum_s \frac{(2I_{\mathrm{p}})^{5/4}}{2^{1/2}\mathbf{E}(t_s)[\mathbf{p}+\mathbf{A}(t_s)]} \end{aligned} \tag{2.38}$$

It can be seen solution of the Eq. 2.36, the saddle point $t_s = t_{\mathrm{r}} + it_{\mathrm{i}}$, is a complex number, so the phase factor of Eq. 2.34 is the integral of the complex variable function under the saddle point method. The integration path can be divided into two parts considering as an analytical function:

$$\int_{-\infty}^{t_s} = -\int_{t_s}^{\infty} = -\int_{t_s}^{t_{\mathrm{r}}} - \int_{t_{\mathrm{r}}}^{\infty} \tag{2.39}$$

Integrate directly from the saddle point (t_s) to the real part (t_{r}) and then from the real part to infinity. So the phase factor could be divided into two parts:

$$\begin{aligned} \widetilde{S}_p(t) &= \Phi_s^t + \Phi_s \\ \Phi_s^t &= -\int_{t_s}^{t_{\mathrm{r}}} \{\frac{[\mathbf{p}+\mathbf{A}(\tau)]^2}{2} + I_{\mathrm{p}}\} d\tau \\ \Phi_s &= -\int_{t_{\mathrm{r}}}^{\infty} \{\frac{[\mathbf{p}+\mathbf{A}(\tau)]^2}{2} + I_{\mathrm{p}}\} d\tau \end{aligned} \tag{2.40}$$

The first term Φ_s^t is from the t_s to the t_r, which physical correspondence as electron tunnelling through the barrier, where the real part is the initial tunnelling phase and imaginary part presents tunnelling probability [65]. The second integration Φ_s is achieved in real-time. The ionization rate only depends on the Φ_s^t because the Φ_s is the phase accumulation after the ionization. Transition amplitude can be written as:

$$M_{\mathbf{p}} \backsim \sum_s P(t_s)\exp(i\Phi_s^t)\exp(i\Phi_s) \tag{2.41}$$

Furthermore, the imaginary value presents the tunnelling probability defines as:

$$\widetilde{S}_p(t)^s = -\mathrm{Im}\int_{t_s}^{t_\mathrm{r}}\{\frac{[\mathbf{p}+\mathbf{A}(\tau)]^2}{2}+I_\mathrm{p}\}d\tau \tag{2.42}$$

For a classical physical process of SFA, electrons tunnel from moment t_r, and then behave the classical motion in the external field skipping the Coulomb potential, the electron with the final state momentum $\mathbf{p}$ derived from the initial momentum with Eq. 2.56:

$$\mathbf{p}_0 = \mathbf{p}+\mathbf{A}(t_\mathrm{r}) \tag{2.43}$$

The initial position of the electron at the ionization time t_r can be determined using the hypothesis in the virtual time theory [64], which supposes that the electron moves in the barrier during the period from t_s to t_r follow the quantum trajectory. The definition of the quantum trajectory need to satisfy the following two Boundary conditions: 1) The real part of the electron at the beginning of the tunnel is zero, that is, $\mathrm{Re}(\mathbf{r}(t_s)) = 0$; 2) The classical quantity of the electron at the tunnel exit should be a real number, $\mathrm{Im}(\mathbf{r}(t_\mathrm{r})) = \mathrm{Im}(\mathbf{p}(t_\mathrm{r})) = 0$. Quantum trajectories completing the above conditions can be constructed

$$\mathbf{r}_q(t) = \int^t \mathbf{A}(\tau) - \mathrm{Re}[\int^{t_s}\mathbf{A}(\tau)d\tau] \tag{2.44}$$

And the initial position of the tunnel exit can be express as integration motion of under the barrier:

$$\mathbf{r}_0 = \mathbf{r}_q(t_\mathrm{r}) = \mathrm{Re}[\int_{t_s}^{t_\mathrm{r}}\mathbf{A}(\tau)d\tau] \tag{2.45}$$

Now, from the saddle point SFA, we could extract ionization information inclu initial velocity $\mathbf{v}_0$, initial position $\mathbf{r}_0$, ionization rate, tunnelling rate $\widetilde{S}_p(t)^s$, tunnelling period and transition amplitude M_p.

Next, we show the calculation process of the SFA saddle point equation with an example: Assuming that the light field is along the z-direction, $\mathbf{A}_z(t) = Et$, the light field can be considered as an electrostatic field in the quasi-static limit. Substituting into the saddle point equation 2.36:

$$\frac{1}{2}[(p_z - Et_\mathrm{r} - iEt_\mathrm{i})^2 + p_x^2] + I_\mathrm{p} = 0 \tag{2.46}$$

Here, we only considered the xz plane, and the saddle point can be reached:

$$t_{\mathrm{r}} = \frac{p_z}{E}, \; p_{0\mathrm{z}} = p_z - Et_{\mathrm{r}} = 0 \tag{2.47}$$

Substitute 2.43 to get the initial momentum:

$$p_{0\mathrm{x}} = p_x, \quad p_{0\mathrm{z}} = p_z - Et_{\mathrm{r}} = 0 \tag{2.48}$$

It seems that the initial longitudinal momentum is zero when satisfying the quasi-static condition. For the initial position:

$$r_z = \mathrm{Re}[\int_{t_s}^{t_{\mathrm{r}}} -E\tau d\tau] = -\frac{Et_{\mathrm{i}}^2}{2} \approx -\frac{I_{\mathrm{p}}}{E} \tag{2.49}$$

Tunnelling possibility from the imaginary part of tunnelling phase:

$$\begin{aligned} \widetilde{S}_p(t)^s &= -\mathrm{Im}\int_{t_s}^{t_{\mathrm{r}}} [\frac{(p_z - E\tau)^2 + p_x^2}{2} + I_{\mathrm{p}}]d\tau \\ &= \frac{(p_x^2 + 2I_{\mathrm{p}})^{3/2}}{3E} \end{aligned} \tag{2.50}$$

And the ionization rate:

$$\begin{aligned} W &\propto \exp(-\frac{2(p_x + 2I_{\mathrm{p}})^{3/2}}{3E}) \\ &\propto \exp(-\frac{2(2I_{\mathrm{p}})^{3/2}}{3E})\exp(-\frac{p_x^2\sqrt{2I_{\mathrm{p}}}}{E}) \end{aligned} \tag{2.51}$$

In principle, the SFA can be applied for the general form of the light field, but the initial longitudinal velocity at the tunnel exit is not always zero, and the relationship between the ionization probability and the initial transverse velocity is no longer a Gaussian distribution with the centre at zero. These differences will cause the SFA results to be inconsistent with the adiabatic method when the quasi-static conditions are not met, and this inconsistency is collectively referred to as a non-adiabatic phenomenon.

2.2.6 CTMC and QTMC method

Semi-classical refers to classic images to describe electrons' movement and give classic particles non-classical phase information. The ionized electron can be considered a classic particle with a definite orbit, and its motion satisfies the classical Newton equation following Coulomb potential and external field. Finally, the electrons with the same final state will interfere to produce a momentum spectrum. The classical model was initially developed by Corkum [35, 36] in dealing with the ionization of long-wavelength laser fields. The laser is no longer regarded as a photon in a strong field with a longer wavelength than a classical electromagnetic field describing the light field. Following the action of an external field, electrons tunnel into free electrons and then continue to be driven by the external field for classical motion. The three-step model method opened the research era of using classical particles to describe the movement of electrons in a strong field at the atomic scale.

At first, Corkum's model described the second step only considering the effect of the external electric field during the electron propagation. Successively, the Coulomb force's influence is involved in the classical-trajectory Monte Carlo (CTMC) model. In 1997, Hu et al. [46] extended the three-step model to consider the electron transverse momentum distribution at the moment of tunnelling and the after tunnelling affected by the Coulomb force, successfully explaining the angular distribution structure of high-energy electrons. It is the foundation of the CTMC method. Furthermore, Li et al. [66, 67] proposed quantum trajectory Monte Carlon (QTMC) in 2014. Utilizing the idea of Feynman path integral and considering the interference effect between electrons that reach the same final state momentum through different paths, providing phase information to the classical particles, which can well explain the two-dimensional electron momentum spectrum.

2.2.6.1 Classical Propagation and Phase

Under quasi-static conditions, it is supposed that the electric field at each tunnelling moment is a constant value, obtaining tunnel exit position, exit momentum distribution, and the ionization rate. After the initial conditions are determined, the electron propagation is described by an utterly classical model. Electron motion satisfies the Newtonian equation of motion as:

$$\frac{d^2\mathbf{r}}{dt^2} = \mathbf{E}(t) - \frac{Z\mathbf{r}}{r^3} \tag{2.52}$$

Or written as a first-order differential equations:

$$\begin{aligned} \frac{d\mathbf{p}}{dt} &= \mathbf{E}(t) - \frac{Z\mathbf{r}}{r^3} \\ \frac{d\mathbf{r}}{dt} &= \mathbf{p} \end{aligned} \tag{2.53}$$

In practical calculations, the external electric field is generally a finite pulse. The electron's movement is only carried out under the Coulomb force after the end of the pulse, described by Kepler orbit. If the electron's energy is less than zero, the electron orbit should be a closed ellipse and the electrons will eventually be bound to the Rydberg state without being ionized [68, 69]. Electrons with energy greater than zero are hyperbolic orbits, and the asymptotic momentum at infinity obtained by analysis is used as the momentum captured by the detector. Knowing the momentum p_f and position r_f at the end of the laser, derived three conserved quantities: energy, angular momentum, and Laplace–Runge–Lenz (LRL) vector,

$$\begin{aligned} \frac{p_\infty^2}{2} &= \frac{p_\mathrm{f}^2}{2} - \frac{Z}{r} \\ \mathbf{L} &= \mathbf{r}_\mathrm{f} \times \mathbf{p}_\mathrm{f} \\ \boldsymbol{\alpha} = \mathbf{p}_\mathrm{f} \times \mathbf{L} &- \frac{Z\mathbf{r}_\mathrm{f}}{r_\mathrm{f}} \end{aligned} \tag{2.54}$$

The final state momentum is expressed as [69, 70]:

$$\mathbf{p}_\infty = p_\infty \frac{p_\infty(\mathbf{L}\times\boldsymbol{\alpha}) - \boldsymbol{\alpha}}{1 + p_\infty^2 L^2} \tag{2.55}$$

If we ignore the Coulomb potential, the energy of the tunnelled electrons must be greater than zero, and all of them will eventually reach the detector. The final state electron momentum can be purchased directly from the equation of motion:

$$\begin{aligned} \mathbf{p}_\infty = \mathbf{p}_\mathrm{f} &= \mathbf{p}_0 - \int_0^\infty \mathbf{E}(t)dt \\ &= \mathbf{p}_0 - \mathbf{A}(t_0) \end{aligned} \tag{2.56}$$

Where t_0 represents the electron ionization time, p_0 is the initial momentum of the ionization, and the vector potential $\mathbf{A}$ satisfies $E = \partial\mathbf{A}/\partial t$, which physically needs to satisfy that the vector potential is zero before and after the laser field, $A(\pm\infty) = 0$.

After involving the Coulomb potential, some of the electrons' final state energy may be less than zero, others momentum will deviate from the result of Eq. 2.56, even a considerable deviation may occur because of being scattered by the Coulomb potential. The CTMC method sums of the ionization probabilities of the electrons with the same final momentum $\sum W^j(t_0, p_\perp)$, where the summation traverses all electrons of j. The statistical result exhibits the final angular distribution structure caused by the initial longitudinal momentum. The QTMC method gives phase information to each electron and superimposes the probability amplitudes of electrons that reach the same final momentum. The probability that the final momentum $\mathbf{p}$ is

$$M_\mathbf{p} = \sum_j \sqrt{W^j(t_0, p_\perp)}\exp(i\Phi_j), \tag{2.57}$$

it is based on the Feynman path integral idea [71], it was also used in the strong field domain [72]. In the supplementary material of literature [66], we could find the derivation process of the orbital phase of each electron Φ, and the result is:

$$\Phi = -\int_{t_0}^\infty [\frac{v(t)^2}{2} - \frac{Z}{r(t)} + I_\mathrm{p}]dt \tag{2.58}$$

The integral term is the total energy of the electron. In the actual calculation, the Eq. 2.58 rewrite as a in a differential formula:

$$\frac{d\Phi}{dt} = -[\frac{v(t)^2}{2} - \frac{Z}{r(t)} + I_\mathrm{p}] \tag{2.59}$$

It could solved with differential equation Eq. 2.53 together. Eq. 2.57 is the same as Eq. 2.42, so we have connected the SFA and the semi-classical theory. The only difference is that the tunnelling probability amplitude of QTMC is a real number, but $P(t_s)\exp(i\Phi_s^t)$ is a complex number, which means that the initial phases of different orbits are not necessarily the same. The results of Eq. 2.49 to Eq. 2.51 contain the same exponential factors of ionization rate utilized in the QTMC model, confirming the consistency and effectiveness of these methods.

Recently, Shvetsov-Shilovski et al. [73] proposed the semi-classical two-step (SCTS) model, which is essentially the semi-classical method discussed in this chapter. This work re-derives the orbital phase, pointing out the omissions in the original derivation process [66] and made corrections. The orbital phase can finally be written as:

$$\Phi = -\mathbf{v}_0 \cdot \mathbf{r}_0 + I_\mathrm{p} t_0 - \int_{t_0}^{t_\mathrm{r}} [\frac{v(t)^2}{2} - \frac{2Z}{r(t)}]dt + \Phi_\mathrm{f}^C(t_\mathrm{f}) \tag{2.60}$$

The progressive Coulomb correction term $\Phi_\mathrm{f}^C(t_\mathrm{f})$ can be expressed by the electron velocity $\mathbf{p}_\mathrm{f}$, position $\mathbf{r}_\mathrm{f}$, and angular momentum l at the end of the laser (see [73] for detailed derivation):

$$\Phi_\mathrm{f}^C(t_\mathrm{f}) = -Z\sqrt{b}[\ln g + \operatorname{arsinh}(\frac{\mathbf{r}_\mathrm{f} \cdot \mathbf{p}_\mathrm{f}}{g\sqrt{b}})], \tag{2.61}$$

where $b = 1/\sqrt{2I_\mathrm{p}}$, $g = \sqrt{1 + 2I_\mathrm{p} l^2}$.

2.2.6.2 Steps of a CTMC Method

The semi-classical method is mainly divided into the following steps in the specific numerical calculation implementation:

1) Prepare sample electrons. One method takes time points uniformly from the beginning to the end of the laser and then evenly takes points for the initial transverse velocity at each moment. Calculate the ionization rate corresponding to each moment and initial transverse velocity (Eq. 2.16), representing the number of tunnelling electrons ionized at this moment and with the initial velocity is proportional to the ionization rate. However, we only use one electron as a representative and multiply it by the Eq. 2.16) as a weight.

The uniform sampling point has two disadvantages: One is that the non-physical interference structure caused by the periodicity of the uniform points may appear. On the other hand, in order to obtain the convergent momentum spectrum, dense sampling points and a larger number of sample points are required. A commonly used improvement method is the Monte Carlo method, uniformly randomly sampled in the time and the initial transverse momentum to compute the ionization moment and initial transverse momentum. This method can use fewer samples to obtain a converged momentum spectrum with higher efficiency. Generally, the typical sample order of magnitude is 10^9.

2) After the ionization time and initial transverse velocity of the electrons are determined by random sampling. Next, solving the differential equations Eq. 2.53 and Eq. 2.59, we can obtain the position, velocity and phase accumulation of the electron at the end of the laser. In addition, the process of solving the differential equation can be recorded to obtain the trajectory of the electron driven by the electric field. Finally, the final state electron momentum can be calculated by the Kepler formula (Eq. 2.55).

3) Finally, use the Eq .2.57 to calculate the ionization probability of electrons with the same final momentum. In practice, we consider that the final momentum is distributed in a small rectangular area $[p_x - \Delta p_x/2 \ p_x + \Delta p_x/2, p_z - \Delta p_z/2 \ p_x + \Delta p_z/2]$. Generally, for a laser with a longer wavelength, the electron phase oscillates faster, or the fringes in momentum space are denser, so smaller binning is required. Typically, 1/10 of the

momentum space fringe spacing under a certain laser parameter can be taken as binning area range. The small binning region leads to an insufficient number of electrons falling in. More sample electrons are required to achieve a certain statistic, which consumes more computation resources.

2.3 Propagation and return of the quasi-free electron

The widely accepted re-scattering model can explain the electron motion under the laser field, also called the three-step model or simple man's model (SMM) proposed by Corkum. The model divides the formation of high-energy photoelectrons into three steps:

(1)The bound state electrons tunnelling through the Coulomb barrier distorted by the laser field form free electrons;

(2)The electrons are accelerated and returned, which have the opportunity to return to the vicinity of the nucleus following the action of the laser field;

(3) The returned electrons collide with the atoms elastically, earning more energy, finally escaping from the Coulomb potential, captured by the detector.

We will intuitively explain the progress mathematically. The time depends electric field could define as:

$$\mathbf{E}(t) = E_0(t)\begin{pmatrix} 0 \\ -\epsilon\sin(\omega t) \\ \cos(\omega t)\end{pmatrix} \tag{2.62}$$

Where ϵ is the ellipticity parameter, ϵ =0 for linear polarisation, $\epsilon = \pm 1$ for circular polarisation and $-1 < \epsilon < 0$ and $0 < \epsilon < 1$ for elliptical polarisation. The motion in the laser field can be described by the Newtonian equation of motion:

$$\frac{d^2\mathbf{S}}{dt^2} = \frac{q\mathbf{E}}{m} \tag{2.63}$$

The momentum of electron in the oscillating electric field is express as under atomic unite:

$$\mathbf{p}(t_\mathrm{i}, t) = -\int_{t_\mathrm{i}}^{t} \mathbf{E}(t')dt' = \mathbf{A}_\mathrm{i} - \mathbf{A} \tag{2.64}$$

The electrons tunnels barrier at t_i time and propagate with laser field until time t, the vector potential of the laser as $\mathbf{A}(t) = \int \mathbf{E}(t')dt'$. When the electron reach the detector at $t \to \infty$, the electron gains the momentum at the time t_i from the vector potential.

$$\mathbf{p}_\mathrm{dir}(t_\mathrm{i}) = \mathbf{p}(t \to \infty, t_\mathrm{i}) = -\int_{t_\mathrm{i}}^{\infty} \mathbf{E}(t')dt' = \mathbf{A}(t_\mathrm{i}), \tag{2.65}$$

where we usually assume the vector potential vanishes to zero at $t \to \infty$. The finial momentum of electron directly ionized without re-collision in the linear polarization ($\epsilon = 0$) could express as

$$\mathbf{p}_\mathrm{dir}(t_\mathrm{i}) = \mathbf{A}(t_\mathrm{i}) = -\int_{t_\mathrm{i}}^{\infty} E_0\cos(\omega t')dt' = \frac{E_0}{\omega}\sin(\omega t_\mathrm{i}) \tag{2.66}$$

Here, we could see that the final momentum is mainly dependent on the ionization time. If we neglect the initial velocity at the tunnel exit, the maximum momentum of direct electron could reach is:

$$\mathbf{p}_{\mathrm{dir,max}} = \frac{E_0}{\omega} = 2\sqrt{U_{\mathrm{p}}}, \tag{2.67}$$

and the maximum kinetic energy is:

$$E_{\mathrm{dir,max}} = (\frac{E_0}{\omega})^2/2 = 2U_{\mathrm{p}} \tag{2.68}$$

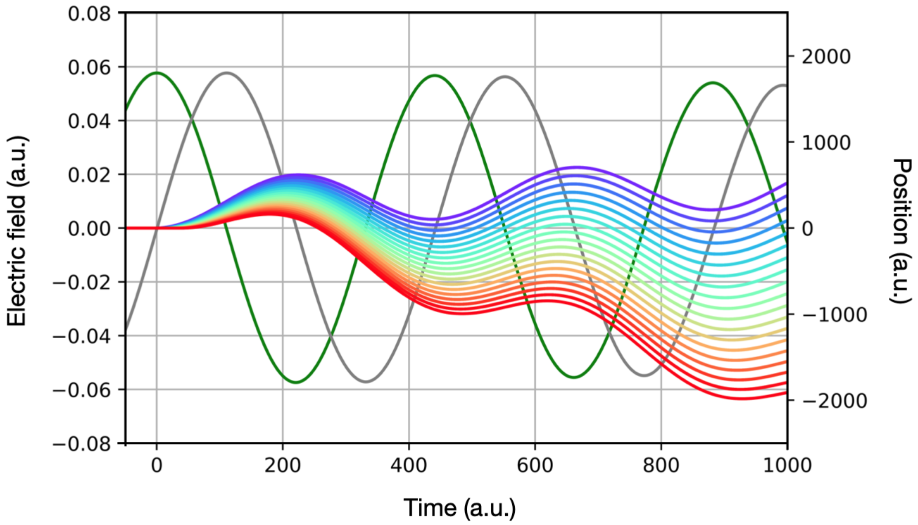

Figure 2.3: **Illustration of electron trajectories**. electric field and vector potential of the laser at intensity of 1.2×10^{14} W/cm^2 are indicating with green and grey line respectively, the classical electron trajectories are incicated with purple to red line indicated the different birth time.

2.3.1 Returning electron

In the second step of the three-step model, the classical motion of the electron oscillating under the laser field has the opportunity to return to the vicinity of the nucleus. We could integrate to the Eq. 2.63 get an expression of momentum under the oscillated laser field:

$$\mathbf{p}(t, t_{\mathrm{i}}) = \frac{E_0}{\omega} \begin{pmatrix} 0 \\ -\epsilon[\cos(\omega t_{\mathrm{i}}) - \cos(\omega t)] \\ \sin(\omega t_{\mathrm{i}}) - \sin(\omega t) \end{pmatrix} + \mathbf{v_0}, \tag{2.69}$$

and the electrons' position follow as:

$$\mathbf{S}(t,t_{\mathrm{i}})=\frac{E_0}{\omega^2}\begin{pmatrix}0\\ -\epsilon[\cos(\omega t_{\mathrm{i}})(\omega\Delta t)-\sin(\omega t)+\sin(\omega t_{\mathrm{i}})]\\ \sin(\omega t_{\mathrm{i}})(\omega\Delta t)+\cos(\omega t)-\cos(\omega t_{\mathrm{i}})\end{pmatrix}+\mathbf{v}_0\Delta t+\mathbf{S_0} \tag{2.70}$$

with $\Delta t = t_{\mathrm{r}} - t_{\mathrm{i}}$, The $\mathbf{v}_0$ stands for the initial velocity and $\mathbf{S}_0$ is the initial position of the electron at the tunnel exit. Assuming that the initial velocity is equal to zero and the position of the nucleus is the origin of the coordinates, considering the linear polarisation case, when the electron return to the ionic core at the return time t_{r} and mathematically satisfy the condition $\mathbf{S}(t_{\mathrm{r}}, t_{\mathrm{i}}) = 0$, we could get :

$$\sin(\omega t_{\mathrm{i}})(\omega\Delta t)+\cos(\omega t_{\mathrm{r}})-\cos(\omega t_{\mathrm{i}})=0 \tag{2.71}$$

Here, we have two variables but only one equation, the pairs of birth time t_{i} and return time t_{r} could be solved numerically and create a set of solutions instead of a unique one. Considering the $\phi = \omega t$ as a phase of the carrier field cycle, we could rewrite as phase format as:

$$\sin(\phi_{\mathrm{i}})(\Delta\phi)+\cos(\phi_{\mathrm{r}})-\cos(\phi_i)=0 \tag{2.72}$$

With the $\Delta\phi = \phi_{\mathrm{r}} - \phi_{\mathrm{i}}$, considering the cosine format of the electric field, the pyhsics solution could be only found for birth time at $0 \leq \phi_{\mathrm{i}} \leq \pi/2$ and returning time between $\pi/2 \leq \phi_{\mathrm{r}} \leq 2\pi$. The electron bon before the peak of the electric field $-\pi/2 \leq \phi_{\mathrm{r}} \leq 0$ doesn't cause any suitable solution($\phi_{\mathrm{i}} < \phi_{\mathrm{r}}$).

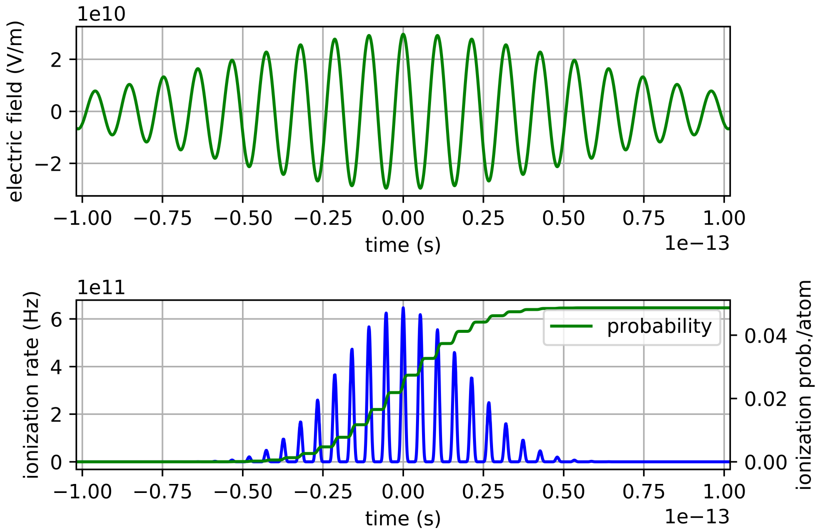

Figure 2.4: **Illustration of electron ionization rate**. Ionization Rate of water molecule with 100 fs 1.2×10^{14} W/cm^2 laser pulse

The kinetic energy of the returning electron could be calculated from Eq. 2.63 as

$$E_{\mathrm{r}}(\phi_{\mathrm{r}},\phi_{\mathrm{i}})=2U_{\mathrm{p}}(\sin(\phi_{\mathrm{i}})-\sin(\phi_{\mathrm{r}}))^2 \tag{2.73}$$

As increasing the birth time ϕ_i, the returning energy firstly increase then reduced, the maxmun of returning energy could be found at $\phi_\mathrm{i} \approx 0.1\pi$ and returning at $\phi_\mathrm{i} \approx 1.4\pi$, corresponding the $E_\mathrm{r} = 3.175U_\mathrm{p}$. Another important concept is the defination of the long trajectory and short trajectory, the same returning energy could be achieved by different set of solution of ϕ_r and ϕ_i which indicate the different ionization pathway. We involve long trajectory and short trajectory according the electron birth time to distinguish two solutions. The long trajectory is the $\phi_\mathrm{i} < \phi_{\mathrm{i,E_{i,max}}}$ and $\phi_\mathrm{r} > \phi_{\mathrm{r,E_{r,max}}}$ and short trajectory is $\phi_\mathrm{i} > \phi_{\mathrm{i,E_{i,max}}}$ and $\phi_\mathrm{r} < \phi_{\mathrm{r,E_{r,max}}}$.

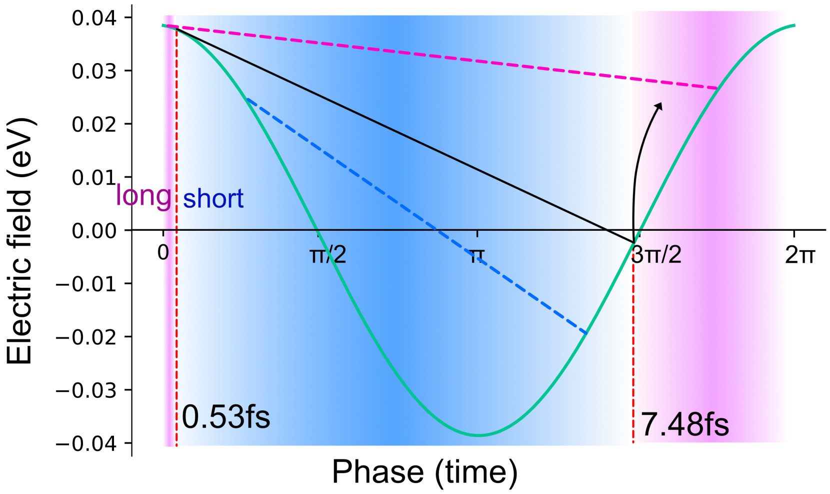

Figure 2.5: **Illustration of electron long and short trajectories on top of the laser field.** The electron long and short trajectory areas are plotted according to the different borning and returning times on top of the laser's electric field. The pink region represents the long trajectory region and the blue area symbolizes the short trajectory. The green line shows the electric field. Black trace illustrates the highest returning energy and the boundary between the long and short trajectory.

2.3.2 Rescattering electron

After tunnelling the barrier and returning to the ionic core, we arrive at the third step of Corkum's three-step model. Three main physical processes are leading in the recollision. The returned electron wave packet could either 1) recombine with the parent ion, leading to emitted of high-energy photons, commonly known as the high-order harmonic generation (HHG), 2) inelastically rescatter to further ionize the parent ion to dication, known as the non-sequential double ionization (NSDI), or 3) elastically scatter off the parent ion without energy loss, obtaining kinetic energy through a laser field, called high energy ATI (HATI). Our LIED technique is based on analyzing elastically rescattered electrons that encode the geometrical information of the molecule.

2.3.3 Re-combination

The returning electrons may be re-captured by the atomic potential and emitter high-frequency photons, which energy come from multiple photons absorbed during the ionization process. Considering the conservation of parity and energy, the frequency of the emitted photon must be an odd multiple of the laser frequency [74], and the high order harmonics can be as high as dozens or even hundreds. Only one year after the invention of the laser, Framken et al. [75] used a 694.3 nm laser to discover the frequency doubling effect with a quartz crystal. Since then, higher-order nonlinear effects such as third harmonics and four-wave mixing [74] have also been discovered. Traditional methods are challenging to achieve high order harmonics because it is difficult to find suitable nonlinear crystals and the efficiency of high-order harmonics is extremely low. In 1987, McPherson et al. [76] firstly used an ultraviolet light (248 nm) source to observe high-order harmonic radiation in the noble gas. The harmonic intensity first dropped drastically from the low-energy edge to the high-energy, called the ”perturbation” region. Then there is a broad ”platform area” with little difference in radiation intensity, and then the radiation intensity drops rapidly, forming the ”cut-off area”.

The traditional perturbation theory cannot explain the appearance of the high-order harmonic ”platform area” cannot be explained by the traditional perturbation theory. Instead, the three-step model can perfectly describe it. After the electron returns, it recombines with the parent ion and radiates photons of corresponding energy. The highest photon energy of the harmonic radiation in the cut-off region is $I_\mathrm{p} + 3.17U_\mathrm{p}$, where $3.17U_\mathrm{p}$ is the maximum kinetic energy of the electron returning to the nucleus. This is consistent with the results obtained by Krasue et al. [77] by solving TDSE. The related theoretical and experimental research spring up after the discovery of HHG, [32, 78, 79, 80, 81], such as the acquisition of coherent X-ray radiation in the ”water window” band [82, 83] and the shortest single attosecond pulse that can be achieved [84]. Meanwhile, HHG has many vital applications in molecular reconstruction [85], so they have been receiving extensive attention from physicists.

2.3.4 Inelastic re-scattering

Another possibility for electrons to collide with their parent ions is the inelastic rescattering process. In the 1980s, French scientist L'Huillier [86] with her colleagues discovered an unexpected behaviour in a double ionization experiment. A ”knee” structure appeared with laser intensity increased but did not attract much attention. By the 1990s, Fittinghoff et al. [87] and Walker et al.[88] made accurate measurements of single and double ionization ion yields with light intensity, combining theoretical analysis and finally revealed that the ”knee” structure originated from the non-sequential double ionization (NSDI).

Theoretically, the single active electron approximation (SAE) model supposes that atoms undergo double ionization in two steps: first, the atom ionizes an electron within the laser field to form a cation; then, it continues to ionize another electron and becomes a dication. These two steps are independent of each other and not related. The yield of cation is provided by ADK theory [89], while the yield of dication uses cation as a source, only replacing the atom's ground state's binding energy to a cation. However, it is not comparable for the experimental data [88] with the SAE theory. The measured yield of cation and dication at high laser intensity ($>5\times10^{15}$ W/cm^2) are in good agreement with the theoretical results. Nevertheless, when the laser intensity is less than the saturated intensity of single ionization, the measured dications yield increases rapidly with the light intensity, which exceeds the theoretical calculation result by 5-6 order of magnitude [88]. While near the saturated light intensity of single ionization, the excess dications production begins to decrease and the ”knee” structure appears on the overall experimental curve.

Theoretical physicists have proposed different models to explain the physical progress behind the ”knee” structure, mainly including re-scattering models [36, 89], shake-off models [87], and collective tunnelling models [90]. People verified the mechanism of NSDI with further experiments. First, the yields of dication helium in linearly polarized light are much higher than the sequential double ionization prediction, while elliptically polarised light fits it well. This is in line with the rescattering model because the first ionized electron rescattering probability is related to the laser polarization. Furthermore, the two groups used advanced COLTRIM technology to discover the double-peak structure in the longitudinal momentum spectrum of dications [91, 92], which directly denied the shake-off model and collective tunnelling model and became a strong support for the rescattering theory.

The rescattering theory correctly describes the NSDI process: The electron returns and collides to the vicinity of the atom inelastically, exciting the inner shell electron so that another electron is ionized or excited to a higher Rydberg state to be further ionized. Both the shake-off model and the collective follow-through model predict that the momentum spectrum of dication is a single-peak structure with a very narrow distribution, contrary to experimental observations. On the other hand, the double-peak structure means that the two electrons that undergo double ionization are highly likely to be emitted along the same direction of the laser field. Experiment [91] also approved that the two electrons are apparently correlated, which further supports the rescattering theory [93, 94]. Therefore, the NSDI caused by rescattering is finally recognized as the dominant mechanism for forming knee-shaped structures.

2.3.5 Elastic re-scattering

The returning electron also elastically scatter the parent ion without energy loss as two rigid bodies collide. The returning electron as an incident beam scatters off the ion and exits with rescattering angle Θ_r, in the linear polarization, we could describe the rescattering motion mathematically as:

$$\mathbf{p}_{\mathrm{resc}}(\phi_\mathrm{i},\phi_\mathrm{r},\Theta_\mathrm{r}) = \frac{E_0}{\omega}[(\sin\phi_\mathrm{i}-\sin\phi_\mathrm{r})\begin{pmatrix}\cos\Theta_\mathrm{r}\\ \sin\Theta_\mathrm{r}\end{pmatrix}+\begin{pmatrix}\sin\phi_\mathrm{r}\\ 0\end{pmatrix}] \tag{2.74}$$

The first term is the returning momentum before the rescattering, folded with the influence of the scattering angle. The second term could understand as a direct photoelectron momentum after the rescattering. The final kinetic energy of the electron could express as:

$$E_{\mathrm{resc}}(\phi_{\mathrm{i}}, \phi_{\mathrm{r}}, \Theta_{\mathrm{r}}) = 2U_{\mathrm{p}}[\sin^2\phi_{\mathrm{i}} + 2\sin\phi_{\mathrm{r}}(1 - \cos\Theta_{\mathrm{r}})(\sin\phi_{\mathrm{r}} - \sin\phi_{\mathrm{i}})] \tag{2.75}$$

The maximum rescattering energy could achieve at the initial tunneling time at $\phi_{\mathrm{i}} \approx 0.08\pi \approx 0.04\tau_{\mathrm{cycle}}$, rescattering at time $\phi_{\mathrm{r}} \approx 1.45\pi \approx 0.73\tau_{\mathrm{cycle}}$ and rescattering angle at $\Theta_{\mathrm{r}} = 180^o$ so called back-scattering electrons, resulting in

$$E_{\mathrm{resc,max}}(180^o) = 10U_{\mathrm{p}} \tag{2.76}$$

It also should be noticed that the time pair for the maximum rescattering energy ($E_{\mathrm{resc}} = 10U_{\mathrm{p}}$; $\phi_{\mathrm{i}} \approx 0.08\pi, \phi_{\mathrm{r}} \approx 1.45\pi$) didn't correspondence the time pair for the maximum returning energy ($E_{\mathrm{r}} = 3.175U_{\mathrm{p}}$; $\phi_{\mathrm{i}} \approx 0.1\pi, \phi_{\mathrm{r}} \approx 1.4\pi$).

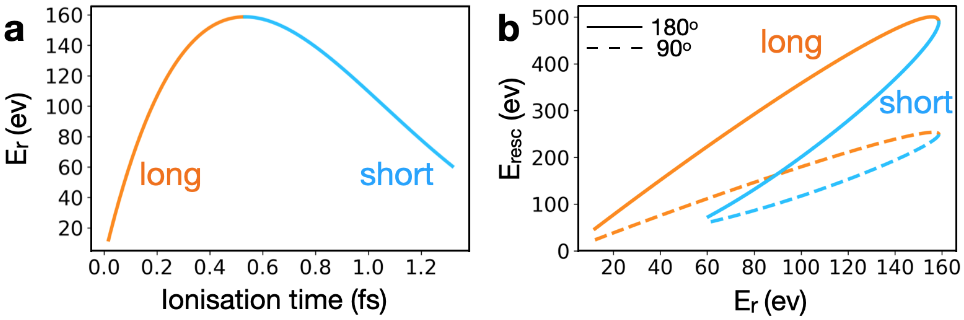

Figure 2.6: **Long and short trajectories.** Using the $U_{\mathrm{p}} = 50$ eV as an example. **a** Return energy E_{r} as function of ionization time for long and short trajectories. **b** The final kinetic energy of the electron after re-scattering E_{resc} is plotted as a function of E_{r} for various scattering angles Θ_{r} for both trajectories.

2.3.6 Summary

Depending on the birth phase, if the electrons no longer interact with atoms after tunnelling, they will quiver back and forth in the laser field and obtain a certain amount of drift energy Eq. 2.66 after the laser pulse terminates. It can be seen that the kinetic energy is only related to the laser phase and the tunnelling moment t_{i}. Therefore, the electron tunnelling at the peak position of the electric field ($E = E_0\cos(\omega t)$) obtains the smallest kinetic energy while obtaining the highest energy at the zero point of the electric field. On the other hand, according to the ADK theory, the ionization probability of an electron is most prominent at the peak of the laser field, then rapidly decays until the field drops to zero. Constructing the energy spectrum within the range exhibits an exponential decay trend, this part of the electron is called "direct electron" with the maximum kinetic energy of $2U_{\mathrm{p}}$. Moreover, if the electron returns to the vicinity of the atom and elastically scatter with it, the electron will gain more energy due to the collision. The final energy may greater than $2U_{\mathrm{p}}$, between $2U_{\mathrm{p}}$ - $10U_{\mathrm{p}}$. Therefore, a platform structure is exhibited in this area, falling rapidly afterwards and cutting off at $10U_{\mathrm{p}}$, called "rescattering electrons". Considering the relationship between U_{p} and laser intensity and wavelength, the cut-off energy of $2U_\mathrm{p}$ is often used to calibrate the laser intensity at a certain wavelength in experiments.

2.4 Imaging molecular structure with LIED

Laser-induced electron diffraction is a method based on self-imaging a target structure using the molecule's own emitted attosecond electron wave packet during the laser-induced re-collisions process. It is a laser-based single-electron diffraction method that combines sub-atomic picometre and femtosecond spatiotemporal resolution. Three steps could describe the process shown in Fig. 2.7: (i) The ground-state bound electrons first undergo tunnelling ionization through the barrier formed by the laser and the Coulomb field. (ii)The ionized electron is then accelerated in the laser electric field and gains energy. As the laser field reverses, the electron is pulled back to the vicinity of the parent ion by the electric field. (iii) Elastically rescattering to parent ion in whole directions and the momentum of all charged particles could be captured by the detector. The geometrical information of the molecule is perceptible in a diffraction pattern.

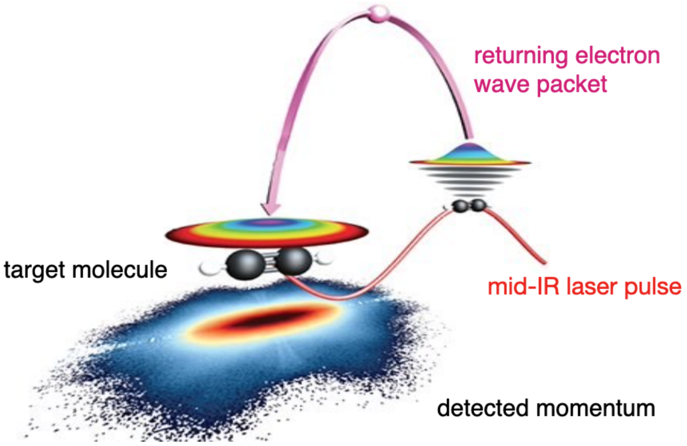

Figure 2.7: **Illustration of LIED technique to image the molecule**. The ground-state electrons first undergo tunnelling ionization through the barrier formed by the laser and the Coulomb field. The ionized electron is then accelerated and returned to the vicinity of the parent ion (mauve trace) driven by the laser field. Elastically rescattering to parent ion and captured by the momentum detector. The picture is original from [95].

2.4.1 Momentum transfer

The returning EWP needs to achieve adequate energy to penetrate the core of the parent's ion to overcome the influence of the column potential. Meanwhile, as shown in Fig. 2.8, high energy electrons own a shorter De Broglie wavelength offers better spatial resolution and more extensive momentum transfer range. The momentum transfer defines as:

$$q = \mathbf{k}_\mathrm{resc}(k, \theta, \phi) - \mathbf{k}_0(k_0, 0, 0), \tag{2.77}$$

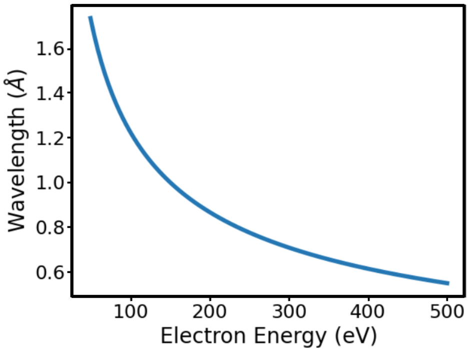

Figure 2.8: **De Broglie wavelength of electron.** The relationship between De Broglie wavelength and electron energy. The ultra-short electron beam driven by the long-wavelength laser will have higher energy, and its corresponding shorter De Broglie wavelength will provide higher spatial resolution for the LIED method, which will directly promote the molecular ultrafast dynamic imaging.

which arises from the momentum difference between the scattered electrons vector $\mathbf{k}_{\mathrm{resc}}(k,\theta,\phi)$ and the returning (incoming) electrons vector $\mathbf{k}_0(k,\theta,\phi)$. If we assume the azimuthal angle is symmetry in the scattering process, the magnitude of the momentum transfer could be expressed as:

$$q = 2k_0 \cdot \sin(\theta/2) \tag{2.78}$$

2.4.2 Quantitative re-scattering (QRS) theory

The physics understanding of LIED could be described through the QRS model [96, 97]. The QRS theory describes the high-energy photoelectrons distribution produced by intense laser pulses. The momentum distribution results from electron differential cross sections (DCS) among the returning free-electron wave packet elastic scattering with the target ion. The photoelectron momentum distributions $D(k,\theta)$ are shown as:

$$D(k,\theta) = W(k_{\mathrm{r}})\sigma(k_{\mathrm{r}},\theta_{\mathrm{r}}) \tag{2.79}$$

$D(k,\theta)$ depend on $W(k_{\mathrm{r}})$ is interpreted as the momentum distribution of the returning electrons also called returning wave packet (RWP), and the field-free elastic DCS, $\sigma(k_{\mathrm{r}},\theta_{\mathrm{r}})$. The variable of the detected momentum k, detected scattering angle θ, the returning momentum k_{r} and rescattering angle θ_{r} are illustrated in Fig. 2.9. Since the electron rescattering process occurs during the laser field, the scattered electron gains an additional vector momentum "kick" $-A(t_{\mathrm{r}}) = -A_{\mathrm{r}}$ from the electric field, where time t_{r} is the instant of electron recollision. Hence, the relationship between detected momentum and returning momentum is given by:

$$k_{\parallel} = k\cos\theta = -A_{\mathrm{r}} \pm k_{\mathrm{r}}\cos\theta_{\mathrm{r}} \tag{2.80}$$

$$k_{\perp} = k\sin\theta = k_{\mathrm{r}}\sin\theta_{\mathrm{r}}, \tag{2.81}$$

where the plus (minus) sign refers to the electrons returning to the target ion along the positive (negative) electric field. $\|$ sign indicates parallel to the polarization, and $\perp$ is perpendicular to polarization, respectively. Meanwhile, we assume the long trajectory is dominated over short trajectories due to the significant higher ionization probability, hence, the long trajectory is only considered for the thesis. According to the semi-classical re-collision model, we could get the relationship between A_r and k_r as $A_\mathrm{r} = k_\mathrm{r}/1.26$, the ratio is a constant value for long trajectory [97].

For calculation of molecular ionization, angular distributed ionization rate $\mathrm{N}(\Omega_L)$ and alignment distribution $\rho(\Omega_L)$ of a molecule need to be included, where Ω_L is the alignment angle based on the laboratory frame. The angle between molecular orientation and laser polarization is one of the essential parameters to influence ionization rate. When the laser polarization is parallel to the molecular orbital, such as the highest occupied molecular orbital (HOMO), the ionization possibility is more dominant than the perpendicular case.

The observed photoelectron momentum spectrum is supplied by the incoherent sum of all orientated angles as:

$$D(k, \theta, \Omega_L) \propto W(k_\mathrm{r}) \int d\Omega_L [\rho(\Omega_L) N(\Omega_L) \sigma(k_\mathrm{r}, \theta_\mathrm{r}, \Omega_L)] \tag{2.82}$$

In the LIED experiment, a weighted DCS (σ_tot) is a vital character we could directly measure from the experiment, which corresponds to the probability of being scattered into a particular unit solid angle. The σ_tot, in theory, could express as the ratio between the photoelectron momentum distribution and RWP:

$$\sigma_\mathrm{tot} = \int d\Omega_L [\rho(\Omega_L) N(\Omega_L) \sigma(k_\mathrm{r}, \theta_\mathrm{r}, \Omega_L)] \propto \frac{D(k, \theta)}{W(k_\mathrm{r})} \tag{2.83}$$

In other words, σ_tot can be determined in LIED experimental setup with an overall scaling factor, which is a bridge connected with theory and experiment.

2.4.3 Independent atom model (IAM)

The Independent atom model (IAM) model is based on charge density modelling. It assumes the electron distribution isotopically around the atom. Thus the charge density is only dependent on the internuclear distance of the molecule. Due to it is a straightforward method, it is always used in diffraction techniques like UED and XRD. This section introduces the IAM to calculate molecular DCS compared with the LIED experiment's measurement.

Calculated the field-free DCS, assuming the incident beam of the electron as planar wave scatter with a multi-centre atomic system could be expressed as:

$$\sigma(k_\mathrm{r}, \theta_\mathrm{r}, \Omega_L) = \sum_{i,j} f_i(k_\mathrm{r}, \theta_\mathrm{r}) f_j^*(k_\mathrm{r}, \theta_\mathrm{r}) e^{i\mathbf{q}\mathbf{R}_\mathrm{i,j}} \tag{2.84}$$

Where Ω_L is the alignment angle concerning the laboratory frame, the $f_i(k_\mathrm{r}, \theta_\mathrm{r})$ is the real part of the scattering amplitude for the i_th atom, the $f_j^*(k_\mathrm{r}, \theta_\mathrm{r})$ is the imagery part of the j_th atom. $\mathbf{R}_\mathrm{i,j} = \mathbf{R}_i - \mathbf{R}_j$ is vectorial internuclear distance and $\mathbf{q} = \mathbf{k}_\mathrm{resc} - \mathbf{k}_r$ is the

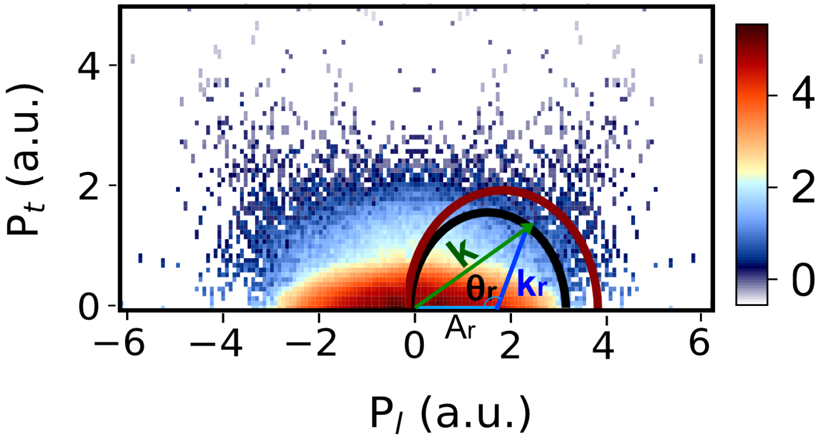

Figure 2.9: **PtPl map**. The measured 2D electron momentum distributions in logarithmic scale with P_l (parallel laser polarization) and P_t (perpendicular laser polarization). The returning electron momentum k_r, detected finial momentum k, laser vector potential A_r and rescattering angle θ_r are shown, the black and red circle show the different returning momentum.

momentum transfer vector between the returning and rescattering electron. The general equation of DCS could be express as:

$$\sigma_{\mathrm{tot}}(k_\mathrm{r},\theta_\mathrm{r}) = \sum_{i=j}|f_i|^2\int d\Omega_L|\rho(\Omega_L)N(\Omega_L)| + \sum_{i\neq j} f_i f_j^*\int d\Omega_L|[\rho(\Omega_L)N(\Omega_L)e^{i\mathbf{qR}_{\mathrm{i,j}}}] \tag{2.85}$$

For the random rotated molecular target, we integrate over alignment angle Ω_L and get:

$$\begin{aligned}\sigma_{\mathrm{tot}}(k_\mathrm{r},\theta_\mathrm{r}\theta_\mathrm{r}) &= \sum_i|f_i|^2 + \sum_{i\neq j} f_i f_j^*\int e^{i\mathbf{qR}_{\mathrm{i,j}}} \\ &= \sigma_{\mathrm{atom}} + \sigma_{\mathrm{mol}}\end{aligned} \tag{2.86}$$

The σ_{tot} is comprised of two components: (i) the incoherent sum of atomic scatterings, σ_{atom}, and (ii) a modulating coherent molecular scattering signal, σ_{mol}, which is around one order lower. The atomic term σ_{atom} contributes as a background signal to our total scattering signal, and relates to the number and types of atoms and is independent of the molecular structure. The σ_{mol} expresses the coherent molecular interference term which includes the molecular internuclear distance of two atoms, containing the fingerprint of geometrical information of the molecule.

To delicate compare with theory and experiment, we define a more sensitive factor called molecular contrast factor (MCF), which is the ratio between coherent molecular interference term and incoherent atomic term, exhibits a more clear interference signal due to without the σ_{atom} background contribution.

$$MCF(k_\mathrm{r},\theta_\mathrm{r}) = \frac{\sigma_{\mathrm{mol}}}{\sigma_{\mathrm{atom}}} = \frac{\sigma_{\mathrm{tot}}-\sigma_{\mathrm{atom}}}{\sigma_{\mathrm{atom}}} = \frac{1}{\sigma_{\mathrm{atom}}}\sum_{i\neq j} f_i f_j^*\frac{\sin(q,R_{\mathrm{i,j}})}{q,R_{\mathrm{i,j}}} \tag{2.87}$$

To extract the molecular structure via the LIED method, we usually fit the experimental MCF and theoretical MCF. The fitting of an MCF is more sensitive than fitting a DCS because the offset σ_{atom} is removed, where the oscillated signal is more pronounced. Where the experimental MCF is given by:

$$MCF_{\text{exp}}(k_{\text{r}}, \theta_{\text{r}}) = \frac{\sigma_{\text{exp,tot}} - \sigma_{\text{atom}}}{\sigma_{\text{atom}}} = \frac{\beta\sigma_{\text{exp}} - \sigma_{\text{atom}}}{\sigma_{\text{atom}}} \tag{2.88}$$

The β factor is a scaling factor that comes from the different order of magnitude between experimental and simulated results, which is given by the best fit between an experimental MCF and a theoretical MCF. The QRS method used the fitting routine to retrieve molecular structure by seeking the minimum discrepancy between an experimental MCF and theoretical MCFs spanning around possible structures. Primely, we calculated theoretical MCFs for each configuration by varying internuclear distances. Next, the best chi-square fit of the experimental to the theoretical MCF is determined via:

$$\chi^2(\mathbf{R}) = \sum_{i,j}(MCF_{\text{exp}}(k_{\text{r,i}}, \theta_{\text{r,j}}) - MCF(k_{\text{r,i}}, \theta_{\text{r,j}}, \mathbf{R})) \tag{2.89}$$

i, j addresses the available experimental indices of grid points for returning energies and rescattering angles, respectively. **R** is the internuclear distance. The minimum position χ^2_{min} will be found to identify the measured molecular structure.

On the other hand, LIED is based on the IAM model and QRS theory. IAM does not describe well that DCS returns energy below 50 eV [96, 97]. In the experiment, we must establish a return energy higher than 50 eV in order to be correctly explained by the theory.

2.4.4 Spatial resolution

Spatial resolution refers to the size of the smallest unit that can be distinguished in detail on diffraction patterns and is an index used to characterize the capability to recognize the minimum internuclear distance. The spatial resolution is an essential parameter when we design an experiment. Let us briefly talk about it in the LIED configuration but also useful for general diffraction imaging. The spatial resolution of diffraction imaging mainly depends on the probe beam wavelength and scattering angle. Traditionally imaging techniques like the X-ray crystallography, the smallest distance could be distinguished related on Bragg's law [98, 99] as the equation:

$$n\lambda = 2d\sin(\alpha), \tag{2.90}$$

where d is the smallest distance between crystal lattice planes, α is the angle between the incident beam and crystal plane, n is an integer, and λ is the beam's wavelength. Choosing the minimum integer number as $n = 1$, the spatial resolution depends on:

$$d = \frac{\lambda}{2\sin(\alpha)}. \tag{2.91}$$

On the other hand, applying the Fourier transform to the MCF varied with q (MCF(q); Eq. 2.87), we could extract the molecular internuclear distance, which is called Fourier transform variant of LIED method. According to the character of the Fourier transform, the resolution of the output internuclear distance $\mathbf{R}_{\mathrm{i,j}}$ depends on the range of input momentum transfer q. The Fourier transform transmits from the momentum transfer domain to the space domain, involving the resolution of the output internuclear distance defined by:

$$D = \frac{2\pi}{\Delta q}. \tag{2.92}$$

The D is the minimum distance that could be distinguished. If the momentum transfer range is too small, we could not identify the two peaks in the space. It seems the Fourier transform resolution and Bragg's law are two independent conditions to restrict the spatial resolution. We will convert them to a same formula in the following text. The wavenumber k_0 is given by:

$$k_0 = \frac{2\pi}{\lambda} \tag{2.93}$$

Taking into count Eq. 2.78, q could rearrange as function with λ,

$$q = 2k_0 \cdot \sin(\theta/2) = \frac{4\pi \sin(\theta/2)}{\lambda}, \tag{2.94}$$

substituting it to equation 2.92 and we will get

$$D = \frac{2\pi}{q} = \frac{2\pi}{\frac{4\pi \sin(\theta/2)}{\lambda}} = \frac{\lambda}{2\sin(\theta/2)} \tag{2.95}$$

Which is actually the same as the outcome as we calculated from Eq. 2.91 considering D and d are identical. The θ is defined as the angle between the incident beam and scattering beam, the half of θ is equal to the α according to the geometric relationship. Thus, we have approved that the spatial resolution limitation from Bragg's law and Fourier transform are identical. Nevertheless, we also need to notice that the momentum transfer range typical is not starting from zero in LIED compared with X-ray or electron diffraction, because we need to avoid the direct electrons which dominate the small value of the momentum transfer area.

Chapter 3

Experimental Methodology

Contents

3.1 Laser technology

Since the 1960s, laser as a coherence monochromaticity light source with high collimation carries tremendous physics developments [3]. After 60 years of development, laser technology continuously innovated biology, chemistry, materials, medicine, and other natural science fields, forming a series of new interdisciplinary and application fields. Such as optoelectronics technology, nonlinear optics, spectroscopy, ultrafast photonics, quantum optics, strong-field physics, lidar, cold atom and cold molecular physics, laser chemistry, laser medicine, photonic biology, laser-controlled nuclear fusion and laser processing [5]. Among them, the investigation on the interaction between ultra-short and intense lasers with the matter has become one of the most active and cutting-edge scientific research fields in the world.

Before discussing the interaction between laser and matter, we will briefly review the development of laser technology. With the continuous innovation of technology, the peak power of laser output has reached the order of titanium watts (10^{12} W) or even petawatts (10^{15} W), and the intensity of the focused laser beam has progressed from the initial less than 10^{10} W/cm^2 reach to $10^{25} \sim 10^{29}$ W/cm^2 [13, 32, 100, 101]. Figure 3.3 shows the maximum laser peak intensity that can be achieved in laboratories with different years and the corresponding research fields. It can be seen that people's understanding of the microscopic world from the atomic level to the Quark era with the help of the development of laser technology.

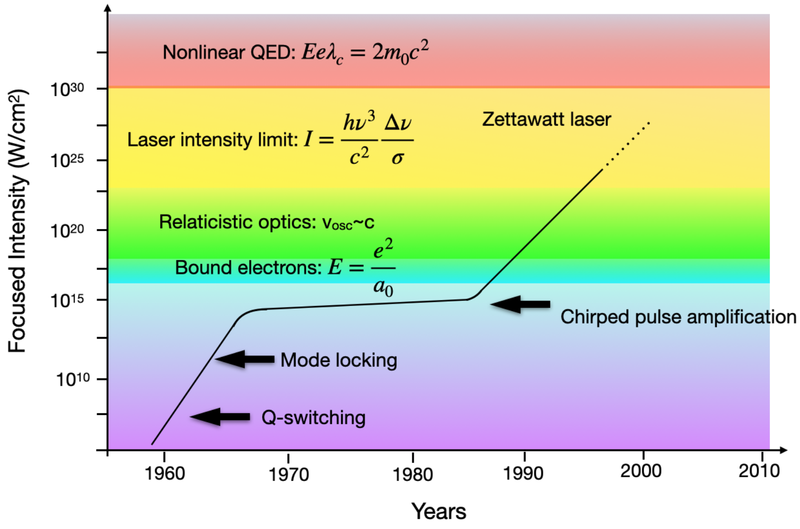

Figure 3.1: **Laser intensity vs. years.** The maximum laser peak intensity that can be achieved in laboratories with different years and the corresponding research fields [100].

On the other hand, after the laser developed from continuous light to pulsed light, its pulse width progressively narrowed from nanoseconds (ns, 10^{-9}s) to femtoseconds (fs, 10^{-15}s), and then further shortened to attoseconds (as, 10^{-18}s) shown in Fig. 3.2 [78]. It offers people's perception of the time scale to the attosecond level.

3.1.1 Q-switching

If the population of atoms (or molecules) is reversed according to the thermal equilibrium (Boltzmann) distribution of energy levels, it is possible to use stimulated emission to achieve optical amplification. Schawlow and Townes [102] have discovered the phenomenon of strong light in the experiment, pointing out that when a substance is excited by energy

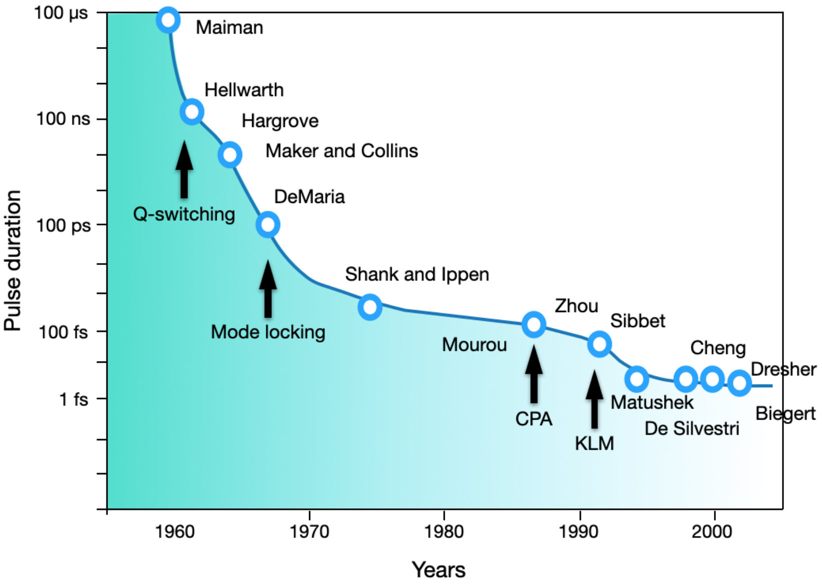

Figure 3.2: **Laser pulse duration vs. years.** The laser pulse duration that can be achieved in laboratories with different years [78].

with the same frequency as intrinsic molecular oscillation, it will produce a not diverge intense light - laser (light amplification by stimulated emission of radiation). After that, scientists proposed different experimental schemes, and Maiman finally made the world's first laser in 1960 [3]. Two years later, Hellwarth and McClung realized the Q-switching technology for the first time in a ruby laser [4]. The Q value is given by:

$$Q = 2\pi v_0(\text{The energy stored in the cavity/ The energy lost per second}) \tag{3.1}$$

Where v_0 is the centre frequency of the laser, the Q value is inversely proportional to the loss in the cavity. If the loss is significant and the threshold is high, it is not easy to start vibration; on the contrary, if the loss is slight and the threshold is low, it is easier to start vibration. Since the laser threshold limits the maximum number of population inversions on the energy level, the threshold can be changed effectively by changing the Q value of the resonant cavity. The basic idea of Q-switching technology is to use an electro-optical switch or acoustic-optic switch to control laser oscillation and output. At the beginning of pumping, make the cavity in a low Q state, that is, raise the threshold to prevent forming oscillations, and the number of particles at the upper energy level can be massively accumulated. When the accumulation reaches the maximum value (saturation value), then suddenly reduces the loss of the cavity, the causing Q value immediately rises, and the laser oscillation is instantly established. Most of the particles stored in the upper energy level are converted into the output in the form of a single pulse with high peak power. Compared with a free-running laser, the appearance of Q-switching technology has increased the laser peak power by three orders of magnitude, achieving a 10^6 W level output. Meanwhile, the laser pulse width is also shortened to the order of nanoseconds.

3.1.2 Mode-locking

After the appearance of the laser, based on the first published paper describing the theory of longitudinal modes in the laser cavity, people realized mode locking on the He-Ne laser and generated nanosecond laser pulses [103]. For general lasers, if there is no special mode selection, the output will always contain multi-longitudinal modes, which are not in phase with each other. Therefore, the output pulse results from their irregular superposition and the intensity fluctuate with time. The mode-locking technique achieved phase locking between different oscillating longitudinal modes. The modes are coherently superimposed, a sequence optical pulse with a specific time interval and extremely narrow pulse width and remarkably high peak power can be obtained. The development of mode-locking technology has passed through active mode-locking, passive mode-locking, synchronous pump mode-locking, collision mode-locking, the solid-state pulse mode-locking, and self-mode-locking that appeared in the 1980s. Increased the laser pulse duration from nanoseconds to picoseconds [104] even femtoseconds [105].

Meanwhile, in the late 1980s, the appearance of Ti:Sapphire crystals significantly promoted the research and development of solid-state mode-locked lasers, securing the mode-locking technology more developed and stable [106, 107, 108, 109]. It is worth mentioning that based on the self-mode-locking technology, it is not necessary to insert any modulation element in the laser cavity and only use the nonlinear effect of the medium itself to achieve mode-lock. In 1991, Spence et al. [106] used a 20 nm long Ti:Sapphire crystal as the gain medium and inserted an SF14 glass prism pair into the cavity to compensate for dispersion, received a 60 fs self-mode-locked laser pulse output only using the Ti:Sapphire's own Kerr lens effect (KLM). The excellent stability of self-mode-locked lasers laid a solid foundation for the subsequent development of pulse amplification technology, commencing the ultra-short and intense lasers unquestionably possible to be practical. At present, commercial laser oscillators can directly generate ultra-short laser pulses with a pulse duration of 5 fs [110].

3.1.3 Chirped pulse amplification technology

When the laser pulse power increases to a specific level, the self-focusing, self-phase modulation and other nonlinear optical effects will damage the amplifying medium itself, which will reduce the quality of the laser and damage the optical components. The laser intensity has been unable to break through the bottleneck of $10^{15}\mathrm{W/cm^2}$ for the next 20 years (see the Fig. 3.3), until the emergence of chirped pulse amplification (CPA) technology got a breakthrough [111].

CPA technology is an essential milestone in the development of ultrashort pulse technology. The basic process is to use dispersive elements (such as gratings or prisms) to make the frequency components of the femtosecond pulse not synchronized in time, thereby stretching the femtosecond ultrashort pulse into Chirped pulses of the order of hundreds of picoseconds or even nanoseconds and then the expanded pulses are injected into the amplification system and amplified step by step. During the amplification process, the laser intensity remains at a low level even if the power increases rapidly due to the wide pulse duration, avoiding damage to optical components such as crystals. In the end, the

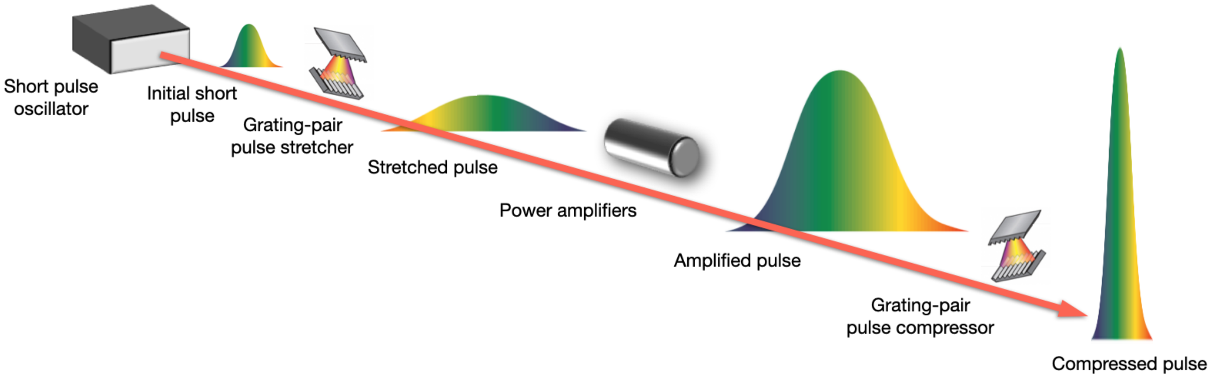

Figure 3.3: **Scheme of chirped pulse amplification.** Temporally stretching the femtosecond ultrashort pulse into Chirped pulses with dispersive elements, then amplified, and finally compressed again [110].

amplified pulse passes through the optical element with the opposite dispersion of the stretching unit, compressed the pulse in the time domain to obtain an ultra-high-power and ultra-short pulse output. At present, the developed and stable commercialized high-energy fs-laser systems generally use oscillators with Ti:Sapphire as the gain medium and chirped pulse amplification systems providing powerful research tools for the investigation of strong-field physics, electron acceleration, high-order harmonics, fast ignition, attosecond science and high-energy particle physics. [5].

On the other hand, the hollow-core fibre compression and filament compression techniques [110] overcome the gain narrowing effect and the bandwidth limitation of optical components, obtaining the few-cycle pulse output shorten to 2.6 fs [112]. Based on the compression method of hollow fibre with gas density gradient [113, 114], Bohman et al. added a specific positive chirp to the incident beam in advance to achieve a 5fs single pulse with 5mJ pulse energy [115]. The development of ultrashort pulses led to the vigorous development of corresponding physical research, making it possible to observe microscopic ultrafast phenomena such as electron motion [110].

3.1.4 Optical parametric amplification technology

In the early stages of laser development, the phenomenon of optical parametric amplification (OPA) has been perceived [116], the physical process is a three-wave mixing process, which a set of coupling equations can describe, including the phase and group velocities of the different wavelength components and wave vector detuning [117, 118] in the nonlinear crystal. The ultra-short and intense mid-infrared laser pulses generated in practical applications are dependent on difference frequency generation (DFG) and Optical parametric amplification (OPA).

A typical application of DFG is to use 800 nm Ti:Sapphire fs laser as the pump light and 1.053 µm YLF laser as the idle light to generate a single wavelength of 3.6 µm signal light in the nonlinear KTA crystal (Potassium Titanyl Arsenate, KTiOAsO4), to achieve the energy exchange between the three and amplify the idle light and signal light [74].

The OPA has exceptionally high flexibility and can generate ultra-short and intense pulses with tunable and an extensive range wavelength in a single system. Although different design schemes of optical energy amplification have been reported [118], the BBO crystal (β - Barium Borate) is commonly utilized in commercial OPA systems. First, a weak femtosecond light with a wavelength of 800 nm or its dual-frequency (400 nm) is used in the fused quartz (the threshold is commonly 1 µJ) to produce the seed light. In the second stage, strong 800 nm or 400 nm light as the pump light interacts with the seed light in the BBO crystal to generate and amplify signal light and idle light. Generally, it will be amplified by one or more stages to obtain higher energy signal light or idle light output. In order to achieve OPA, energy exchange must be realized between the three waves firstly, so the energy conservation formula must be satisfied:

$$\hbar\omega_{\mathrm{p}} = \hbar\omega_{\mathrm{s}} + \hbar\omega_{\mathrm{i}} \tag{3.2}$$

And the phases must be matched (momentum conservation):

$$k_{\mathrm{p}} = k_{\mathrm{s}} + k_{\mathrm{i}} \tag{3.3}$$

Where ω is the angular frequency and k is the light wave vector, respectively. When the phase matching is satisfied, the two light beams form a different angle α within the BBO, generating signal light with different wavelengths and polarization directions shown in Fig. 3.4. In practical applications, multi-stage OPA amplification and different design schemes could achieve higher power laser with wavelengths from ultra-ultraviolet to mid-infrared or even far-infrared (0.25-10 µm) [118].

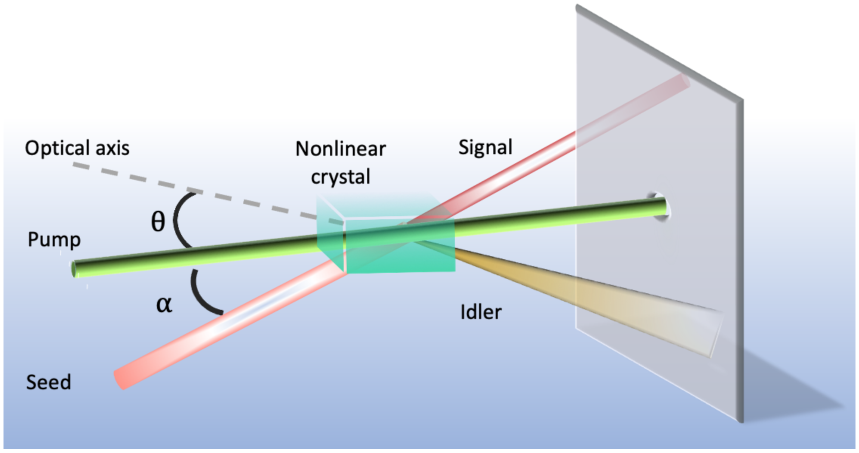

Figure 3.4: **Scheme of optical parametric amplification.** The pump and seed light beams form a different angle α within the nonlinear crystal, generating signal light with different wavelengths and polarization directions [119].

The rapid development of OPA combined with CPA provides a novel Optical parametric chirped pulse amplification (OPCPA) technology approach for achieving higher power femtosecond laser pulse. This technology was first proposed in 1992 [120] and achieve more prominent improvement in 1997 [121]. OPCPA technology provides full performance to the respective advantages of CPA and OPA. Compared with the traditional CPA system, it does not require a complicated multi-pass geometric optical path. Meanwhile, optimized phase matching of OPCPA expanded the gain bandwidth, eliminated the gain narrowing effect in CPA and reduced the internal absorption. The diminished thermal effect of the crystal and reduced corresponding energy loss of the OPCPA provides the chance to generate higher energy and higher quality beam. The existing OPCPA technology could reach the petawatt-level output by compressing the pulse width, which is a very potential new technological approach for the development of intense ultrashort lasers [119].

OPA and OPCPA technology development provide people high power and wavelength tuning laser beams, especially for the interaction between laser and matter in the mid-to-far infrared band, offering an unprecedented opportunity for the reach of strong-field physics such as above-threshold ionization, high-order harmonics, attosecond physics.

3.1.5 Mid-IR OPCPA source at 160 kHz repetition rate

Our advanced home built mid-infrared light source system, CEP stable OPCPA, operates at a 160 kHz high repetition rate of 3.2 µm. The table-top system can generate up to 118 µJ (18.9W) 97 fs. Figure 3.5 shows the schema of the High power 3.2 µm OPCPA laser system. The front-end two-colour Erbium-doped fibre laser runs at 100 MHz from Toptica Photonics AG, which delivers 220 mW at 1550 nm and a 1050 nm few milliwatts with sub-100 fs pulse durations.

The front-end generated two-colour laser beam converted to mid-infrared 3.2 µm beam via DFG process with periodically poled lithium niobate (PPLN) crystal. The 3.2 µm pulse is stretched to a 3 ps negatively chirped-pulse by propagating through a 50-mm-long sapphire rod, firstly pre-amplified in three consecutive OPCPA PPLN stages (OPCPA1, OPCPA2, OPCPA3) up to 2.6 µJ. Swapped the direction of the chirp from negative to positive by a chirp-inverter and further stretched up to 7 ps. The OPCPA Booster amplifier with PPLN crystal (OPCPA4, OPCPA5) amplified the 3.2 µm pulse to 18 µJ. The longer seed pulse improves the temporal overlap between seed and pump laser, increasing conversion efficiency from 2.8% to 7.2% when pulse duration stretches from 3 ps to 7 ps. The pulse energy reaches the 131 µJ (21W) after passing the finial OPCPA Booster amplifier stages with Potassium niobate (KNbO3) nonlinear crystals (OPCPA6, OPCPA7). The pulse finial compressed to 97 fs with compressed powers of 118 µJ (18.9 W) with the high transmission efficient anti-resonant (AR) coated 100 mm sapphire rod.

The Nd: YVO4 pump laser runs at 50 MHz delivering 1064 nm pulses, which repetition rate is reduced to 160 kHz and power up to 40W after the oscillator. The output beam is split into three beams (15W, 12.5W and 12.5W) to pump the OPCPA pre-amplifier PPLN, the OPCPA booster amplifier PPLN and the OPCPA booster amplifier bulk KNbO3, respectively. The first beamline with 15 W pump pulses is directly applied to amplify the pre-amplifier OPCPA stage. The second beamline (12.5W) is further amplified to 50 W by a single Nd: YVO4 power amplifier that is worked to amplify the first two OPCPA stages after the chirp-inverter. The third beamline is boosted up to 110 W by a chain of consecutive Nd: YVO4 power amplifiers to pump the bulk non-collinear OPCPA stages based on the KNbO3 crystals. Thus the total pump power attains 175 W (1.1 mJ).

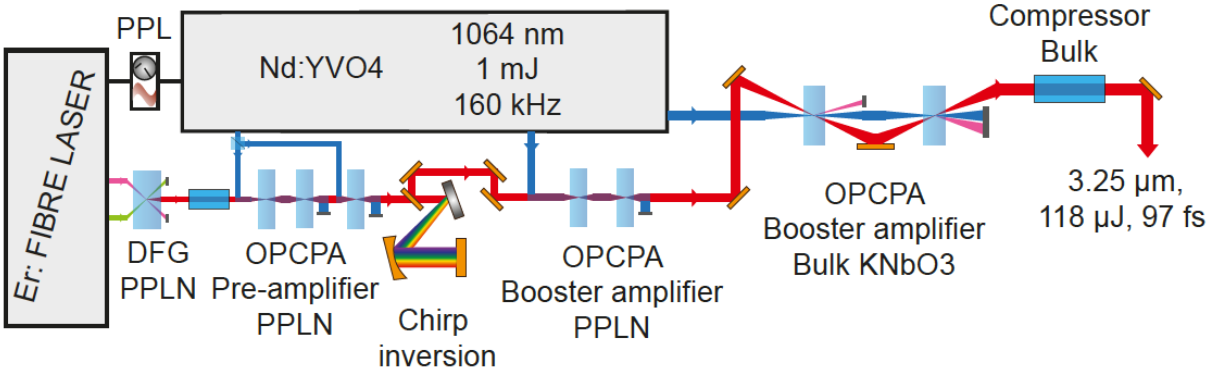

Figure 3.5: **Schema of the High power mid-IR OPCPA laser system.** The front-end two-colour Erbium-doped fibre laser runs at 100 MHz from Toptica Photonics AG, which delivers 220 mW at 1550 nm and a 1050 nm few-milliWatts with sub-100 fs pulse durations. The Nd: YVO4 pump laser runs at 50 MHz delivering 1064 nm pulses, which repetition rate is reduced to 160 kHz and power up to 40W after the oscillator. The output beam is split into three beams with 15W, 12.5W and 12.5W to pump the OPCPA pre-amplifier PPLN, the OPCPA booster amplifier PPLN and the OPCPA booster amplifier bulk KNbO3, respectively.

3.1.6 Intensity estimation

The field strength of the incident light directly influences the light-matter interactions. Thus, the exact information about the laser intensity of the focused spot used in an experiment is crucial to scale and interpret experimental results. Assuming that the laser beam irradiance distribution conforms to the ideal Gaussian distribution, which is symmetric about the centre of the beam. It decreases as the distance between the centre of the beam and the direction of propagation increases, laser intensity distribution in the focal volume can be expressed as:

$$I(z,r) = I_{\text{peak}}[\frac{\omega_0^2}{\omega^2(z)}]\exp[-\frac{2r^2}{\omega^2(z)}] \tag{3.4}$$

Where $\omega(z)$ is the radius of the laser beam and ω_0 is the intensity drops to $1/e^2$ of the axial, the laser intensity as a function of distance z parallel to the laser propagation direction and distance r perpendicular to the laser propagation direction from the focus point. The peak laser intensity could be calculated as:

$$I_{\text{peak}} = \frac{2E_{\text{p}}}{\pi\tau\omega_0^2} = \frac{2P}{f_{\text{rep}}\pi\tau\omega_0^2} \tag{3.5}$$

The pulse energy $E_{\text{p}} = \frac{P}{f_{\text{rep}}}$ calculated from laser power P divided the repetition rate (f_{rep}), where the P directly measured with a power meter in the experiment, τ present the pulse duration in Full width at half maximum (FWHM). In the current experimental set-up, we use an on-axis parabolic mirror with focal length d_f=50 mm to focus the beam with a waist of ω_0=7-10 µm.

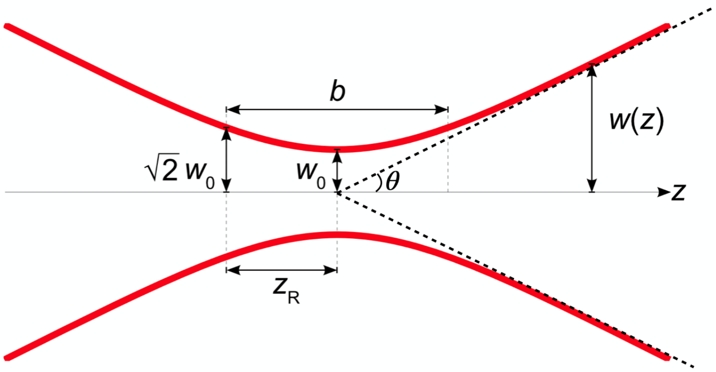

Figure 3.6: **Gaussian beam Waist.** When the focused beam propagates in space, its irradiance profile does not remain constant ($\omega(z)$depends on z). Due to diffraction, the Gaussian beam will converge and diverge from the beam waist (ω_0) area, where the beam diameter reaches its minimum. Rayleigh length z_R and divergence angle θ are also shown.

When the beam is focused in space, its irradiance profile does not remain constant ($\omega(z)$ depends on z). Due to diffraction, the Gaussian beam will converge and diverge from the beam waist (ω_0) area, where the beam diameter reaches its minimum. The convergence and divergence of the beam are within the range of the divergence angle θ at both ends of the beam waist (Fig. 3.6).

$$\begin{gathered} \omega(z) = \omega_0\sqrt{1 + (\frac{z}{z_R})^2} \\ \theta = \frac{\lambda}{\pi\omega_0} \end{gathered} \tag{3.6}$$

z_R is the Rayleigh length or Rayleigh range refers to the distance of the beam along its propagation direction from its waist to a cross-section, where the cross-sectional radius is about $\sqrt{2}$ times the waist radius (laser intensity drop to $I_{\text{peak}}/2$). θ is based on the far-field approximation, which cannot accurately reflect the divergence near the beam waist, becoming more accurate as farther from the waist. The formula above shows that the divergence angle is inverse proportional to the beam waist, such as the more extensive the beam waist, the smaller the divergence angle. So a laser beam expander is always used to reduce the beam divergence by increasing the beam diameter. The ω_0 and z_R could also express with optical and laser information:

$$\begin{gathered} \omega_0 = \omega(0) = \frac{\lambda d_f}{\pi R} \\ z_R = \frac{\omega_0^2\pi}{\lambda} \end{gathered} \tag{3.7}$$

Where d_f is the focal length of the mirror or lens and R is the radius of the incident collimated beam. We could see that the ω_0 is proportional to wavelength, leading to a shorter wavelength that is easier to focus. Figure 3.7(a) show the laser beam shape as transverse distance r. People typically define the beam boundary (beam diameter) at a minimum intensity of $I_{1/\mathrm{e}^2} = I(z_{1/\mathrm{e}^2}, 0) = 1/e^2 \cdot I_{\mathrm{peak}}$, where the transverse distance is equal to ω_0. Figure 3.7(b) provides the 2D intensity contour plot I(r, z) in the focus spot. It spans a longitudinal volume with a width around $z_{1/\mathrm{e}^2} \approx 127$ μm and the radius of ω_0, considering a minimum intensity of I_{1/e^2}. The green line is the outline of the focal volume, while the $\omega(z)$ is shown as a red line.

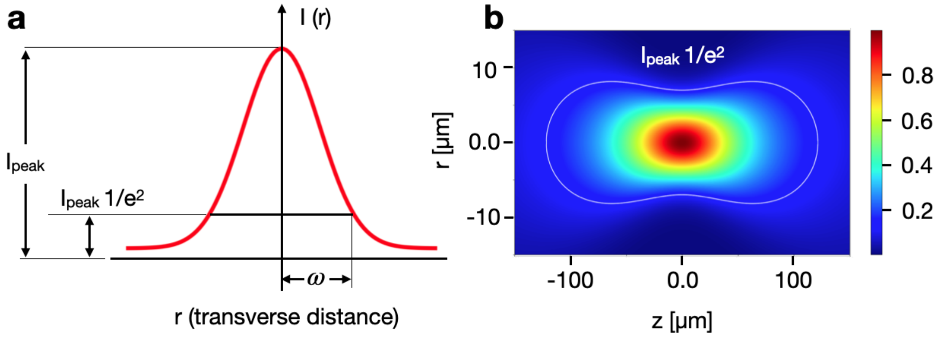

Figure 3.7: **Intensity distribution in the focal volume.**(a) The laser beam shape as transverse distance r. The typically defined the beam boundary (beam diameter) at a minimum intensity of $I_{1/\mathrm{e}^2} = I(z_{1/\mathrm{e}^2}) = 1/e^2 \cdot I_{\mathrm{peak}}$, where the transverse distance is equal to ω_0. (b) The 2D intensity contour plot I(r, z) in the focus spot. The white line is the outline of a minimum intensity of I_{1/e^2} [122].

The equation above is assumed the perfect Gaussian distribution of the laser beam. In reality, it always suffers aberrations due to optics and laser propagation. It could be interpreted via the beam quality factor M^2 to compare the performance of real laser beams and diffraction-limited Gaussian beams. For a perfect Gaussian beam, the $M^2 = 1$. $M^2 \geq 1$ indicates the aberrations exist, presenting a multiplication factor to λ. Hence, aberrations cause a bigger focal volume and lower laser peak intensity if other parameters are equal. The M^2 factor is highly related to beam performance. However, the factor cannot describe the specific spatial distribution, characterizing the proximity of the beam to the perfect Gaussian beam, which mainly determines the minimum spot size and beams divergence angle.

Duo to the laser beam focus inside the ultrahigh vacuum chamber, we cannot directly access and diagnose the beam performance only depended on optical information, resulting in the bigger error of the laser intensity determination. Here, we present several alternative ways to assist the laser intensity estimation:

(1) Fitting longitudinal momentum with ADK theory. In theory, the ADK method could adequately describe the electron and ion longitudinal momentum distribution. The best-fitting between the theory and experiment will provide the laser peak intensity by comparing the theoretical electron or ion longitudinal momentum with various laser intensities with experimental data induced by a linearly polarized laser field.

(2) Comparing with $2U_\mathrm{p}$ and $10U_\mathrm{p}$ cut-off. In chapter 2, we talk about the maximum kinetic energy for a direct electron is $2U_\mathrm{p}$ and for the rescattering electron is $10U_\mathrm{p}$. The Fig. 4.3b shows electron counts as a function of returning energy. We could identify the laser peak intensity by identifying the $2U_\mathrm{p}$ and $10U_\mathrm{p}$ cut-off positions.

(3) Compare with H_2 peaks shape. (1) and (2) need to determine laser peak intensity by analyzing data firstly, which is not suitable for quick checks in the lab. The third method is by comparing the ToF peak shape of H_2. Figure 3.8 shows the normalized ion counts H_2 as a function of time of flight with different laser intensity, the internal two peaks around 1650 ns and 1800 ns from dissociation channel (H^++H) and the outer two peak around 1550 ns and 1900 ns from charge resonance enhanced ionization channel (H^++ H^+) in this case. We could determine laser peak intensity quickly by comparing the relative ratio between the dissociation channel and the enhanced ionization channel.

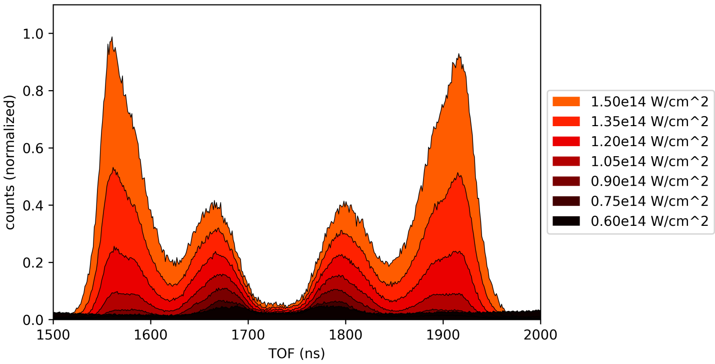

Figure 3.8: **Laser intensity calibration with H_2 ToF peak.** The normalized ion counts H_2 as a function of time of flight with different laser intensity, the internal two peaks around 1650ns and 1800 ns from dissociation channel (H^++ H) and the outer two peak around 1550 ns and 1900 ns from charge resonance enhanced ionization channel (H^++ H^+). We could determine laser peak intensity with higher precision by comparing the relative ratio between the dissociation channel and the enhanced ionization channel.

At last, we highlight that the laser system possesses a 160 kHz repetition rate. The experiment shows the ratio of electron rescattering possibility to directly ionized electrons estimates approximately as λ^{-4}. High repetition rate provides the LIED measurement could be accomplished in a realistic time scale. Meanwhile, to image the molecular structure, electrons need to gain more significant kinetic energy from the laser to penetrate the atomic core of the molecule. A mid-IR high repetition rate laser system guarantees the satisfactorily rescattering electron achieves adequate kinetic energy to establish the LIED experiment.

3.2 Reaction microscope

The interaction between light and matter happens inherently in three dimensions. Hence, it is crucial to capture all ionization events to apprehend the completeness of the physical process. The reaction microscope (ReMi) or Cold Target Recoil Ion Momentum Spectroscopy (COLTRIMS) is currently one of the best tools for studying the collision dynamics of atoms and molecules. The apparatus allows detecting 3D ion and electron momentum coincidently with 4π solid angle acceptance. Our ReMi setup includes a supersonic gas cold target system, a time-of-flight spectrometer (ToF), a delay line anode position-sensitive detector, a fast electronics system and a data acquisition system.

The photon collides perpendicularly with the ultrasonic gas beam at the collision centre, causing the target molecules to be ionized. An external static electric field is and magnetic field applied to the collision area. The recoil electrons and ions under the action of the external fields and finally fly to the position-sensitive detector. The initial longitudinal momentum (parallel to the external static field) can be determined by measuring the flight time and static electric field. The hitting position of the detector and static magnetic field determines the transverse momentum (perpendicular to the external field). Finally, the three-dimensional momentum of each particle can be accurately measured so that the reaction process can be reconstructed.

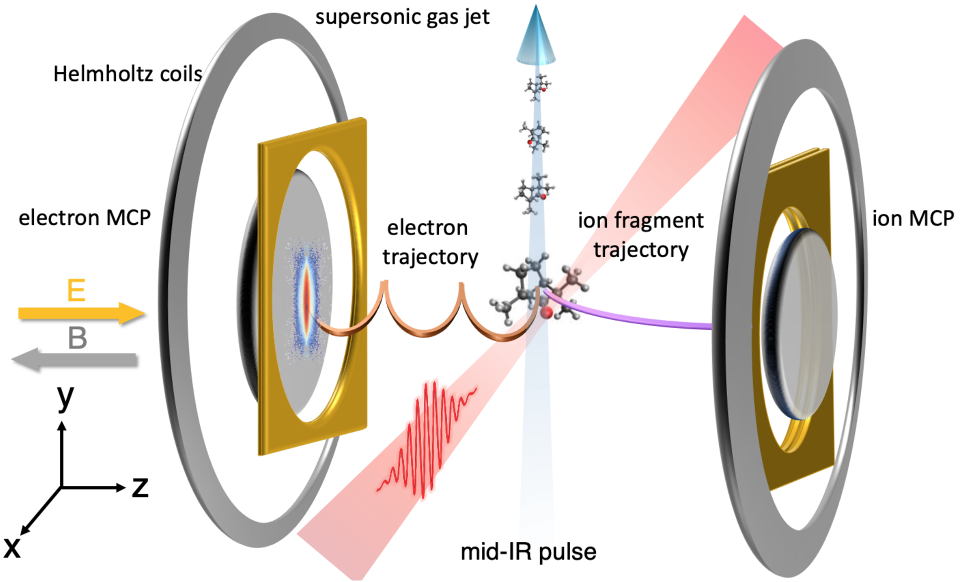

Figure 3.9: **Working principle of a reaction microscope setup.** The photon collides perpendicularly with the ultrasonic gas beam at the collision centre, causing the target molecules to be ionized. An external static electric field is and magnetic field applied to the collision area. The recoil electrons and ions under the action of the external fields and finally fly to the position-sensitive detector.

3.2.1 Supersonic gas jet

To investigate single molecule ultra-fast dynamic, we need to prepare the sample for the gas phase to achieve the single-molecule interaction. To achieve a high-resolution recollision picture, we must address minimum other uncertainties, such as reducing the initial momentum spread. The longitudinal momentum (laser propagation direction) spread of the gas jet could be described by the Maxwell-Boltzmann distribution of ideal gas as:

$$\Delta p = \sqrt{k_B T m}, \tag{3.8}$$

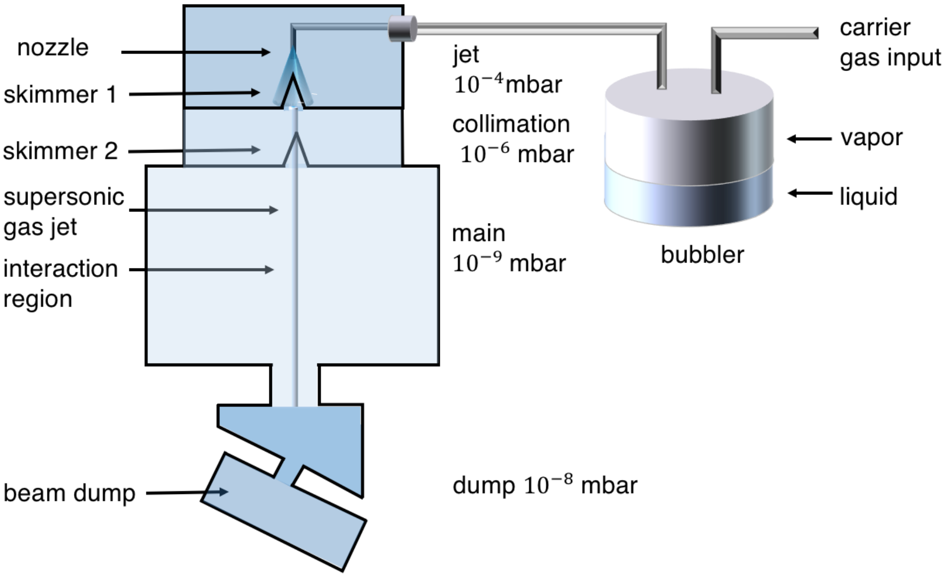

Figure 3.10: **Supersonic gas jet propagate in vacuum chamber.** The input gas pass the jet chamber (10^{-4} mbar), the collimation chamber (10^{-6} mbar), then arrive at the main chamber.The illustration of a ReMi connected with a simple bubbler.

where the k_B is Boltzmann constant and T is the internal temperature. For example, the Δp of noble gas atoms at room temperature $T_0 = 300$ K around 10 a.u.. It reaches the same order momentum distribution from the re-collision event of strong-field ionization. We need to cool down the internal target temperature to reduce the momentum spread. One way to achieve it is to accelerate the gas speed to transfer the internal energy of thermal motion to kinetic energy. We realize the adiabatic expansion to form a supersonic gas jet via passing gradient vacuum level chambers. The Fig. 3.10 shows the input gas first reaches the jet chamber (10^{-4} mbar), passing the skimmer 1 to enter the collimation chamber (10^{-6} mbar), then passing the skimmer 2 to arrive at the main chamber (10^{-9} mbar). The gradient of the pressure chamber accelerates the gas speedup to exceeding the speed of sound c_S and effectively decrease the gas jet internal temperature. A supersonic gas jet could be effectively cooled downrange from several mK to a few tens of K. The maximum momentum in the jet propagation direction could be expressed as:

$$\begin{aligned} \frac{1}{2}mv_{\mathrm{jet}}^2 &= \frac{f}{2}k_BT_0 + k_BT_0 \\ p_{\mathrm{jet}} = p_{\parallel} &= \sqrt{2k_BT_0m(1+\frac{f}{2})} \end{aligned} \tag{3.9}$$

The f is the degrees of freedom of an ideal gas particle. For example, the atoms possess f=3 translational degrees of freedom, and linear molecules possess f=5 degrees of freedom containing two rotational degrees.

In gas flow dynamics, the relationship of jet velocity v and the speed of sound c_S could be described as a Mach number as $M_\mathrm{a} = \frac{v}{c_S}$. The gas jet can be separated into individual areas depending on the magnitude of the M_a after expanding through the nozzle. The area is located after the nozzle with the lowest effective gas temperature and higher Mach number $M_\text{a} \gg 1$, known as the zone of silence. The zone of silence extends up to the boundary of the Mach disk ($M_\text{a} = 1$).

Table 3.1: Technical parameters of vacuum system

Gas bottle stagnation pressure (typ.)	1-3 bar
Pressure in Jet Chamber	10^{-4} mbar (Ar_{1bar})
Jet ch. turbo pump	510 l/s (for N^2)
Pressure in Collimation Chamber	10-6 mbar (Ar_{1bar})
Collimation ch. turbo pump	250 l/s (for N^2)
Pressure in Main Chamber	10^{-9}mbar (Ar_{1bar})
Main ch. turbo pump	510 l/s (for N^2)
Pressure in Dump Chamber	10^{-8} mbar (Ar_{1bar})
Dump ch. turbo pump	250 l/s (for N^2)
Nozzle diameter	30 µm
Skimmer 1 diameter	200 µm
distance nozzle - skimmer	1 $\approx$ 5 mm
Skimmer 2 diameter	400 µm
distance skimmer 1 - skimmer 2	$\approx$ 22 mm
distance skimmer 2 - focal plane	$\approx$ 65 mm
gas beam divergence θ	0.85^o
gas jet diameter at focal spot	$\approx$1.4 mm

To calculate the final temperature T_∞ in the jet, we first define the speed ratio as a ratio between the jet velocity and the residual thermal velocity :

$$S_{\infty,\parallel} = \frac{v_{\text{jet}}}{v_{\text{therm}}} = A[\sqrt{2}\frac{P_0 d}{k_B T_0}(\frac{53 C_6}{k_B T_0})^{1/3}], \tag{3.10}$$

With the initial pressure(P_0), initial temperature (T_0) and nozzle diameter(d) could be determined in the experiment, and three empirical parameters (A, B and C_6) depend on the target property. The final jet temperature is calculated as:

$$T_{\infty,\parallel} = T_0 \frac{\kappa}{\kappa - 1} \frac{1}{S^2_{\infty,\parallel}}, \tag{3.11}$$

with the heats ratio $\kappa = \frac{c_\text{p}}{c_V} = 1 + \frac{2}{f}$. The finial longitudinal momentum spread of the supersonic jet could be express as:

$$\Delta p_{\parallel,\infty} = \pm\sqrt{k_B T_{\infty,\parallel} m} \tag{3.12}$$

Alternatively, the final jet temperature could also be determined with experiment data when the laser polarisation toward the detector (perpendicular to the jet direction):

$$T_{\infty,\parallel} = \frac{\Delta p^2_{\perp,\text{ion}}}{4\ln(4) k_B m} \tag{3.13}$$

Where $\Delta p_{\perp,\mathrm{ion}}$ is the ion momentum distribution perpendicular to the laser polarisation. The transverse jet momentum spread $\Delta p_{\perp}$ depends on the last skimmers' orifice geometry, the divergence of the gas jet in the transverse direction could express as:

$$\begin{aligned} \Delta p_{\perp} &= \pm \tan(\Theta) p_{\parallel} \\ \Theta &= \arctan[d_{\mathrm{s2}}/(2x_{\mathrm{Nozzle-sk.2}})] \end{aligned} \tag{3.14}$$

typically spread of the transverse direction normally smaller than longitudinal. The summarized properties of a gas such as Ar, Xe, O_2, C_2H_2 are shown in Table 3.2. Generally, the jet temperature in the propagation direction is in a few K range and the divergence of transfer direction is in the range of hundreds of mK.

Table 3.2: The characteristics of supersonic jet for the target species

target	$\Delta p_{300\mathrm{K}}$	v_{jet}	$p_{\parallel}$	$T_{\infty,\parallel}$	$\Delta p_{\perp}$	$T_{\infty,\perp}$
Ar	8.35	560	18.7	?	0.14	0.08
Xe	15.2	309	33.9	?	0.25	0.08
O_2	7.5	741	19.8	13	0.15	0.12
C_2H_2	6.7	823	17.8	?	0.13	0.12

The gas jet passes two skimmers to cool down the temperature of the jet; meanwhile, the particle density n of the jet is also reduced. The supersonic gas jet's gas density could be expressed with Mach number M_a and heats ratio κ. The Mach number describing the expanded gas jet zones after the nozzle, which can also be determined with an empirical model as a function of distance x from the nozzle as:

$$M_a(\tilde{x}) = \tilde{x}^{\kappa-1}(b + \frac{c}{\tilde{x}} + \frac{d}{\tilde{x}^2} + \frac{e}{\tilde{x}^3}) \tag{3.15}$$

where the effective distance $\tilde{x} = x/d$ from x divide by the nozzle diameter d. Found that the empirical coefficient were:

$$\begin{aligned} b &= 16.5404 - 15.8215\kappa + 4.70182\kappa^2 \\ c &= -15.6286 + 15.1459\kappa - 3.73352\kappa^2 \\ d &= 13.1705 - 14.4312\kappa + 4.05912\kappa^2 \\ e &= -3.4116 + 3.7898\kappa - 1.07202\kappa^2 \end{aligned} \tag{3.16}$$

The supersonic gas jet density of the number of particles can be assessed at a distance of x along the jet propagation axis from the nozzle by:

$$N = n_0[1 + \frac{M_a(x)^2(\kappa - 1)}{2}]^{\frac{1}{1-\kappa}} \tag{3.17}$$

In our ReMi setups, we could usually achieve the lower target density in a range of $10^{10} - 10^{12}$ /cm^3. Comparing the particle density under the condition of 2 bar and 300K around $n_0 \approx 5 \times 10^{19}$ /cm^3. The reduction of the gas density is essential for single-molecule coincidently imagining to avoid influence such as a cluster effect.

3.2.2 Bubbler set up

In case we have to deliver the liquid molecules into our reaction chamber. We designed a setup with a temperature-controlled reservoir contained target liquid molecules called "bubbler". The helium as a carrier gas passed through a bubbler and picked up vaporized water molecules into our reaction chamber as shown in Fig. 3.11.

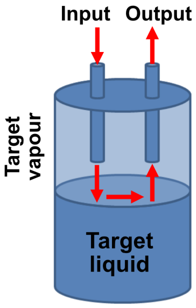

Figure 3.11: Typical cylindrical bubbler with a reservoir and two inlet/outlets [123]. The target liquid is stored in the temperature-controlled reservoir.

3.2.3 Time-of-flight spectrometer

Time-of-flight spectrometer (ToF) technology could be traced back to the 1950s [124]. Its resolution and signal-to-noise ratio has significantly improved later on and has outstanding performance in studying the ionization behaviour of atoms and molecules [125]. The basic working principle of the ToF is to use the flighting time to measure the initial kinetic energy of ionized electrons and to distinguish different types of ions through the charge-to-mass ratio to collect the output. Since the initial momentum $P_{\mathrm{z,i}}$ of the charged particle is tiny, it is difficult to fly to the detector unobstructedly. A pair of electrodes produced voltage ΔU in the ionization zone to make a specific potential difference between the plates. Various charged particles gain specific kinetic energy after being accelerated by an external electric field. A distance of l_a is for these particles to pass through the acceleration zone is:

$$l_a = \frac{1}{2}\frac{q\Delta U}{ml_a}t_a^2 + \frac{P_{\mathrm{z,i}}}{m}t_a + z_0 \tag{3.18}$$

Afterwards, these particles fly out of the acceleration zone and enter the fieldless flight drift zone at length l_d:

$$l_a = \frac{q\Delta U}{ml_a}t_a t_d + \frac{P_{\mathrm{z,i}}}{m}t_d \tag{3.19}$$

The t_a is the time required for the particles to pass through the accelerated flight zone at a distance of l_a and t_d is the time to pass through the field-free drift flight zone a distance of l_d.

The overall time of flying two-zone could be expressed as:

$$T_{\mathrm{oF}}(p_{\mathrm{z,i}}) = t_a + t_d = m\left(\frac{2l_a}{\sqrt{p_{\mathrm{z,i}}^2 + 2mq\Delta U} \pm p_{\mathrm{z,i}}} + \frac{l_d}{\sqrt{p_{\mathrm{z,i}}^2 + 2mq\Delta U}}\right) \tag{3.20}$$

The ± sign indicate the particles initial momentum in the $\pm\mathbf{e_z}$ direction regarding the ionization happed at $(x_0, y_0, z_0) = 0$. Taking into counts we don't have a drift length ($l_d = 0$) in our ReMi setup . For the tunnelling ionization, the initial momentum of ion could assume $P_{\mathrm{z,i}} = 0$, the t_{oF} could simply written as:

$$t_{\mathrm{oF}} = \sqrt{\frac{2l_a^2 m}{\Delta U q}} \tag{3.21}$$

The time required for the detector to detect the signal of the particle is proportional to the $\sqrt{m/q}$, a small mass and a high charge particle arrives at the detector earlier. The ToF spectrometer uses this principle to allow particles with different charges to fly unobstructedly in a high vacuum environment. The difference in flight time distinguishes different masses and charges taken by flying the same distance to arrive at the detector. We can isolate the ion signals interested by selecting the detection time zone.

Longitudinal momentum. An analytical solution of initial longitudinal momentum distribution for a certain t_{oF} could express as:

$$P_{\mathrm{z,i}} = -\frac{1}{2}\frac{q\Delta U}{l_a} t_{\mathrm{oF}} + \frac{m l_a}{t_{\mathrm{oF}}}, \tag{3.22}$$

which mainly is reconstructed by the ToF and static electric field.

Transverse momentum of electron. The initial transverse momentum $\mathbf{P}_{\mathrm{tr,i}}$ is mainly influenced by the magnetic field $\mathbf{B}$, the magnetic field leads to the cyclotron motion of the charged particle and constrains the particles to the centre of the detector. The angular frequency of particles cyclotron motion is defined as:

$$\omega_c = \frac{2\pi}{t_c} = \frac{|q|B_z}{m} \tag{3.23}$$

t_c is the cyclotron period, in the Fig. 3.12 shows the sketch for the reconstruction of the transverse momentum (red arrow), the angle $\alpha = \omega_c t$ is the particle moved along the cyclotron axis. The radius of the cyclotron trajectory is defined as:

$$R_c = \frac{r}{2|\sin(\alpha/2)|} \tag{3.24}$$

Consider the Lorentz force as a Centripetal force, the equation of tangential speed along with the radius of curvature R_c could express as:

$$F = q\mathbf{v} \times \mathbf{B} = \frac{m\mathbf{v}^2}{R_c} \tag{3.25}$$

Combining theses two equation above, initial transverse momentum $p_{\mathrm{tr,i}}$ of the charged particle could be express as:

$$p_{\mathrm{tr,i}} = \frac{\omega_c m r}{2|\sin(\omega_c t/2)|} \tag{3.26}$$

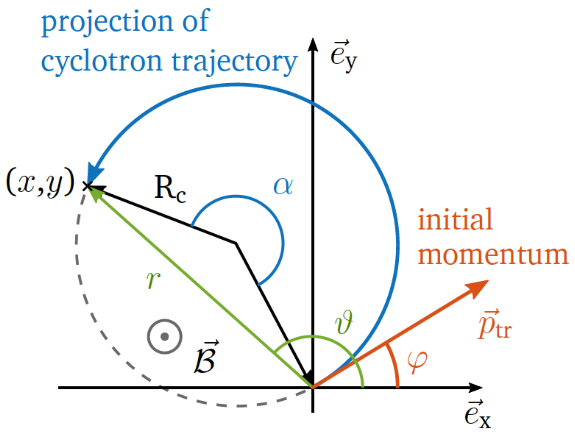

Figure 3.12: **Electron cyclotron trajectory.** A sketch for the reconstruction of the transverse momentum (red arrow), the angle $\alpha = \omega_c t$ is the particle moved along the cyclotron axis. The distance of green arrow r is defined as $r = \sqrt{x^2 + y^2}$.

The emission angle is linked to the polar angle θ of the impact position and cyclotron angle as:

$$\phi = \theta - \frac{\mathrm{mod}_{2\pi}(\omega_c t)}{2} \tag{3.27}$$

Where θ could be calculated from the hit MCP position of x and y. To be noticed, the Eq. 3.26 register the cyclotron trajectory of electrons when t_{oF} equal to the integer multiples of cyclotron period t_c, the transverse momenta reaches to infinity $p_{\mathrm{tr}} \to \infty$. Because the electron will return to the "original" position in the traverse direction, electrons hit the identical spot of the MCP. We could not reconstruct the initial transverse momentum via the Eq. 3.26. The singularity point for $t_{\mathrm{oF}} = N t_c, N \in \mathbb{N}$, we called it as cyclotron node or node.

Transverse momentum of ion

For the heavy particles like ions $(m/g \gg 1)$, transverse momentum of ions can be simplified as:

$$\mathbf{p}_{\mathrm{tr,i}} = \begin{pmatrix} p_{\mathrm{x,i}} \\ p_{\mathrm{y,i}} \end{pmatrix} = \frac{m}{t_{\mathrm{oF}}} \begin{pmatrix} x \\ y \end{pmatrix} \tag{3.28}$$

3.2.4 Detection system

We will go through the detail of the detection system that happened in the main chamber. After the target gas-phase atoms or molecules interact with the laser beam to produce photoelectrons and ions, the particles are accelerated by a two-pole voltage and then fly to a detector with a microchannel plate (MCP) to be detected. The detector's signal and trigger signal output are often converted into standard nuclear instrumentation module (NIM) signals by the constant fraction discriminator(CFD). A component beam of mid-infrared laser pulse output by the OPCPA laser system is converted into an electrical signal by a photodiode as a trigger signal to trigger the time-to-digital (TDC) conversion card. Finally, the computer stores the digital signal and performs further analysis and processing.

3.2.5 Micro channel plate (MCP)

MCP is a large-area high-gain detector that can detect electron and ion signals. The structure and working principle of MCP are shown in Fig. 3.13. There are about million thin-walled glass tubes with high resistivity regularly distributed inside, and the inner wall of each micropore (microchannel) has an electric cathode material with a high secondary electron emission coefficient and is fixed at a certain angle with the surface. Its working principle is similar to that of a photomultiplier tube: when MCP has applied thousands of volts, the charged particles enter the micropores with specific kinetic energy under the action of the voltage difference between the ground grid and the MCP front plate and then collide the hole wall. Driven by the electric field, the electron bombards the tube wall to emit secondary electrons. These secondary electrons are accelerated to bombard the tube wall to emit more secondary electrons, resulting in an avalanche effect, thus forming a continuous electron multiplication and output the other side of the channel. A charged particle can produce up to 10^3 electrons.

The hitting timing information t_{MCP} can be associated with a time zero from a photodiode. The time-of-flight of the charged particle can consequently be determined as

$$t_{\mathrm{oF}} = t_{\mathrm{MCP}} - t_{\mathrm{trigger}} + t_0 \tag{3.29}$$

with a global timing offset t_0.

The operating environment of the MCP is generally $< 2 \times 10^{-6}$ mbar and the range of temperature from -50 to 70 ^{0}C to avoid MCP breakdown. MCP also should always be placed in a vacuum environment to avoid being polluted by water vapour and dust in the air. The detector system may vary as different companies and different modules. Our Delay line Detectors system from RoentDek consists of 25 µm pore size and 32 µm centre-to-centre spacing providing position resolution <0.1 mm, temporal resolution <0.2 ns, rate capability up to 1MHz and multi-hit dead time at 10 - 20 ns.

MCP detects the charged particle's spatial information but does not include the spatial information of amplified electronic signals. Delay line anodes (DLAs) or camera is equipped behind the MCP. Delay lines have the advantage of single-particle detection and assigning the 3D momentum to any particle via linking a detected position with the ToF. Consequently, we could also perform coincidences between multiple particles considering momentum conservation. In addition, DLAs is typically advantageous with low-count high-rep rate sources (or vice versa, these sources are advantageous for delay lines). Cameras have the advantage of capturing many particles at once, but only 2D. In photoionization, this is often sufficient enough. It is excellent to perform a low-rep rate beam source and many particles per shot.

To retrieve the single molecular dynamic hence, our MCP is equipped with two vertically oriented DLAs. The delay line is a copper wire wound on an insulating plate (ceramic) to form a parallel and evenly spaced grid. These lines are usually added voltage positively from +200 V to +500 V. Consequently, the secondary enhanced electronic signal

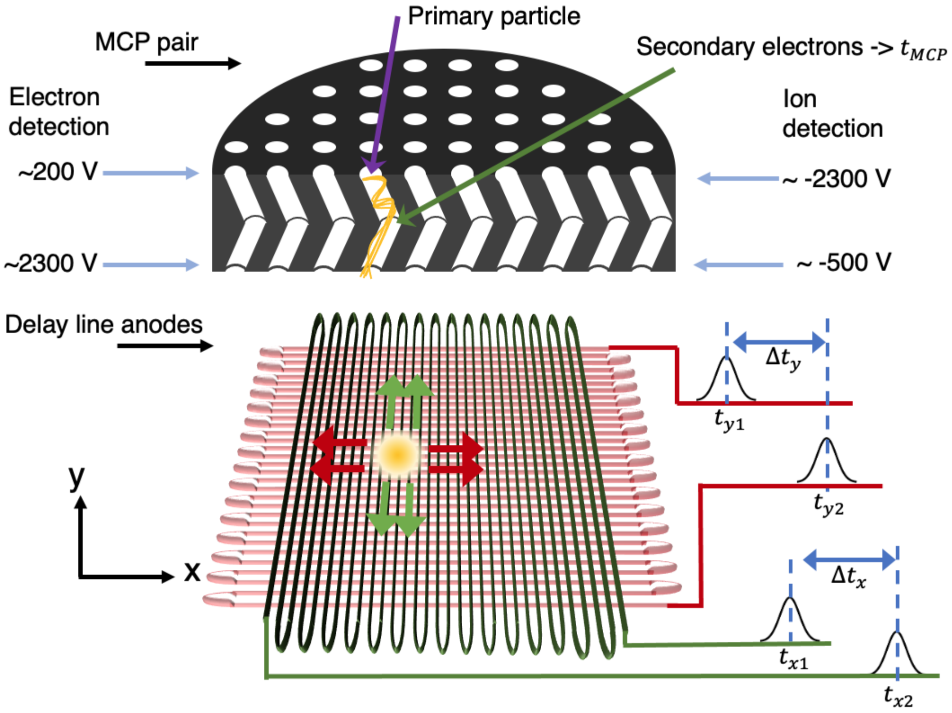

Figure 3.13: **MCP detector and delay line.** (a) The structure and working principle of MCP. The charged particles enter the micropores with specific kinetic energy under the action of the voltage difference between the ground grid and the front plate of the MCP and then collide the hole wall. Driven by the electric field, the electron bombards the tube wall to emit secondary electrons. These secondary electrons are accelerated to bombard the tube wall to emit more secondary electrons, resulting in an avalanche effect. (b) MCP is equipped with two vertically oriented Delay line anodes (DLAs). The delay line is a copper wire wound on an insulating plate (ceramic) to form a parallel and evenly spaced grid. The time difference between the arrival of these detection signals at the two ends indicates the spatial position of the impact.

hits the parallel wires to generate electric charges, propagating to both ends of the delay line wires as a pulse signal. The time difference between the arrival of these detection signals at the two ends indicates the spatial position of the impact. Since two vertically intersecting DLAs are used, the spatial position of the electron could be determined by the time difference as:

$$\begin{aligned} X &= v_\perp(t_{\mathrm{x1}} - t_{\mathrm{x2}}) \\ Y &= v_\perp(t_{\mathrm{y1}} - t_{\mathrm{y2}}) \end{aligned} \tag{3.30}$$

The $v_\perp$ is the propagation speed of the electric signal in the copper wire. The sum of time signal $t_{\mathrm{sum,x/y}} = t_{\mathrm{x/y,1}} + t_{\mathrm{x/y,2}}$ is always a constant due to the fixed length of the copper wire. The difference of time signal reconstructs the position where particles hit on the detector.

3.2.6 Constant fraction discriminator(CFD)

To let the signal processing in the ”counting card”, the coupling box is needed to convert the high-voltage signals of the MCP and DLAs into low-voltage signals. In the DLAs setup, two insulated copper wires are coiled in each direction, called the signal and reference wires. Only if the signals of two wires from each end of the wire are detected in the coupling box, then the electric signals $t_{\mathrm{x/y}}$ are sent to the counting card.

After the coupling boxes, a totally of 11 signals contain ten signals ($t_{\mathrm{MCP}}, t_{\mathrm{x1}}, t_{\mathrm{y1}}, t_{\mathrm{x2}}, t_{\mathrm{y2}}$) respectively from MCP of electron and ion, plus one the laser trigger signal from photodiode. All signals individually are first amplified via a fast, wide-bandwidth amplifier (Ortec - FTA820A). They are then passed by a constant fraction discriminator (CFD, RoentDek - CFD4b) as a noise filter. The primary function of CFD is to discriminate the same signal as long as its amplitude exceeds the discriminator's threshold to avoid the signal being too strong or too weak to be discriminated.

In a traditional threshold discriminator, the same signal with various amplitude may output differently rise times t_{r}, leading to the time starting point of the crossover with the threshold being different, as shown in Fig. 3.14(a). The phenomenon of time walk generate the time delay of the NIM signal, and it may cause the signal generated at the same time impossible to be observed. Time walk will cause significant errors in the measured ultrafast electronic signals.

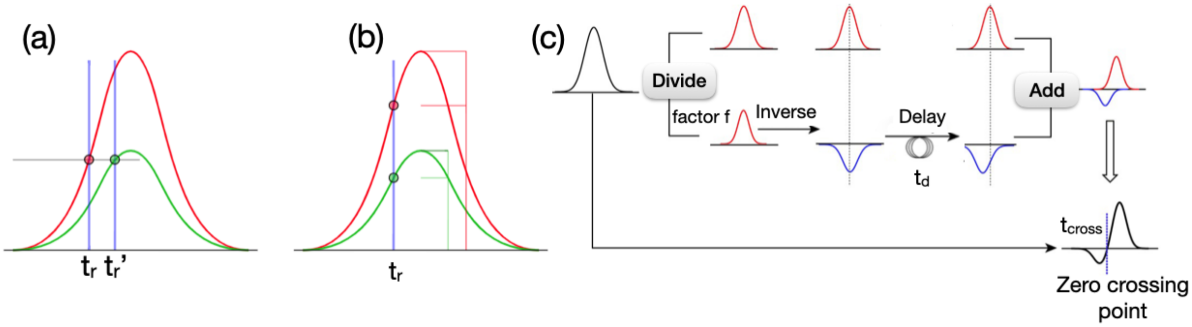

Figure 3.14: **Threshold discriminators and constant fraction discriminator(CFD). (a)** The same signal with various amplitude may output differently rise times t_{r} and t'_{r} for threshold discriminators. **(b)** CFD avoids is capable of discriminating the signals sent at the same time. **(c)** The working principle of CFD. The CFD attenuates the signal by a factor of f and at the same time reverses and delays the signal for a time t_d, and then superimposes the two signals,

In contrast, CFD can avoid the ”time walk” of the discriminated signal using the edge flipping method. The CFD attenuates the signal by a factor of f and at the same time reverses and delays the signal for a time t_d, and then superimposes the two signals, as shown in Fig. 3.14(c). Finally, using the intersection of the signal and the horizontal axis at t_{cross} (zero crossing point) as the starting point of the signal. We could derive that $t_{\mathrm{cross}} = t_d/(1-f)$, which is not related to the signal amplitude. Hence, CFD avoids time delay and is capable of discriminating the signals sent at the same time.

3.2.7 Time-to-Digital Converter(TDC)

After the filters of CFD, all 11 signals are brought into a time-to-digital converter (TDC) card (*C.A.E.N. - V1290N*). Our TDC reach a time resolution of 25 ps (effectively, it is around 100 ps depending on calibration), a maximum readout window $t_{\text{window,max}}$ up to 52 µs and a dead time of 5 ns, which is essential for multiple hit detection. TDC is an integrated chip that converts signals generated at different times into digital signals, and its working principle is shown in Fig. 3.15. During the period from the trigger signal start t_1 to the end t_2, the number of clock rates is recorded and the time interval $t_2 - t_1$ is converted into digital information. In the experiment, we used a photodiode to detect the laser shot as a trigger signal, recording the time information of the detected particles' signal generated in the action zone of each laser pulse. The TDC receives a trigger signal as an event, and the software can store different events as a stack on the computer. In addition, according to the experiment's needs, we can set the parameters of the TDC to work in different modes as set it to work only in a certain period to make the trigger more effective.

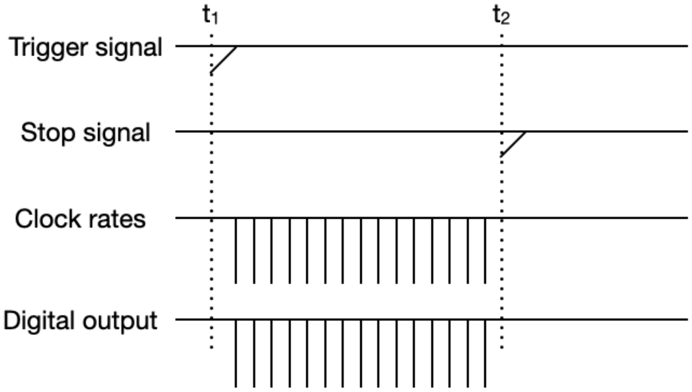

Figure 3.15: **The working principle of time-to-Digital Convertor(TDC).** TDC is usually used to determine a time interval and convert it into digital (binary) output

Here, laser pulse as a trigger initiates the TDC readout. The time interval between two laser pulses consistently is named a ToF window, which is 6.25 µs according to the laser system running at 160 kHz. Depending on the mass of charged particles, electrons always travel faster, arriving in the first ToF window. Heavier mass like ion could arrive at the first, second or third ToF window. We must pre-calculate the ion's ToF and adjust the TDC readout window and ReMi hardware ion ToF window.

3.2.8 Data analysis

In order to process a large amount of data generated by strong field-induced ionization and fragmentation, an automated data analysis program is required. In our laboratory, the data is processed using the GENERiC code written by Arne Senftleben (et al.) at MPIK (Max-Planck-Institut für Kernphysik, Heidelberg, Germany). GENERiC code can be hosted and executed in the Go4 framework developed by the GSI Helmholtz Centre for Heavy Ion Research. Go4 is an open-source, real-time, object-oriented, online/offline data analysis graphical user interface (GUI), integrating MBS (multi-branch system, a framework for experimental data acquisition) streaming media server to convert a data stream into the multiple-step analysis. Therefore, Go4 provides many C++ classes that extend the ROOT framework developed at CERN (European Organization for Nuclear Research) and are often used for particle and high energy physics data analysis.

Figure 3.16: **The pipeline of the GENERiC code.** The pipeline consists of three main processing steps: extract step, unpack step, and calc step.

The GENERiC code is used to process all the data signals extracted from the TDC of the ReMi electronic device to reconstruct the momentum vector of the charged particles and their physical properties. In Fig. 3.16, the pipeline of the GENERiC code is depicted. It consists of three main processing steps: extract step, unpack step, and calc step. The signal in the MBS contains the original timestamps of the signals from the MCP, DLA, and photodiode, which correspond to a particle impact detector. In the extract step, raw event data directly from the MBS stream server or data files are converted into basic event objects. Each TDC channel is plotted as a histogram as a function of its time bins. We could monitor the noise level of each channel and modify the CFD threshold for all channels. In the unpack step, with ToF and position hit on the MCP of the charged particle, we could calibrate the XY position and ToF of electrons and ions. In the calc step, with information on the static electric and magnetic field, we could trace back the particle's trajectory to reconstruct the three dimensions momenta of ion and electron at the time after the ionization. Other physical properties such as kinetic energy release (KER) and solid angle distribution of ionization could also retrieve from 3D momenta. Coincident filters could also be applied by electron and ion momentum conservation.

3.2.9 Capabilities of the system

The sensitivity of the charged particles detection in the measurement mainly depends on the pore size and centre to centre spacing on the MCP detector, the strength of the static electric field and the magnetic field. The position resolution of MCP cannot be improved; therefore, it is necessary to scale the static extraction field appropriately according to the experimental plan to cover the required momentum range.

Longitudinal acceptance. Longitudinal acceptance is solely dependent on external static electric field strength E_z. The particles have an infinite acceptance in their respective forward direction, indicating accelerated directly to their respective detector ($+\mathbf{E}$ for ions and $-\mathbf{E}$ for electrons). When the initial longitudinal momentum of particles in the backward direction is sufficient to overcome the opposite acceleration, they will not be detected. In other words, if the initial longitudinal momentum is too large in the opposite direction(comparing the accelerated force of the static electric field direction), the static electric field could not drive the particles to the detector. Hence, the minimum detectable momentum is:

$$p_z \geq -\sqrt{\frac{2|q\Delta U|}{m}} \tag{3.31}$$

Transverse acceptance. The discretion of transverse acceptance is restricted differently for ions and electrons due to their different performance in the magnetic field.The maximum momentum acceptance for in transverse direction is solely dependent on external static magnetic field strength and the diameter of the detector:

$$p_{\mathrm{tr,ele}} \leq \frac{r_{\max}}{2} e B_z, \tag{3.32}$$

while the transverse kinetic energy yields

$$E_{\mathrm{kin,tr,ele}} \leq \frac{r_{\max}^2}{8m} e^2 B_z^2, \tag{3.33}$$

The radius of our MCP is 40mm, which means the practical maximum radius $r_{\max} = 40mm$ regarding the electrons do not contain initial transverse momentum and strike directly in the detector centre. The discontinuities or nodes area also need to be considered when discussing the transverse acceptance of electrons. The momentum acceptance is zero since all electrons hit the MCP at the same central position.

The transverse acceptance of ions is mainly limited by the diameter of the detector and the electric field strength due to the influence for heavy mass ions is neglectable. Thus, the maximum transverse kinetic energy can be evaluated with the flight time for ions, results in

$$E_{\mathrm{kin,tr,ion}} \leq \frac{r_{\max}^2}{2l_a} |q\Delta U|. \tag{3.34}$$

3.2.10 Momentum resolution

Theoretically, the momentum acceptance of ReMi can increase indefinitely as the static field increases, but the momentum resolution deteriorates as the field strength increases. The momentum resolution Δp is resolved by applying the Gaussian error propagation to the Eqs. 3.20 and 3.26 where presented longitudinal and transverse momentum, we take into account the major uncertainties: the δt connected to determining the correct time zero of the laser triggering and δr of the exact impact point of the MCP and DLA. The longitudinal momentum resolution could express as:

$$\Delta p_z = |\frac{1}{\partial t/\partial p_z}\delta t|^{l_d=0} = |-\frac{1}{2}\frac{q\Delta U}{l_a} - \frac{ml_a}{t^2}|\ |\delta t| \tag{3.35}$$

For the transverse momentum resolution:

$$\Delta p_{\mathrm{tr}} = \frac{m\omega_c}{2|\sin(\omega_c t/2)|}\sqrt{\delta r^2 + (\frac{r\omega_c}{2\tan(\omega_c t/2)})^2\delta t^2} \tag{3.36}$$

Here, $t = t_{\mathrm{oF}}$. The momentum resolution as function of the δt and δr, the variables t and r can be substituted by equations for their related momentum components p_z (Eq. 3.20) and p_{tr} (Eq. 3.26). Therefore, the two the momentum resolution equations could be also as function of initial momentum variables: δp_z (p_z) and δp_{tr} (p_z, p_{tr}), it shows the particles with different initial momentum at different resolutions are to be detected. Normally, systematic uncertainties of the ReMi estimated as δt = [0.5;1] ns and δr = [0.5;1] mm depending on the setting of the CFDs. Furthermore error such as acceleration length δl_a could vary as focal spot position varies, and filed strength δE and δB can result from instabilities of the instrument respectively. The overall uncertainty could be calculated as:

$$\Delta p = \sqrt{\Delta p_z^2 + \Delta p_{\mathrm{tr}}^2} \tag{3.37}$$

And energy uncertainty could be calculated as:

$$\Delta E = \frac{1}{m}\sqrt{(p_z \Delta p_z)^2 + (p_{\mathrm{tr}} \Delta p_{\mathrm{tr}})^2} \tag{3.38}$$

We also need to be noticed, the Eq. 3.26 indicate the cyclotron motion of electrons, when time of time of flight t_{oF} equal to the integer multiples of t_c, the resolution of transverse momenta reaches to infinity $\Delta p_{\mathrm{tr}} \to \infty$, we could not considering analysis for electron around $t_{\mathrm{oF}} = N t_c (N \in \mathbb{N})$ i.e. node area. A higher static field generally leads to 4π solid acceptance for the larger momenta of both electrons and ions. However, higher fields lead to higher momentum uncertainties which blur out the structure retrieved in the momentum distribution. Hence, the magnitude of the static field needs to be adjusted to fulfil each experimental condition. In principle, we should keep a relatively lower static field while the catching-all particle is also needed.

Chapter 4

Imaging an isolated water molecule

Contents

This chapter will explore the retrieve of the molecular structural information utilising laser-induced electron diffraction (LIED). LIED is a state-of-the-art technique that combines an intense laser source and a complete three-dimensional electron-ion coincidence detection system. The chapter is organised as follows: Sec 4.1 describes the advantages and limitations of diffraction structural imagining techniques like X-ray diffraction (XRD) and ultrafast electron diffraction (UED); Sec 4.2 represents imaging an isolated water molecule via LIED.

4.1 Limitations of X-ray and electron incoherent scattering

X-ray diffraction (XRD) and ultrafast electron diffraction (UED) are the most established techniques to retrieve gas-phase molecular structure based on diffraction. Incident photons/electrons scatter with the target and result in the diffraction pattern in the far-field. A the Fourier-transform reveals structural information of the near field.

Based on the current technologies, X-ray beam, parameters from the Linac Coherent Light Source (LCLS), could reach wavelength of 1.494 Å with pulse duration of 30 fs [126]. In comparison of the electron scattering, the 3.7 MeV-UED system at the SLAC

National Accelerator Laboratory could reach electron beam wavelength up to 0.003 Å and pulse duration to 230 fs [127]. According to last information from the SLAC National Accelerator Laboratory website, the facility could reach repetition rates up to 360 Hz and electron pulse duration shorter than 150 fs dependence the beam setup [128]. Their relative merits are shown in Table 4.1.

Table 4.1: Currently X-ray and UED resolution

	Energy	Wavelength	Photons or electrons per pulse P_0	Pulse repetition rate	Pulse duration
X-ray[126]	8.3 KeV	1.494 Å	10^{12} photons/pulse	120 Hz	30fs
MeV-UED[127]	3.7 MeV	0.003 Å	3.7×10^4 e^-/pluse	120 Hz	230fs
keV-UED[129]	30 KeV	0.067 Å	2.5×10^3 e^-/pluse	50 000 Hz	> 1ps

X-ray diffraction imaging with Free Electron Lasers pulses necessitates a large facility and a precise balance between adequate beam brightness and the damage threshold of the sample. The photon scattering probability is five orders lower than the one for electron shown in Table 4.2. Relativistic 3.7 MeV - UED could reach a sub-Ångstrom spatial resolution but thus vastly challenging to reach with a sub-100 fs temporal resolution. Table 4.2 exhibits the total scattering probability, P_{scatt}/P_0, measured from one particle scattered off one target N-methyl morpholine molecule within momentum transfers from 0.5 to 20 Å^{-1}. The Scattered particle count , P_{scatt}, calculated using P_0 values from Table 4.1 [130].

Table 4.2: X-ray and UED scattering probability

	39.5 keV X-rays	30 keV electrons	3.7 MeV electrons
Total scattering probability, P_{scatt}/P_0	1.36×10^{-23}	9.01×10^{-18}	1.30×10^{-18}
Scattered particle count, P_{scatt}	1.36×10^{-11}	2.25×10^{-14}	4.81×10^{-14}

A remedy table-top method is highly required, especially for imaging gas-phase molecular dynamics that provide the combined adequated spatial and temporal resolutions. Laser-induced electron diffraction (LIED) is a method based on self-imaging a target structure using the molecule's own emitted attosecond electron wave packet during the laser-induced re-collisions process. It benefits from a larger cross-section of electrons than photons. In addition, the returning single electron wave packet coherent scatters the target providing a much shorter temporal resolution than UED. The spatial resolution depends on the wavelength of the returning probed electron wave packet (EWP), and temporal resolution depends on the laser and EWP pulse duration. LIED typically offers the electron returning energy 50 eV - 500 eV attained De Broglie wavelength shorter than 1.6 Å (Fig. 2.8), which is satisfactory the spatial resolution to insight molecular dynamics respecting the typical molecular bond length is around 1 Å. The pulse duration of laser could easily reach sub 100 femtosecond (fs; 1 fs = 10^{-15} s), and EWP is in attosecond level, advancing the LIED to achieve sub-Ångström spatial and sub 100 fs temporal resolution. In particular, LIED observed that the C-H internuclear distance doubled 9 fs after deprotonation in $[C_2H_2]^{2+}$ [9], which other electron-diffraction based methods such as UED [131, 8] still blind to scatter against the most elusive scatterer, the hydrogen atom. Here, as a primary step towards imaging the large complex molecular structures, we present the retrieval of the most simple liquid molecules - water H_2O via the LIED technique.

4.2 Imaging isolated water molecules using attosecond electron wave packets

Water (H_2O) is one of the most important molecules in our life, which perform as an essential solvent and metabolite in living organisms [132, 133]. Probing the properties of water, such as its geometric structure and dipole moment, can provide valuable insights into the mechanisms of biologically important processes such as protein folding in water, water-protein electrostatic interactions that can determine solvation shell formation. The solvation shell water exchanges dynamically with bulk water in the layer. It changes processes ranging from membrane formation to protein folding [134, 135, 136]. Control over chemical reactivity through mode selective chemistry [137, 138], strong-field perturbation of water dissolution [139], and influence of vapour-liquid nucleation [140] by modifying the dipole moment of water. Thus, distorting the geometric structure of water will have important and wide-reaching implications. Such distortion can be achieved using intense fields with field strengths on the order of the Coulombic attraction between electrons and protons. Jung et al. [141] theoretically demonstrated that significant structural change in water could be achieved using electric fields on the order of 0.15 - 0.20 V/Å. The authors also show that each water molecule undergoes a local electric field of around 2 V/Å from nearby water monomers in liquid water in the absence of an external electric field [141]. Shunping et al. demonstrated that the dipole moment orientation of the molecule relative to the external electric field was crucial; if the dipole moment of the molecule is aligned with (against) the external electric field, then the molecule is stretched and bent (contracted and straightened) with increasing field strength [142].

Here, we investigate the response of an isolated water molecule to different field strengths that are typically experienced in liquid water under natural conditions. We use intense ($I > 10^{13}$ $\mathrm{Wcm^{-2}}$), ultra-short 97 fs laser pulse with field strengths of approximately 3 V/Å to investigate the response of an isolated water molecule to different laser intensities. The 50 ml pure deionized liquid water from Sigma Aldrich in the bubbler's reservoir is delivered to the interaction chamber carried by the 100 mbar helium gas. We directly retrieve structural information of H_2O^+ in the ground electronic state using LIED. We resolve the field-driven symmetric stretching of the O-H bond in H_2O^+ using Fourier transform (FT) the variant of LIED (FT-LIED) [143, 144] with picometre and femtosecond spatio-temporal resolution. In FT-LIED, the geometric structure can be directly retrieved without any prior knowledge nor the use of retrieval algorithms. This is important since structural information is typically indirectly retrieved using microwave and rotational spectroscopy [145, 146], which, in contrast, require ab initio calculations to interpret the measured data.

4.2.1 FT-LIED analysis

Here, we present the structural retrieval process with FT-LIED data corresponding to $U_\mathrm{p} = 150$ eV at a peak laser intensity of 1.6×10^{14} Wcm^{-2} (3.5 V/Å). The detector captured the electron and ion 3D momentum original in (x, y, z) Cartesian coordinate (Fig. 4.1). The ionization events are cylindrically symmetric along the laser polarization direction. In order to simplify the problem and efficiently analyze the data, we convert the 3D cartesian coordinate to the 3D cylindrical coordinate $(\rho,\ z,\ \phi)$, then integrated over the azimuthal angle to reduce the 3D cylindrical coordinate to a 2D cylindrical coordinate.

$$\begin{aligned} dV &= dxdydz \\ &= \boxed{\rho}\,d\rho dz d\phi \end{aligned} \tag{4.1}$$

According Eq. 4.1 of the volume element, an appropriate Jacobian $J_{\text{cyl./Cart.}} = 1/\rho$ (highlighted by a box) need to be implemented due to the coordinate transfer for discrete elements.

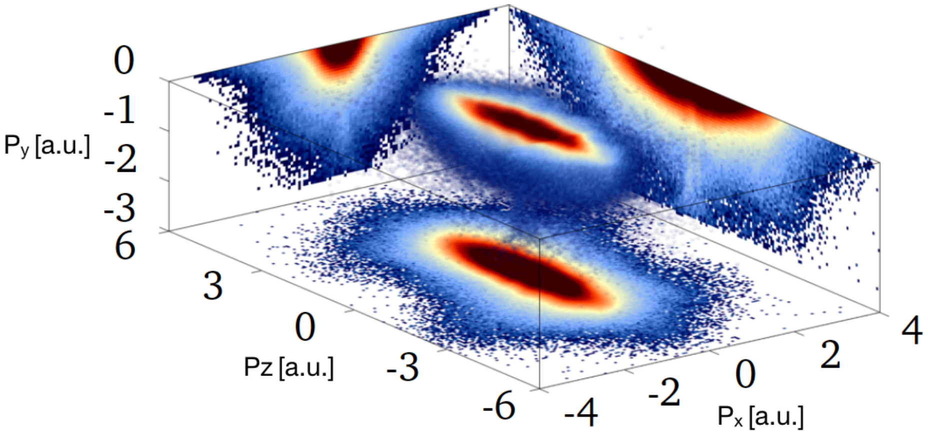

Figure 4.1: The measured 3D electron momentum distribution. The detector captured the 3D electron momentum coincidence with the respective H_2O^+ ions in (x, y, z) cartesian coordinate.

The coordinate dimension mitigated from the initial 3D Cartesian coordinate to 2D cylindrical coordinate, the new 2D coordinate is constructed with longitudinal momentum P_l as parallel to the laser polarization and transverse momentum P_t direction is perpendicular to the laser polarization. In the practice of FT-LIED configuration, laser polarisation is fixed in the z-direction, the mathematical process of converting to the $P_\mathrm{l}P_\mathrm{t}$ map and an appropriate Jacobian which multiply for all matric elements described by Eq. 4.2:

$$\begin{aligned} P_{\mathrm{l}} &= p_z \\ P_{\mathrm{t}} &= \sqrt{p_x^2 + p_y^2} \\ J &= \frac{1}{|p_{\perp}|} \end{aligned} \tag{4.2}$$

Figure 4.2 shows the two-dimensional momentum distribution of P_{l} and P_{t} momenta for all electrons after the conversion. We detect both "direct" electrons (i.e. electrons with $P_{\mathrm{l}} < 4.7$ a.u. ($2U_{\mathrm{p}}$ cut off in the rescattering frame) which have escaped the laser field without recollision) and rescattered electrons (i.e. electrons with $P_{\mathrm{l}} \geq 4.7$ a.u.) which rescatter with parent's ion. To extract the field free interference signal, detected rescattering momentum (k_{resc}) is needed to convert to the returning momentum (k_{r}) via classical relation, which from the k_{resc} subtracted the vector potential (A_{r}) kick undergoing the strong mid-IR field(Eq. 2.80). Each measured k_{resc} correspondences a unique solution for k_{r} and A_{r} in the semi-classical model of long trajectory (Chapter 2). Since we operate in the FT-LIED configuration, we need the maximum momentum transfer range to achieve adequate special resolution. Only back-rescattering electrons ($P_{\mathrm{l}} \geq 4.7$ a.u.) with a rescattering angle, θ_r, of $170^o - 190^o$ are considered corresponding to a small scattering cone of $\Delta\theta_r = 10^o$ around the rescattering angle of $\theta_r = 180^0$. An energy dependent signal is extracted from the 2D momentum map by integrating a small block arc bin in momentum space (see Fig. 4.2) to obtain the total number of electron counts at various k_{resc}.

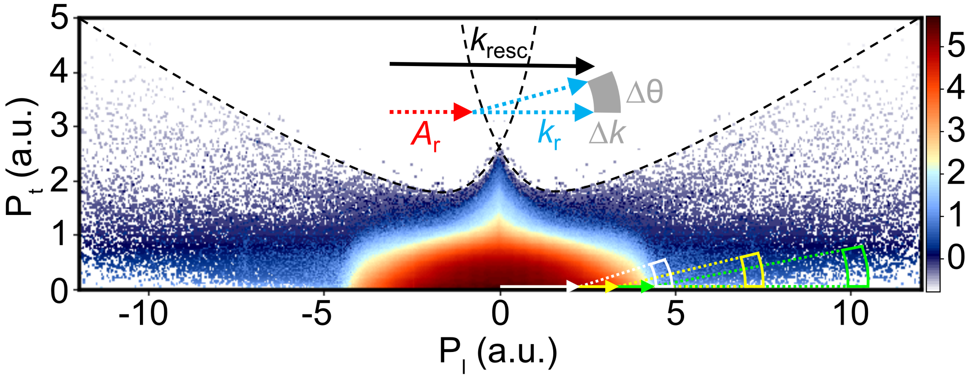

Figure 4.2: **FT-LIED extraction**. Longitudinal and transverse momenta two-dimensional map in atomic units. By subtracting the vector potential of the laser, A_{r}, from the rescattering momentum measured, k_{resc}, the return momentum k_{r} can be obtained, via $k_{\mathrm{r}} = k_{\mathrm{resc}} - A_{\mathrm{r}}$. The number of electrons is integrated by the area indicated with an arc at various rescattering momenta indicated by the white, grey and black arrows along with $P_{\mathrm{t}} = 0$. A schematic relationship of k_{resc}, k_{r} and A_{r} combining with the region encompassed by a small range of rescattering angles and momenta (grey shadow area), $\Delta\theta$ and Δk, respectively, are shown at the top of the figure. The dotted black lines represent the acceptance angle [147].

4.2.2 Electron-ion 3D coincidence detection

The coincidence detection capability of the ReMi ensures that the measured molecular interference signal originates from only the ion(s) of interest. This avoids background signals from competing processes, such as multi-photon ionisation and Coulomb explosion fragmentation, hindering structural retrieval. Meanwhile, these other laser-induced processes generate electrons with relatively small momenta, our analysis focuses on the highly energetic rescattering electrons as these correspond to our LIED imaging electrons. Figure 4.3a shows the time-of-flight (ToF) spectrum of all the measured positively charged fragments, with the most intense ToF peak at around 5.5 µs corresponding to the molecular ion, H_2O^+. The inset shows a close-up of the ToF spectrum around 5.5 µs correspondence mass-to-charge ratio (m/q) of 16 – 18 and the ToF range of the H_2O^+ peak indicated by the blue shaded region. Figure 4.3b shows the signal of electron counts extracted from all electrons (blue dotted trace) and coincidence electrons with H_2O^+ (solid black trace). It is created by integrating electron counts in the grey block arc area as shown in Fig. 4.2 with different k_{resc}. The $2U_{\mathrm{p}}$ and $10U_{\mathrm{p}}$ classical cut-offs are perceptible in both distributions, betokened by green arrows. The electron counts are quickly drop in the 0 - $2U_{\mathrm{p}}$ range (direct electrons) and reach a plateau amidst the 2 to $10U_{\mathrm{p}}$ (reascattering electrons). Moreover, the benefit of coincidence detection is highlighted in the inset of panel(b), the modulation of the molecular interference signal from the H_2O^+ coincidence electron appearing as more contrast and pronounced than that of all electrons.

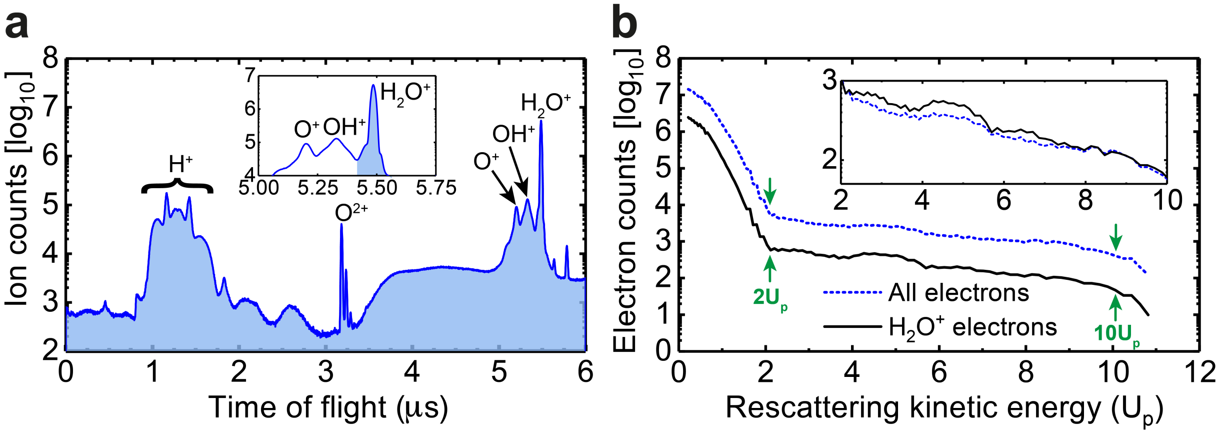

Figure 4.3: **Coincidence detection.** **(a)** The ion time-of-flight (ToF) spectrum up to 6 µs, with the pronounced peak around 5.50 µs belong to H_2O^+ signal. The inset shows a close-up of the ToF spectrum around H_2O^+ peak, the ToF range of the H_2O^+ peak indicated by the blue shaded region. **(b)** The logarithmic scale electron counts as a function of rescattering kinetic energy by a unit of ponderomotive energy, U_{p}=150 eV, the blue dotted trace shows for all electrons and coincidence electrons with H_2O^+ presented by solid black trace. Green arrows indicate the classical cut-offs for $2U_{\mathrm{p}}$ and $10U_{\mathrm{p}}$. The inset is a close-up view of the signal of electron counts between 2 – $10U_{\mathrm{p}}$, overlaying the two distributions on top of each other to highlight the benefit of coincidence imaging where more contrast interference signals are perceived.

4.2.3 Molecular structure retrieval

We produce a plot of electron counts measured in coincident with H_2O^+ that vary with return kinetic energy range from 80 to 460 eV, which corresponds to the rescattering energy plateau among $2U_\mathrm{p}$ to $10U_\mathrm{p}$ shown in Fig. 4.4a. We only analyse the rescattering range where a plateau exists in the signal (i.e. the $2U_\mathrm{p} - 10U_\mathrm{p}$ range). Here, the measured total signal ($\mathrm{I_T}$; solid blue trace) from the backscattered LIED electrons is plotted with a third-order polynomial fit to the empirical background (black dotted trace). In fact, $\mathrm{I_T}$ receives contributions from the coherent molecular interference signal ($\mathrm{I_M}$) and the incoherent atomic signal ($\mathrm{I_A}$). The empirical background from $\mathrm{I_A}$ is extracted using a third-order polynomial fit to the signal and is subsequently subtracted from $\mathrm{I_T}$ to obtain $\mathrm{I_M}$. Figure 4.4b shows the $\mathrm{I_M}$ function of momentum transfer, $q = 2 \cdot k_\mathrm{r}$. The observed oscillations in the $\mathrm{I_M}$ (solid blue trace) contains geometrical information about the molecule. The blue-shaded areas describe the estimated Poisson error of the experimental electron counts, which is the square root of the electron counts.

Applying Fast Fourier transform (FFT) algorithm to the molecular interference signal generates an FFT spectrum, as shown in Fig. 4.4c, a Kaiser window and zero-padding are applied before the transform. It is impossible to measure and operate an infinite signal in practical work, but taking its limited data for analysis and the truncated signal causes its spectrum to be distorted. A slowly truncated window function is used to reduce the side lobes of the window function to reduce spectral leakage, such as the Kaiser window. The advantage of the Kaiser window is that the adjustment parameter α can adjust the width of the main lobe and the size of the side lobes. As α increases, the width of the main lobe increases and the size of the side lobes decreases. $\alpha = 0$ corresponds to a rectangular window function. If α increases, the shape of the Kaiser window in the time domain will be close to the Gaussian curve. The peak concentration of the Kaiser window around frequency 0 is nearly optimal [148]. The FFT spectrum (solid blue line) fitted by two individual Gaussian fits (black dotted lines) and a sum of the two Gaussian fits (solid black line). The centres of the two FFT peaks with individual Gaussian fits are located at 1.24 ± 0.08 Å and 2.04 ± 0.08 Å.

We compare these two measured distances to the O-H and H-H internuclear distances of H_2O and H_2O^+ in their ground electronic state [145, 149] and first excited electronic states state reported in the literature, see Table 4.3. We find that the retrieved geometrical parameters from the FFT method are close to the H_2O or H_2O^+ ground electronic state. The excited electronic states of neutral H_2O are dissociative. We expected the bond length to stretch significantly by probing 7-9 fs after applying the LIED field. The second and third electronic excited state of the H_2O^+ cation are also dissociative[150]. The first excited electronic states H_2O^+, particularly the θ_HOH, is far from ground state H_2O^+. The ionization potential (I_p) of the highest occupied molecular orbital (HOMO) of neutral H_2O is 12.6 eV, which is around 2 eV lower than HOMO-1 ($I_\mathrm{p} = 14.7$ eV [151, 152], thus, the ionized electrons are expected to stem from the HOMO predominantly. This comparison allows to unambiguously assign the measured FT-LIED structure to a symmetrically stretched and slightly straightened H_2O^+ cation in the ground electronic state.

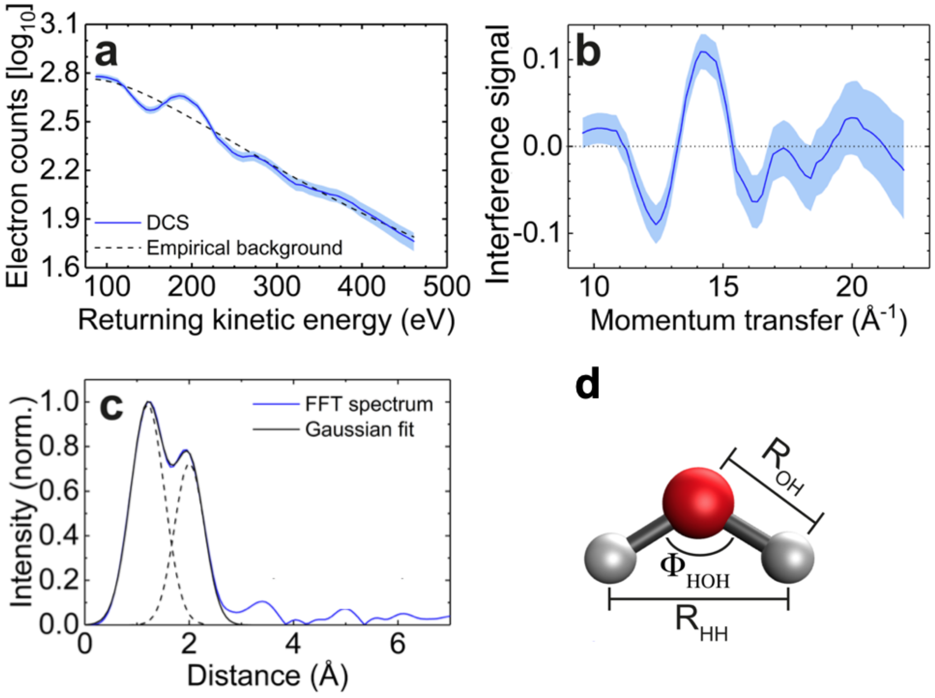

Figure 4.4: **H_2O Structure retrieval (a)** The total electron counts (I_T; blue trace) and the background incoherent atomic signal (I_A; black dotted trace) which is fitted by a third-order polynomial from total electron counts. **(b)** The coherent molecular interference signal (I_M), I_M=(I_T -I_A), as a function of momentum transfer. **(c)** Fast Fourier transform spectrum (blue trace) is fitted by two individual Gaussian fits (black dotted traces) and the sum of the two Gaussian fits (black solid trace). The molecular structural information extract as follow: O-H bond length, $R_{\mathrm{OH}} = 1.24 \pm 0.08$Å ; H-H internuclear distance, $R_{\mathrm{HH}} = 2.04 \pm 0.08$Å; and H-O-H bond angle, $\theta_{\mathrm{HOH}} = 110.7 \pm 6.6^0$. **(d)** A schema of the H_2O^+ shows the geometrical parameters.

4.2.4 Structure dependence on field strength.

To mimic the molecular structural change depending on the solvation shell, we expect H_2O to different field strengths, which act via the molecular dipole on its structure. The structural information of H_2O^+ and field strength are presented in Fig. 4.5 and Table. 4.4. The O–H and H-H internuclear distances increase simultaneously at these four different laser intensities. Field strengths from 2.5 V/Å to 3.8 V/Å leads to an increase of O–H (H–H) internuclear distance of 14%–35% (17%–35%) compared to the equilibrium field-free H_2O^+ ground-state structure. A least-squares fit was applied to the data with dashed-dotted traces, O–H and H–H internuclear distances linearly increase while H–O–H angle slightly decrease as rising field strength. We calculate the dipole moment of H_2O^+ cation with the complete active space self-consistent field (CASSCF) method using the aug-cc-PVTZ (correlation consistent-polarized valence double zeta) basis set [154]. An illustration of the structural information of H_2O^+ and calculated dipole moment are presented in Fig. 4.5(c).

Table 4.3: Molecular structural information for ground electronic state of H_2O and H_2O^+ [145, 149], and first excited electronic states H_2O^+ [153, 150]

	R_{OH}(Å)	R_{HH}(Å)	θ_{HOH}(deg)
$H_2O(\widetilde{X}^1A_1)$	0.96	1.52	105
$H_2O^+(\widetilde{X}^2B_1)$	1.00	1.63	109
$H_2O^+(\widetilde{A}^2A_1)$	0.99	1.98	180

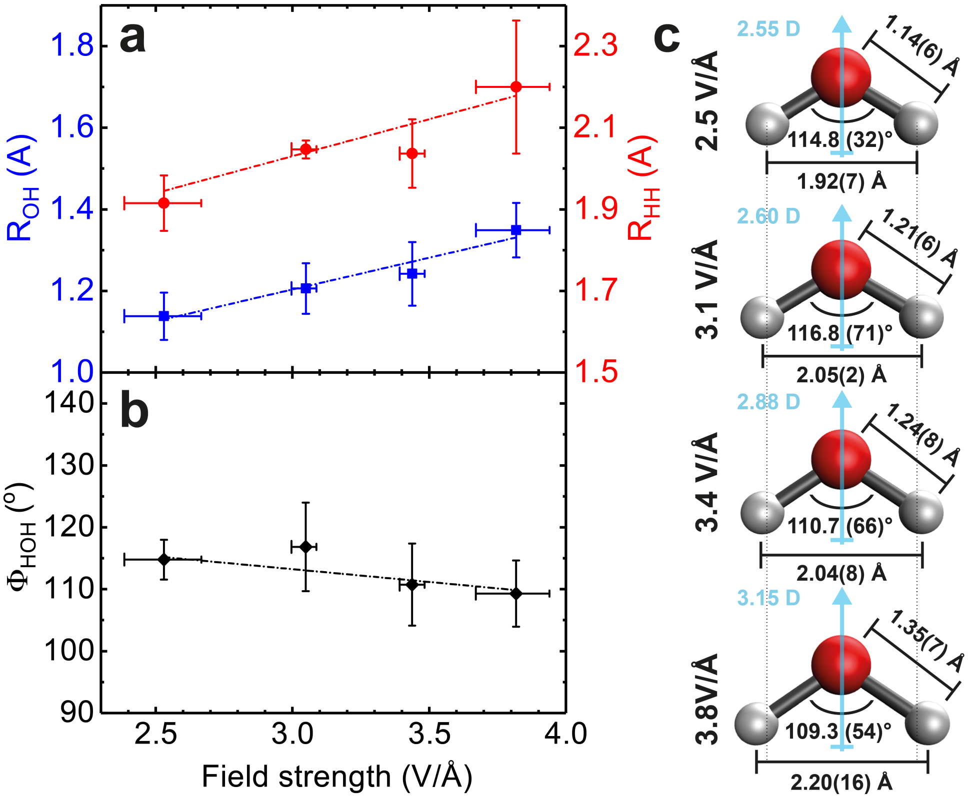

Figure 4.5: **H_2O^+ structure with different laser field strength.** **(a, b)** the O–H (blue), H–H (red) internuclear distances and H–O–H angle (black) as rising field strength. A least squares fit applied to the relative data with dashed-dotted traces. **(c)** An illustration of the structural information of H_2O^+ with four different laser field strengths and vertical blue arrow shown calculated dipole moment.

4.2.5 Error analysis

In a reaction microscope (ReMi), electric and magnetic fields determine the position in longitudinal momentum where the electrons undergo an exact multiple of the cyclotron motion and the transverse momentum error becomes infinite [147]. Which, for some settings, introduced a higher error on the U_{p} estimate that we derive from the longitudinal electron momentum distribution.

We performed a rigorous determination of the uncertainty value in field strength (proportional to U_{p}). Since the longitudinal momentum, $p_{\parallel}$, is proportional to U_{p}, we accu-

Table 4.4: H_2O^+ structure with different laser field strength

Field strength	R_{OH} (Å)	R_{HH} (Å)	θ_{HOH} (^{o})	Dipole moment
2.53 V/Å	1.138 ± 0.058	1.915 ± 0.068	114.770 ± 3.218	2.55D
3.08 V/Å	1.206 ± 0.062	2.047 ± 0.022	116.841 ± 7.145	2.60D
3.44 V/Å	1.242 ± 0.078	2.037 ± 0.084	110.738 ± 6.620	2.88D
3.87 V/Å	1.349 ± 0.067	2.200 ± 0.163	109.296 ± 5.363	3.15D

rately determine the U_p for each measurement from the $2U_\mathrm{p}$ cut-off that is present in the $p_\parallel$ distribution. Moreover, we examined the dependence of the $p_\parallel$ distribution on U_p, given as

$$p_\parallel = \frac{ml_d}{t_d} - \frac{mqUt_a}{l_a}, \tag{4.3}$$

where m and q is the mass and charge of the detected particle, respectively, U is the potential difference of our spectrometer electrodes, and l_a and l_d are the acceleration and drift lengths during the time-of-flight (ToF) of electrons. The drift time,

$$t_d = \frac{ml_d}{\sqrt{p_\parallel^2 + 2mqU}}, \tag{4.4}$$

and the acceleration time,

$$t_a = \frac{2ml_a}{\sqrt{p_\parallel^2 + 2mqU} \pm p_\parallel}, \tag{4.5}$$

contribute to the total time-of-flight (ToF) of the electron, t_ToF, given as

$$t_\mathrm{ToF} = t_a + t_d + t_\mathrm{shift}, \tag{4.6}$$

where t_shift is a small shift applied to the t_ToF in order to centre the $p_\parallel$ distribution at $p_\parallel$=0 a.u. It should be noted that a systematic error arising from a small drift in laser intensity, ΔI_0, over the course of a measurement (i.e. 5 eV drift in U_p) also contributes to $p_\parallel$.

We investigate the uncertainty in U_p, and thus field strength, arising from U, $l_a, l_d, t_\mathrm{shift}, \Delta I_0$, by considering U_p as the following function, $f(U, l_a, l_d, t_\mathrm{shift}, \Delta I_0)$. We propagate the uncertainty in U_p using [155]

$$s_f = \sqrt{\frac{\partial f}{\partial x}^2 s_x^2 + \frac{\partial f}{\partial y}^2 s_y^2 + \frac{\partial f}{\partial z}^2 s_z^2 + \ldots} \tag{4.7}$$

where $\frac{\partial f}{\partial x}$ is the response of f, ∂f, to a small change in the parameter x in question, ∂x, whilst s_x is the standard deviation of x. The following standard deviations are used: s_U=10 V,$s_{\mathrm{l_a}}$=0.003 m, $s_{\mathrm{l_d}}$ =0.002 m,$s_{\Delta\mathrm{ToF}}$=0.5 ns, $s_{\Delta\mathrm{I_0}}$=0.1 W. The corresponding $\frac{\partial f}{\partial x}$ values and the standard deviation of f, s_f, are shown in the Table 4.5 below.

In summary, the calculated uncertainty is less than 10% compared with the measured field strength, which is shown as the horizontal error bar in Fig. 4.5.

Table 4.5: Error propagation values of field strength.

	2.5 V/Å	3.1 V/Å	3.4 V/Å	3.8 V/Å
$\frac{\partial f}{\partial U}(\frac{eV}{V})$	0.32	0.36	0.5	0.44
$\frac{\partial f}{\partial l_a}(\frac{eV}{m})$	950	300	50	100
$\frac{\partial f}{\partial l_d}(\frac{eV}{m})$	2000	1200	1077	1700
$\frac{\partial f}{\partial t_{\text{shift}}}(\frac{eV}{ns})$	9	12	9	17
$\frac{\partial f}{\partial \Delta I_0}(\frac{eV}{W})$	50	50	50	50
$s_f(eV)$	8.8	9.9	9.1	12.8

4.2.6 Mechanism of bond length stretch.

The mechanism explaining the distortion of the nuclear framework in H_2O^+ is as follows: The optical cycle 3.2 µm laser field of 10.7 fs couples in the electric dipole. The molecular dipole moment, µ, given by $\boldsymbol{\mu} = \sum_i Q_i \mathbf{r}_i$ consisting of the charge Q_i at the vector representing position $\mathbf{r}_i$ for the i_{th} atom [156]. When the laser field strength increases, it leads to stretching the O–H bond length further and slightly reducing the H-O-H bond angle, which increases the molecular dipole moment of water and becomes more polarized. The dipole moment of field-free H_2O^+ in its ground electronic state is 2.370 D[156]. As an increase in field strength from 2.5 to 3.8 V/Å, the increasing dipole moment of 8% – 33% of H_2O^+ is observed coincidently with internuclear stretching as compared to the field-free case.

4.3 Conclusion and outlook

We investigate the response of isolated water molecules to external fields of varying strength. Resolving a symmetrically stretched H_2O^+ structure in the ground electronic state 7 – 9 fs after ionization using LIED under the strong-field. By increasing the field strength from 2.5 V/Å to 3.8 V/Å, the O-H bond length, R_{OH}, rises from 1.138 ± 0.058 Å to 1.349 ± 0.067 Å, and the H-H internuclear distance increases from 1.915 ± 0.068 Å to 2.2 ± 0.163 Å, corresponding to 14%–35% (R_{OH}) and 17%–35% (R_{HH}) stretch to the equilibrium field-free H_2O^+ ground-state structure. This change was accompanied by an increase in the dipole moment of H_2O^+ from 2.554 D to 2.780 D. This is significantly higher than the field-free neutral H_2O and H_2O^+ cation values of 1.855 D [157] and 2.370 D [156, 158], respectively. The stronger coupling of the nuclear framework to the laser field ultimately leads to elongated O-H and H-H internuclear distances and a slight reduction of the H–O–H angle measured with picometre and femtosecond resolution. Resolving changes in the molecular structure with such precision is enabled by the LIED's capability to detect molecular interferences occurring between one oxygen and two hydrogen atoms in H_2O^+.

We note that a water molecule is solvation experiences an ambient electric field around 2V/Å, the same order as our field strength. The experimental observation provides insight into "liquid" water molecular distortion in nature. In that case, it may be possible to alter the structure of water molecules in solvation shells that typically surround proteins in cells. It provides the ability to impact the behaviour of proteins by modifying the water-protein electrostatic interaction using strong laser fields. The measure intermolecular and intramolecular bond distances cluster of water with LIED filed would be an exciting project.

Chapter 5

High density molecular jets of complex neutral organic molecules with Tesla valves

Contents

The study of large, isolated organic molecules in the gas phase is a standing challenge, given that these molecules typically exist either in the liquid or solid phase at room temperature and ambient pressure. The samples can be heated and introduced to an ultra-high vacuum environment which generates a gaseous sample, but their vapour pressure is still too low for measurement (below 1 mbar). Currently, no remedy exists to deliver dense molecular jets of neutral complex molecules without ionizing or exciting the target.

The present chapter presents a remedy based on a novel gas delivery system utilizing a series of micro-sized no-moving parts Tesla valves to generate molecular jets of neutral complex molecules. We prove the utility of the new gas delivery system on the strong-field ionization of cis-Stilbene molecules as a test case for complex organic molecules with a vapour pressure of less than 1 mbar. We achieve more than an order-of-magnitude increase in the molecular ion signal than any other method. We show that the ion signal was stable over a measurement time of more than 6 hours. This is a markable improvement over the otherwise short-lived ion signal of less than 15 minutes without Tesla valves. Flow simulations illustrate the principle of unidirectional flow with the Tesla to mitigate counter flow and clogging of the delivery nozzle, a typical problem. We believe that our simple but effective gas-delivery system will benefit a wide range of experiments since it will enable measurements on already-difficult-to-measure molecular samples with low vapour pressures In this chapter, we will present experimental results of cis-Stilbene signal with and without Tesla valves, characterizing the property of the ion signal with different helium carrier gas pressure and the laser power. The flow simulations provide detailed insight into the function of the tesla valve.

5.1 Introduction

A stable and adequate atomic or molecular beam is employed in a wide range in physics, chemistry also has a lesser extent in biology [159], such as ultracold and ultrafast experiments in the physics and beam surfaces interactions in the chemistry [160, 123]. In the laser-induced electron diffraction (LIED) measurement, a cold and dense atomic or molecular beam must be performed. In the reaction microscope (ReMi) setup Fig. 3.10, we pass the gas-phase molecules through a small orifice from a room temperature receptacle to an ultrahigh-vacuum (UHV) chamber. The beam's velocity is accelerated via the pressure gradient of chambers, decreasing the internal temperature to a few K regions due to the internal energy of the target beam (i.e. rotationally and vibrationally) converted to kinetic energy.

The main challenge is to deliver adequate and dense enough gas-phase beams to the interaction region. In the typical ReMi measurement which required around gas densities around 10^{10} - 10^{12} atoms/cm^3 [161, 162, 163]. It is easy to achieve simply as gas-phase molecules like O_2 or N_2 and liquid phase molecules possess higher vapour pressure as H_2O. However, lacking enough gas density always resists the research field progressed. Some interesting larger organic molecules typically existed as the liquid or solid phase at ambient and room temperatures possess relatively low vapour pressure.

A molecule such as a cis-Stilbene possesses lower vapour pressure which has been widely considered a model system to study isomerization dynamics, which has well-characterized cis and trans isomers. Exist numerous theoretical and simulation studies on the isomerization pathways of stilbene molecules. There is also enormous ensemble-averaged experimental studies based on probing the electronic and vibrational states using surface tip-enhanced Raman spectroscopy or atomic force microscopy, which give information about the yield and change in potential energy surfaces. However, no unambiguous identification of the isomerization pathways of the cis-trans geometrical structure of such molecules.

We have to consider a few efficient ways to produce gas-phase jets of large organic molecules, such as (i) heating the sample with an oven; (ii) decreasing the ambient pressure (connected to the UHV chamber); (iii)using a high flow rate carrier gas passing the reservoir, which picks up the vaporized sample ship to the reaction chamber. Here, we combine mentioned three ways using a temperature-controlled delivery system called ”bubbler” containing a liquid sample in a small reservoir shown in Fig. 3.10. The evaporated liquid sample can be mixed with the carrier gas. Next, they are transported to the interaction area to reach sufficient target density for measurement. We could also melt the sample to the liquid phase in case of the solid sample by heating the bubbler, succeeding in evaporating to a gas. The traditional bubbler set up well performance in the H_2O experiment (Chapter. 4), thanks to the higher vapour pressure of the water around 23 mbar at room temperature. However, simple like cis-Stilbene own a relatively low vapour pressure which is smaller than 1 mbar at room temperature [164]. Using a traditional bubbler to deliver cis-Stilbene could not reach the sufficient gas density in the interaction area, even with more than 1 bar carrier gas and heated bubbler more than 100 °C. Meantime overheating may lead to chemical degradation of cis-Stilbene must be avoided. The simple bubbler owns a subtle limitation that the flow of steam is not unidirectional, which can cause the target sample to be trapped around the delivery system and clogging of the nozzle; also, the speed of flow inside the bubble is inadequate.

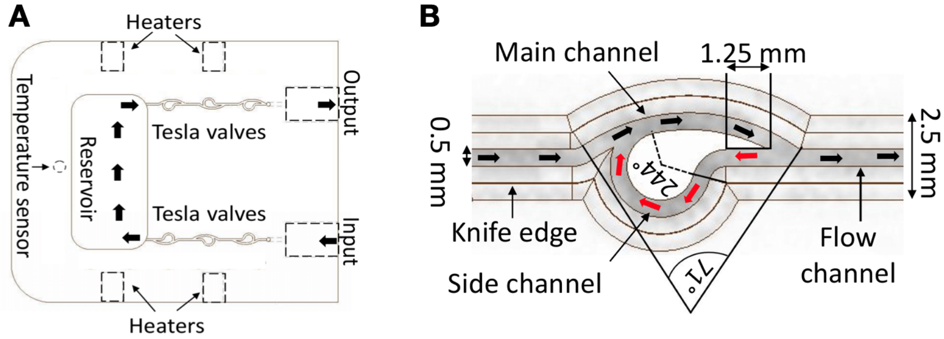

Figure 5.1: **Bubbler designs and operating principles.** **A** The rectangular flat bubbler is applied in this thesis with Tesla valves combined with a reservoir, 4 heaters, a temperature sensor, inlet and outlets. **B** Zoom-in view of one of the flow-control segment of the tesla valves. All the dimensions are indicated, black (red) arrows indicate the forward (backward) direction of gas flow.

It is crucial to improve the rate of evaporation of the cis-Stilbene to reach high gas density. Some factors influence the rate of evaporation, including (i) Flow rate of gas; (ii) The number of minerals dissolved in the liquid; (iii) Ambient pressure; (iv) Surface area; (v) Concentration of the substance evaporating in the air. To maximise the flow rate, we need to reduce the width of the channel inside the Tesla valves bubble to improve the flow speed, using pure carrier gas to pick up the relatively pure liquid sample contained by a larger surface reservoir while keeping the sample at a vacuum level environment.

Here, we present a novel gas delivery system utilising a series of micro-sized no-moving parts Tesla valves [165, 166, 167], to generate molecular jets of cis-Stilbene as shown in Fig. 5.1. Generated high-speed unidirectional flow leading to a significant improvement of gas density, the Tesla valve bubbler let detected cis-Stilbene ion signal boost an order-of-magnitude observed in our experimental set-up. The Tesla valve is a passive one-way valve with a fixed geometry to ensure a stream flows preferentially in one direction. The other direction will have tremendous resistance or even no flow.

The Tesla valve bubbler composes two tesla valve channels consisting of three flow-control segments and a relatively large horizontal flat reservoir. The Tesla valve is a pipeline with a more complicated flow-control segment consisting of alternating pipeline branch structures. Each flow-control segment is divided into two pipelines, one of which is slightly inclined, called the main channel, and the other is bent into a half ring called the side channel. Fig. 5.2A shows the flow passes the main channel and partially passes the

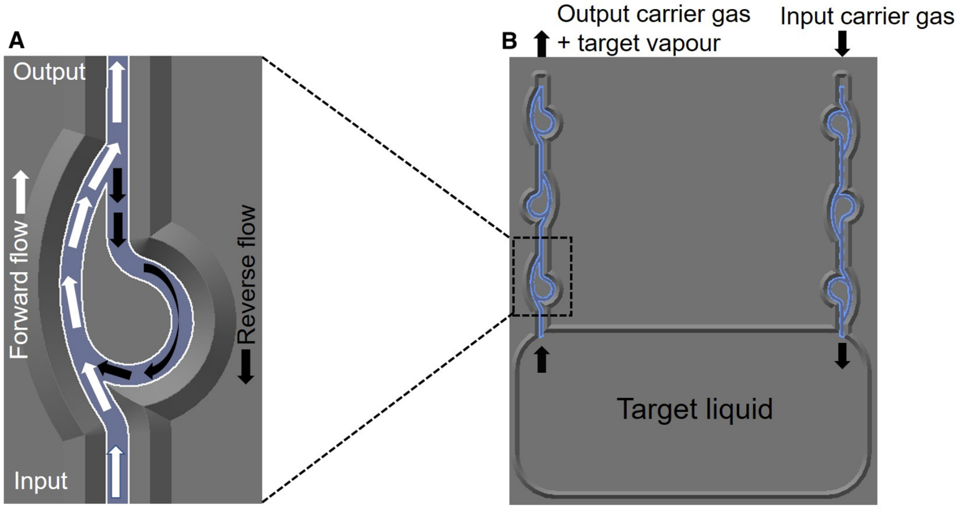

Figure 5.2: **Working principle of a Tesla valve.** **A** White and black arrows indicate the forward and the reverse flow, respectively. **B** Bubbler with the Tesla valves, where the channel of the valves are in shaded blue. The valves in the input line and the output line are arranged. There is an adequate unidirectional flow of carrier gas and efficient transport of the target vapour through the bubbler output.

side channel without resistance in the unimpeded/forward direction (from bottom to top). However, when the flow enters from the other direction (blocking/backward direction, from top to bottom), the liquid flowing in the side channel (annular branch) is turned around will collide head-on with the liquid on the main channel (inclined branch), hindering the flow of liquid. The fluid in the side channel turns around impedes the main channel's flow at a combination point, blocking the whole flow from up to down. After multiple branches, little liquid can flow out of the nozzle, and it can be controlled to prevent liquid from flowing out, thus acting as a check valve. The following series of the flow-control segment is the equivalent, and the number of the flow-control segment can be extended or decreased as needed, showing in Fig. 5.2B.

To augment the flow rate, the width of a channel inside Tesla valves bubble manufacture by only 500 µm; the reservoir designed by the horizontal and flat ensures the large surface area; the pure carrier gas He and 96% pure cis-Stilbene are utilised. The sample is directly exposed to an ultra-high vacuum to reduce the ambient pressure. We also heat the sample to 100 degrees to increase evaporation.

A parameter called diodicity, $\mathrm{D_i}$ often used to characterised the ratio of directional resistances. It defines as the ratio of pressure drops between backward (reverse) and forward directions.

$$D_i = \frac{\Delta p_r}{\Delta p_f} \tag{5.1}$$

Δp_r (Δp_f) is the pressure drop between two ends of the conduit of the reverse(forward) direction. $\mathrm{D_i}$ value larger than one indicating achieving a unidirectional flow. Telsa valve typical could achieve $\mathrm{D_i}$ value around 1.5 [168, 169, 170].

A further advantage is its fixed geometric shape, and it can make up for the deficiencies of traditional valves that are easily damaged due to the requirement for movable parts. The valve does not need any switches, has higher wear resistance, durability, and can be made of many materials.

5.2 Methodology

5.2.1 Bubbler with and without Tesla valves

Detected vertical (Y) position on the ion detector as a function of corresponding time-of-flight (ToF) measured with a Tesla valves bubbler at 1.5 – 1.6×10^{14} W/cm^2 laser intensity is shown in Fig. 5.3. The Y direction is parallel to the molecular jet direction. Due to gravity, the heavier fragments will fly longer and reach the lower position in the Y direction. The black dash line indicates the relationship between the Y position and the ToF of fragments. The red dash line exhibits the Y position of the cis-Stilbene ions signal. The repetition rate of the laser system is 160 kHz, the time interval between two laser shots is 6.25 µs, which is defined as a ToF window. We need to create three ToF windows to capture the cis-Stilbene ions signal, and the first two windows will also display the same signal, which are generated by the previous laser shot. The ionization potential (I_p) of the cis-Stilbene is 7.8 eV [171], which is relatively low compared with other liquid molecules like H_2O (12.6 eV). The relatively low I_p causes cis-Stilbene to be ionized easily to generate more fragments. In our measured ToF spectra, the two main signal original from the cis-Stilbene molecular ion (${C_{14}H_{12}}^+$; 15.5 µs) and Coulomb exploded fragments (e.g. ${C_7H_6}^+$ + ${C_7H_6}^+$; 11µs). The other fragments as C_5H_x and C_6H_x are also signed in the Y vs ToF figure.

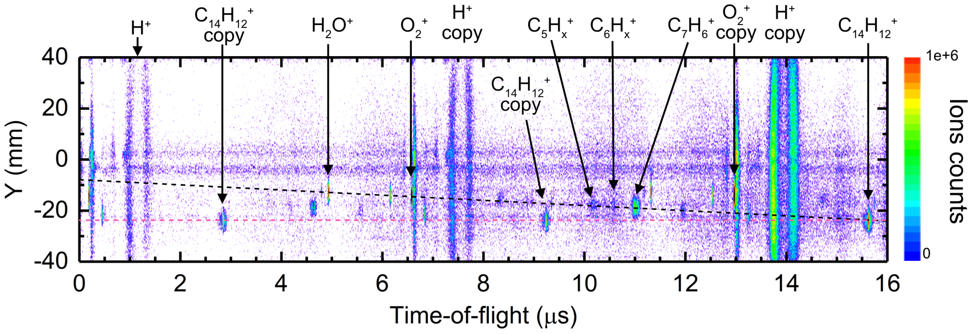

Figure 5.3: **Bubbler Y vs TOF.** Detected vertical (Y) position on the detector as a function of corresponding time-of-flight (ToF) measured with a Tesla valves bubbler. All interest ion species are identified and betokened. Due to gravity, the heavier fragments will fly longer and reach the lower position in the Y direction. The black dash line indicates the relationship between the Y position and the ToF of fragments. The red dash line exhibits the Y position of the cis-Stilbene ions signal. The signals that do not coincide on the diagonal dashed line are copied signals.

Figure 5.4 shows a comparison of the measured ToF spectra with (black line) and without (red line) Tesla valves following the same experimental condition. A zoom-in view of ToF spectra around 15.6 µs where $C_{14}H_{12}^+$ peak located shown in panel b). Using the Tesla valve, the proportion of the cis-Stilbene ion signal to the full spectrum was significantly enhanced by a portion of 6.5. In addition, we found that when the Tesla valve is used (not used), the cis-Stilbene molecular ion accounts for a 2.94% (0.45%) portion of all detected ion signals. While the contribution of $C_7H_6^+$ fragments are increased that reinforcing a higher gas density is approached. To be noticed, we also observe a higher contribution of cis-Stilbene ion signal with a bubble without Tesla valves appearing at the beginning of the experiment. However, it only lasts less than 5 minutes. We attribute it to the appearance of the signal from accumulated cis-Stilbene saturated vapour when the sample is placed longtime in the reservoir. When the system reaches the balance, there is insufficient accumulated cis-Stilbene vapour delivery to the vacuum chamber. In contrast, our Tesla valve bubbler can provide a stable high-density gas-phase molecular beam for more than six hours using only 1.5 ml of cis-Stilbene liquid sample.

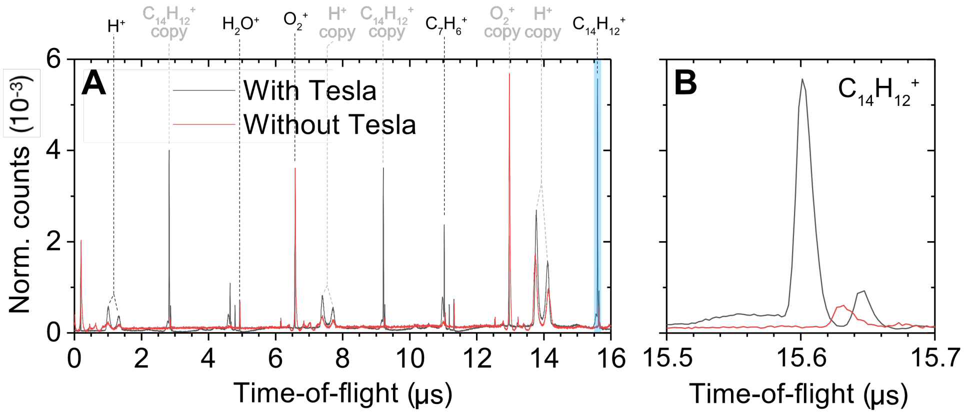

Figure 5.4: **Ion ToF spectra measure with and without Tesla valves.** **A** A comparison of the measured ToF spectra with (black line) and without (red line) Tesla valves following the same experimental condition. All ion species are betokened, and $C_{14}H_{12}^+$ peak range is highlight by the blue shadow area. **B** A zoom-in view of ToF spectra around 15.6 µs where $C_{14}H_{12}^+$ peak located. The slight peak shift in the ToF is due to the different electrostatic fields applied. Their respective total ion signal normalised each ion ToF spectra.

5.2.2 Tesla valve bubbler for different experimental conditions

The application of Tesla valves establishes a significant advantage over a simple bubbler. In this section, we systematically investigate the signal performance with different experimental conditions such as laser power and carrier gas pressure. We measured Tesla valve bubbler ion ToF spectra with laser power of 1.8W (black line) and 1.0W (red line). To achieve the maximum signal of the molecular ion of interest, we need a counterbalance between the total ions signal and the ratio of the cis-Stilbene signal.

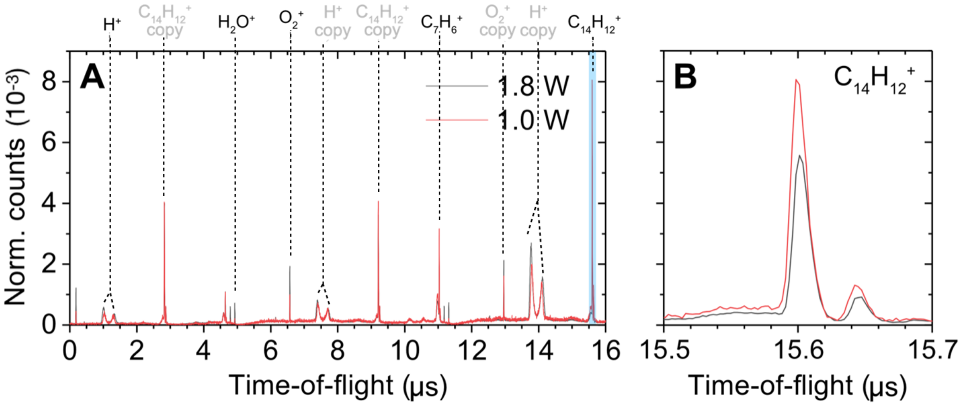

Figure 5.5: **Tesla bubbler signal dependence on laser intensity A** Ion ToF spectra were measured Tesla valve bubbler ion ToF spectra with laser power of 1.8W (black line) and 1.0W (red line). The ToF range of blue shaded indicate $C_{14}H_{12}^+$ peak domain. **B** Zoom-in view of the cis-Stilbene ion ($C_{14}H_{12}^+$) peak for the two ToF spectra respectively. Their respective total ion signal normalised each ion ToF spectra.

Higher laser power will generate a more appreciable ion signal for detection. In contrast, laser intensity requires to be kept at a minimum value to avoid fragmenting the molecule. We proved that by reducing the laser power from 1.8 W to a sufficient laser power (1.0 W). The observed $C_{14}H_{12}^+$ molecular ion signal estimated for a 32% increase in the proportion of the total detected ion signal (Fig. 5.5B). Fig 5.5A shows the ToF spectra normalised by the total counts with two laser intensities. The Grey (red) line presents the laser intensity with 1.8W (1.0W), and the blue shadow area indicates the cis-Stilbene ion ToF peak area. The low laser intensity data exhibits a higher cis-Stilbene signal ratio due to fewer fragments are produced.

The cis-Stilbene signal could be scaled up with laser intensity. However, empirically we need to retain the total ions signal lower than the 25% repetition rate. In an ideal case, our MCP detector could detect cis-Stilbene signals up to 160,000 counts per second (160 kHz repetition rate laser system). Nevertheless, the sizeable signals could not be detected coincidently due to the electronic coincidence gate condition. Three ion Tof windows are created due to the heavy mass, the electron ToF window (500 ns) and the electronic signal transfer also need to cost a few ns. So far, the electronic coincidence gate necessitates a response time of more than 20 μs (4 to 5 laser trigger intervals), i.e. count rate as 20% to 25 % laser repetition rate is acceptable for the coincident gate. Scaling up the laser intensity is not helpful for coincident detection. Meanwhile, lower laser intensity provides a higher ratio of contributed cis-Stilbene ions signal. Therefore we need to avoid too high laser power, reconcile it to meet the count rate around 25% repetition rate to achieve a maximum cis-Stilbene signal.

In the next step, we investigate the dependence of the ion signal from the helium carrier backing pressure under the same laser intensity. Figure 5.6 shows the normalised ToF spectra by total counts vary of backing pressure displayed amidst different colours. With increasing the backing pressure, all the fragments are simultaneously increased. The

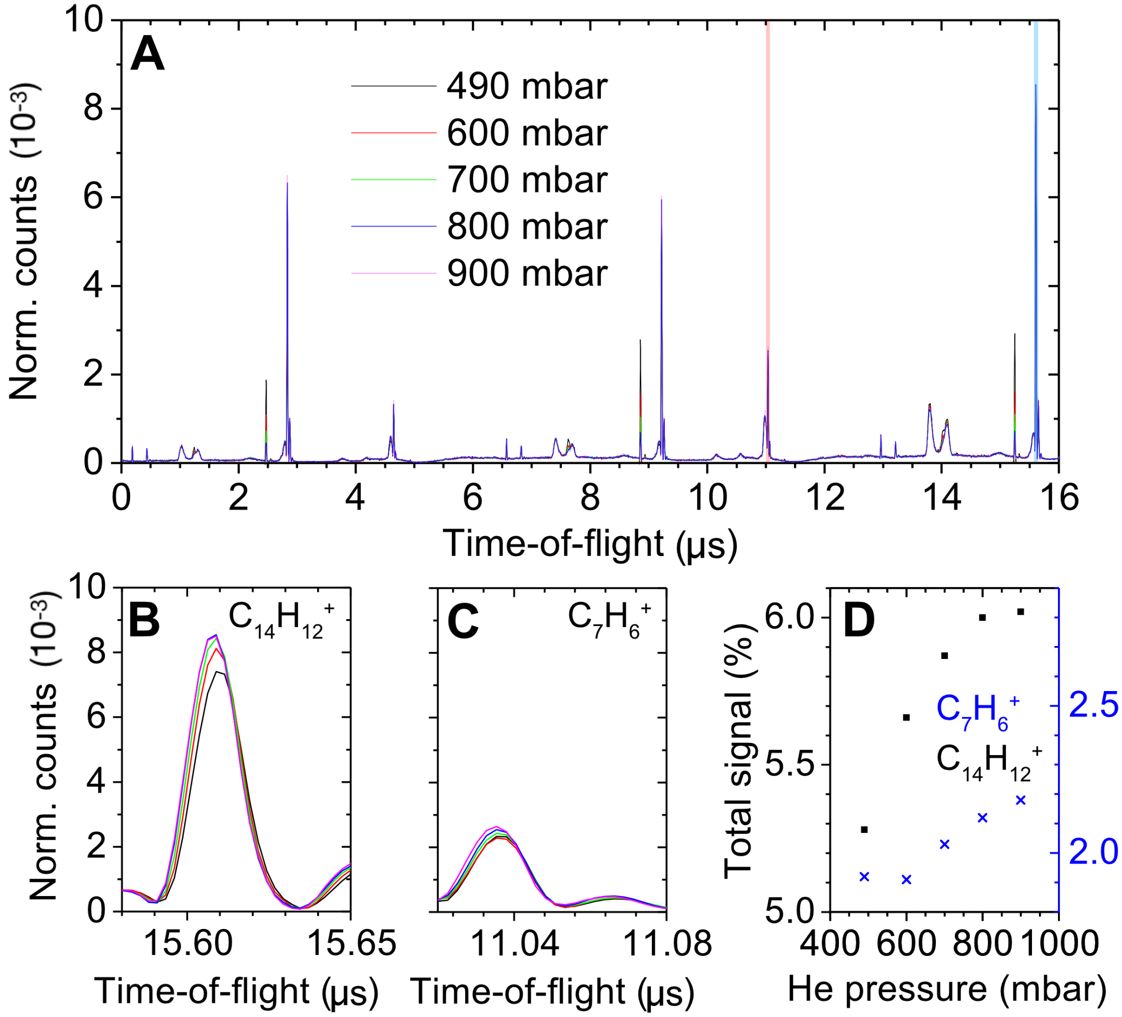

Figure 5.6: **Tesla bubbler signal dependence on the pressure of helium carrier gas.** Cis-Stilbene ion ToF spectra measured with 1.2 W laser intensity ranging a helium carrier gas backing pressure of 490 mbar (black), 600 mbar (red), 700 mbar (green), 800 mbar (blue), and 900 mbar (pink). (**A**) The whole ToF spectra are presented and blue (red) shaded indicate $C_{14}H_{12}^+$ ($C_7H_6^+$)peak region. Zoom-in view of the cis-Stilbene ion ($C_{14}H_{12}^+$) peak (**B**) and phenyl fragment ($C_8H_6^+$) ions peak (**C**) dependence on helium pressure. **D** The cis-Stilbene (black squares) and phenyl fragment (blue crosses) percentage signals function of different Helium backing pressure. Left black (right blue) Y-axis presents the total signal of cis-Stilbene (phenyl fragment). Each ToF spectra with different backing pressure are normalised by their corresponding total ion signal.

zoom-in view of $C_{14}H_{12}^+$ and $C_7H_6^+$ Tof peaks are shown in the Fig. 5.6 (b) and (c). It is easy to understand that higher backing pressure delivers a larger gas density. However, infinitely scaled up backing pressure will not improve the ion signal. We observed that when raising the helium pressure from 490 mbar to 900 mbar, the molecular ion signal increased by about 20%, as shown in Fig. 5.6 (d). From 490 mbar to 800 mbar, the ion signal increase linearly with backing pressure. After 800 mbar, the ion signal increases progressively, betokening that even if we rise higher backing pressure, the ion signal barely grows slightly.

5.2.3 Flow simulations of Tesla valve bubbler

We applied OpenFOAM (Open Source Field Operations and Operations) software [172] to simulate fluid dynamics for a bubbler setup handling a D-type Tesla valve with six flow control sections. We first extract the flow channel from a STEP-File (ISO 10303-21) [173], including all flow-control segments and reservoir, then mesh the entire channels. We are defining the input and output surfaces according to our design. For example, in Fig. 5.7B, we define the input gas pressure as 1 bar from the left channel and the output pressure as $1{\times}10^{-9}$ bar to the right channel. Utilize the semi-implicit method for calculating the pressure correlation equation (SIMPLE) to simulate incompressible gas dynamics. We chose the turbulence model as the Reynolds Average Navier-Stokes (RANS), the available model as $k - \omega$ SST and set the relative transport characteristics for the helium. Non-orthogonal correctors appended up to five to improve stability and convergence. The fluid simulation for tesla valve bubbler takes around 2 hours.

The simulated pressure and velocity two-dimensional (2D) distributions of tesla valve bubbler utilizing computational fluid dynamics (CFD) simulations are shown in Fig. 5.7. The velocity distribution is evolved at four different time steps is shown in Figure 5.7A. The helium carrier gas straightway fills two tesla-valve channels and then slightly reaches the reservoir's balance due to the pressure difference of the input and output surface set. The velocity distribution of the entire bubbler in balance is shown in Fig. 5.7B, and we also need to notice that the flow speed is faster to the sidewall and lessened in the middle of the reservoir. Figure 5.7C shows the pressure distribution of the entire bubbler, shows the constant pressure in the reservoir but higher grading descend in the tesla valve channels. The high-speed unidirectional carrier gas in the main channel ensures that it can pick up adequate vaporized target molecules and deliver higher target density to the interaction area.

Figure 5.8A shows the velocity simulation of flow passes three flow control segments of the tesla valve in an unimpeded forward direction, the colour bar from red to blue betokens the speed reduced with unite m/s. Zoom-in view of a flow control segment shown in Fig. 5.8B, the pointing of the white arrow symbolises the flow direction, the density of the white arrow betokens the amplitude of the speed. We could observe that the flow speed in the main channel is much faster than the side channel. The direction of flow exhibits a U-turn in the enter and exit of the side channel. The forward flow mainly moves in the main channel. The reverse flow mainly enters the side channel where obstructing flow from the forward direction forms more resistance.

In Fig. 5.8C, we set the opposite initial condition in the simulation to force the flow moving in the backward blocking direction (from bottom to top), the two channels barely has any speed. This is because flow moving in the side channel is turned around will conflict with the flow on the main channel performed the barely white arrow in Fig. 5.8D.

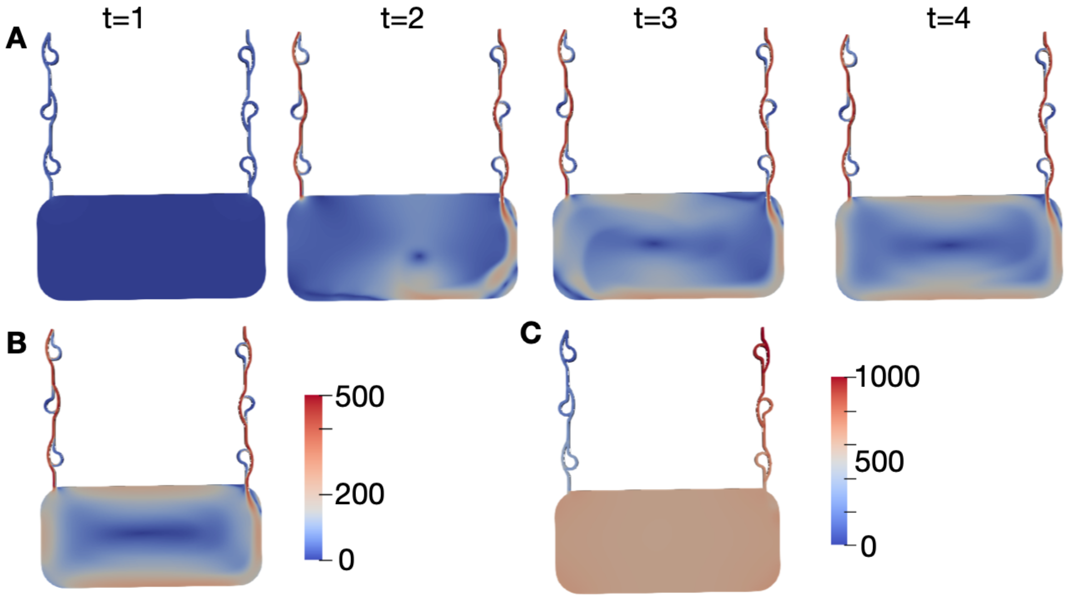

Figure 5.7: **Flow simulations of Tesla valve bubbler.** **A** The velocity distribution is evolved at four different time steps in time. **B** The velocity distribution of the entire bubbler in stability uniting m/s. **C** The pressure distribution of the entire bubbler in balance uniting mbar.

5.2.4 A new design

The flow preferably moving following the sidewall causes the velocity in the middle of the reservoir close to zero shown in Fig. 5.7B. The slight speed of carrier gas picks up less target liquid molecules meanwhile reducing vaporized efficiency. To solve the problems, we add small disturbers in the centre of a reservoir to maintain flow always passing the centre. Figure 5.9 shows the velocity distribution with four different time steps, respectively, observing the flow still survive in the centre of the reservoir due to the perturbation of the middle islands.

5.3 Conclusion and outlook

We demonstrate the efficiency of the new gas delivery system based on Tesla valves to produce a high density of gas-phase cis-Stilbene molecular jets. It accomplishes a comparatively long measurement time (> 6 hours) using only a 1.5ml liquid sample, making it possible to achieve strong-field ionisation measurements on such large and complex low vapour pressure molecules. We design a bubbler delivery system to maximise the evaporation of the target liquid sample, and the Tesla valve ensures that the vapour flows in one direction. The target sample will easily be stuck and positioned around the delivery system without the Tesla valve. Secondly, compared with the tesla valve's absence, we achieved an order of magnitude increase in the cis-Stilbene molecular ions portion to the total detected ion signal. This points to the possibility of achieving LIED measurement considering the measurement time and the signal-to-noise ratio of our cis-Stilbene sig-

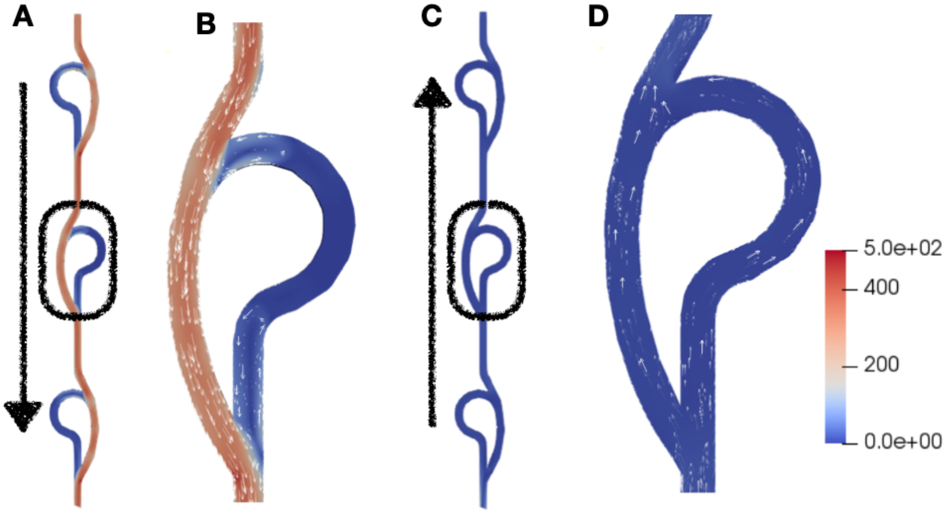

Figure 5.8: **Fluid dynamic simulation for the forward and backward flow of the Tesla valve.A** Flow passes the main channel and partially passes the side channel without resistance in the unimpeded forward direction (from top to bottom indicated by a black arrow). **B** Zoom-in view of the flow control segment, the pointing of the white arrow symbolises the flow direction, the density of the white arrow betokens the amplitude of the speed. **C** Flow simulation of the backward blocking direction (from bottom to top indicated by a black arrow) flow streaming in the side channel is turned around will collide head-on with the flow in the main channel, the entire channels barely has any speed. **D** Zoom-in view of the flow control segment contains barely a few white arrows intimating a lower speed of flow.

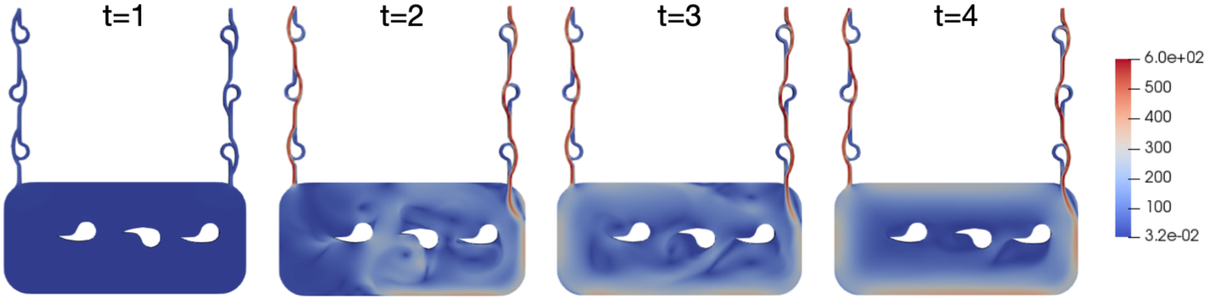

Figure 5.9: **New designof Tesla valve bubbler.** The velocity distribution is evolved at four different time steps in time. Added small disturbers in the centre of a reservoir causes the flow to be unsteady, maintaining flow passing the centre.

nal. We systematically examined the experimental conditions that affect the Tesla valve bubbler's ion signal, such as laser power, carrier gas backing pressure and reservoir temperature. We show that the molecular ion signal can be maximised by measuring under the following conditions: (i) relatively low peak laser intensity; (ii) high helium back pressure; (iii) high reservoir temperature. Our flow simulation quantitatively illustrates the working principle and the velocity and pressure distribution of the Tesla valve bubbler. Confirm the speedy and one-way airflow induced by the Tesla valve.

We believe that our simple but effective gas-delivery system will benefit a wide range of ultra-cold and ultra-fast experiments since it will enable measurements on already difficult-to-measure molecular samples with low vapour pressures. The Tesla valve bubbler will become an essential key as a gas delivery system for the future LIED time-resolved pump-probe measurement of more prominent and complex molecules (such as stilbene and azobenzene).

Chapter 6

Machine learning based laser-induced electron diffraction imaging of molecular structures

Research at the intersection of physics and machine learning (ML) has provided many spectacular advances due to the capacity to solve complex problems with advanced numerical algorithms. Laser-induced electron diffraction (LIED) imaging presents a complex problem since retrieving nuclear coordinates requires equates to finding the global minimum in a complex multi-dimensional solution landscape. This chapter presents a remedy based on a specific implementation of a convolutional neural network (CNN). The solution is based on a pre-calculated and sufficiently large ensemble of structural solutions, which the neural network can identify as matching the measured structure. The method overcomes the above-stated convergence issues and is shown to predict three-dimensional (3D) accurately molecular structures measured with LIED. We contrast these findings against several previously measured structures and all are retrieved with the highest fidelity through the ML framework. Outlining, we present a new approach to overcome scaling issues in image retrieval that impede further advances in ultrafast structural dynamics research and impact the larger area of diffracting imaging. The method is scalable to complex and large molecular structures and overcomes present scaling issues of multi-peak fitting and search routines in high-dimensional solution spaces. Our implementation of CNN for diffraction imaging is shown to retrieve molecular structures accurately and is applicable to scattering or diffraction imaging, independent of the exact implementation with X-rays or electrons.

6.1 Linear regression

Before going into detail in machine learning or deep neural networks, let us first understand one of the simplest models: Linear regression. Regression is used for predictive analysis and forecasting to find the relationship between variables. For example, we have two sets of the independent variable input (x) and dependent output (y). The goal is to let the machine figure out the relationship between x and y. We first introduce a standard term generally used in machine learning called hypothesis (h). The hypothesis is a predicted function mapping out the x to y, and it can be interpreted as a machine trying to predict values (as much as close to y) from x. We will start with the example that y is comprised of a linear combination of x, represented by a linear regression model. In the end, we will build more complex models and learning algorithms.

The hypothesis of the simplest linear regression model with two parameters θ_0 (bias or intercept) and θ_1 (the slope) is expressed as:

$$h_\theta(x) = \theta_1 x + \theta_0 \tag{6.1}$$

In ML, the cost function defines how deviation the model performs to estimate the relationship between x and y, which is the difference or distance between hypothesis (h; predicted value) and actual variable (y). It helps us figure out the best configuration for parameters θ_0 and θ_1, providing the best fit for the predicted value (h) and expect or actual value (y). Cost Function also quantifies the predicted error of h and y in the way of a single exact number. The Cost Function is given by:

$$J(\theta_0, \theta_1) = \frac{1}{2m} \sum_{\mathrm{i}=1}^{m} (h_\theta(x^{(i)}) - y^{(i)})^2 \tag{6.2}$$

Where m indicates the number of data points, the cost function $J(\theta)$ only functions as parameters θ_0 and θ_1 and independent as variables x and y. In order to diminish the cost function or the deviation between the predicted and actual value, we usually use an optimization method called gradient descent, the most commonly used optimization algorithm for deep learning models training. The working principle is to use an iterations method to approach the global minimum of the target function. The gradient is the fastest rising direction. If we want to minimize $J(\theta)$, we drive the $J(\theta)$ following the opposite direction of the gradient, step by step repeatedly, to achieve the fast drop of the cost function.

The gradient descent algorithm is conceptually defined as:

$$\theta_{\mathrm{j}+1} := \theta_j - \alpha \frac{\partial}{\partial \theta_j} J(\theta_j) \tag{6.3}$$

Gradient descent is an iteration algorithm that minimizes the cost function and simultaneously optimizes all parameters of the ML model. The j_{th} is the index of the iteration number, the $J(\theta_j)$ is related on θ at j_{th} iteration, α is called learning rate define the step size of each iteration. The idea is that we start from randomly initialized parameters θ, all parameters are renewed simultaneously via gradient descent optimization in each iteration until the cost function reaches the global minimum.

Let us consider an intuitive explanation of gradient descent: Imagine a person is trapped on the top of a mountain and needs to go down, but the fog disorients him. Therefore, the path down to the downhill cannot be determined, and he must use the information around him to find the path to go down. At this time, he can use the gradient descent algorithm for help. Specifically, based on his current position, taking a step down following the steepest direction from the current position, pointing to solve the current position's gradient and taking a step down following the contradictory direction of the gradient. Then reach the next position and take a step down along the steepest direction repeatedly until the foot of the mountain. An Illusion of linear regression via gradient descent is shown in Fig. 6.1. It shows the dependent variable (y) as the independent variable (x) function in cross scatters. The hypnosis is randomly initialized at the beginning ($\theta_1 = 0$) presented by the solid blue line. Meanwhile, the Fig. 6.1b shows the corresponding cost function with θ_1 in same color. The hypnosis approaches the x-y function during five iterations, and the cost function's value decreases.

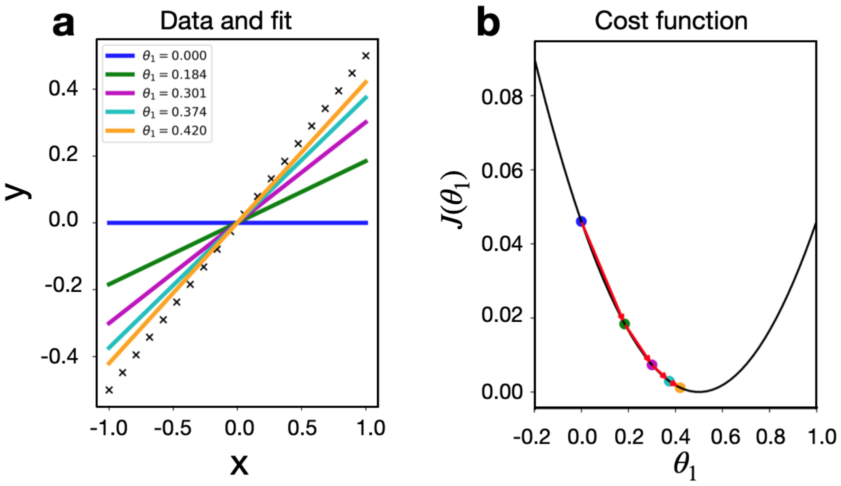

Figure 6.1: **Illusion of linear regression.** **(a)** The dependent variable (y) as a function of the independent variable (x) is shown in cross scatters, the hypnosis presented by the different colours of solid line with five iterations. **(b)** The cost function as function of the parameter θ_1. solid dots show the calculated cost function with correspondence colour in panel (a) with five iterations. θ_1 is initialised as zero initially, from blue to yellow as the iteration number increases, the hypnosis is closing to the variable (y), and the cost function is reduced.

6.1.1 Non-linear regression

To Illusate the complex non-linear relation between x and y, we present two variables x_1 and x_2 considering a second-order term non-linear model to describe the relationship such as:

$$h_\theta(x) = g(\theta_0 + \theta_0 x_1 + \theta_2 x_2 + \theta_3 x_1 x_2 + \theta_4 x_1^2 + \theta_5 x_2^2) \tag{6.4}$$

The equation contains six terms, including three second-order terms, two first-order terms and one bias. However, the number of terms gradually increases with the number of variables x_n, the number of quadratic terms grows in the order of $(n^2)/2$. Now suppose to include third-order terms such as $x_1^2 x_2, x_1 x_2^2$, and the number of cubic terms increases in the order of n^3. When n=100, it can be calculated and get about 17000 cubic terms. The number of these higher-order polynomial terms increase dramatically with the number of initial variable x_n, and the feature space will also expand sharply. Therefore, higher-order terms are required to describe complicated relations, in contrast, it is challenging to include them, and too many terms are likely to lead to over-fitting the result. In addition, there is also a problem of excessive calculation when dealing with so many items.

Hence, simply adding quadratic or cubic terms in the logistic regression algorithm is not a good way to solve complex nonlinear problems. For many practical machine learning and physical problems, the number of x_n is enormous, which will produce many feature items. Instead of create the model ”widely” (high order terms), we could make the algorithm ”deeper” (low order terms but many interconnected units). The neural network has proved to be a much better algorithm for solving complex nonlinear problems. Even if the input feature space or the input dimension n is vast, it can be easily solved. The neural network is based on a nonlinear, adaptive information processing system composed of many interconnected processing units. It has successfully solved many practical problems that modern computers are difficult to solve.

6.2 Neural networks

Historically, scientists have always hoped to simulate the human brain and create machines that can conceive: ”Why can people think?” Scientists have discovered that the reason lies in the human body’s neural network. We should not use an over analogy between neural networks and the human brain. The neural networks are only designed to solve machine learning problems rather than accurately portray the human brain.

Neural networks gradually emerged and were widely used in the 1980s and 1990s [174, 175, 176, 177, 178, 179, 180] and their applications declined in the late 1990s due to various reasons. Recently, neural networks have made a revival. One of the reasons is that neural networks are computationally expensive algorithms. The speed of computers has become faster in recent years, which is enough actually to run large-scale neural networks [181, 182].

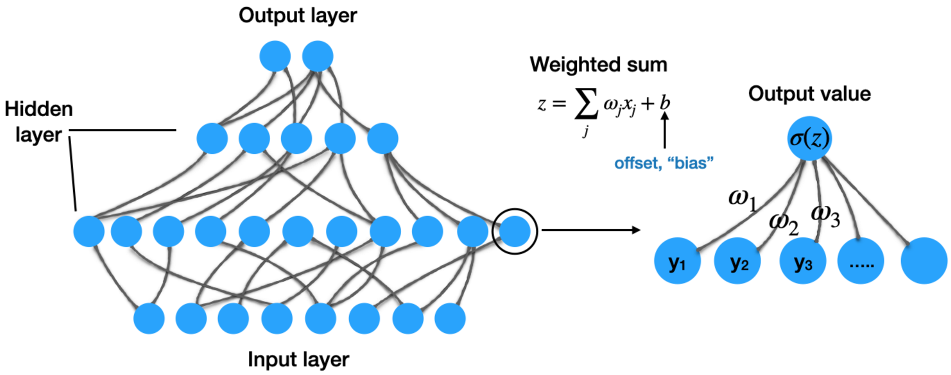

Figure 6.2: **A architecture of common multilayer neural network.** **(a)** A common multilayer neural network consists of three parts: input layer, hidden layer and output layer. **(b)** A zoom in view for calculation of one of neutron in the hidden layer

As shown in Fig. 6.2, a standard multilayer neural network consists of three parts:

input layer, hidden layer and output layer. Numerous neurons accept many non-linear input messages (input vector). The input messages are transmitted, analysed, and weighed in neuron links to form output results in hidden layers. The output message is produced in the output layer. The hidden layer is comprised of many neurons and links between the input and the output layers, which can possess one or more layers. The number of nodes (neurons) in the hidden layer is changeable, but the larger the number, the more significant the nonlinearity of the neural network, and the more significant the robustness of the neural network. We start the calculation from the input layer, and the value is interpreted in the hidden layer. The final value is stored in the output layer.

Like the human brain, the neuron network from information processing establishes a straightforward model and composes different networks according to different connection methods. A neural network is a computing model composed of many nodes (or neurons) connected. A neuron is the basic unit of a neural network representing a specific producing function, called an activation function. Each connection between two neurons represents a weighted value for the signal passing through the connection, called a weight, which is equivalent to the memory of an artificial neural network. The network's output depends on the connection method of the network, the weight value and the activation function.

The mathematical principle behind the neural network is called the Kolmogorov-Arnold representation theorem [183, 184] and is a partial answer to Hilbert's 13th question. A finite number of unary functions can superimpose any continuous multivariate function. The superposition of two finite unary functions is enough to represent any multivariate function accurately. This is much more powerful than a polynomial approximation. Using polynomials to represent a continuous multivariate function accurately requires infinite polynomials.

6.2.1 Weights and bias

Various factors are rarely equally important: some are decisive factors, while others are secondary. Therefore, we need to assign weights to these factors to represent their different importance. The weight characterizes the strength of the connection between different units. If the weight from neuron 1 to neuron 2 has a larger magnitude, neuron 1 has a more significant influence on neuron 2. Weight close to 0 means that varying the input value will not alter the output. The weights determine the influence of the input on the output.

The bias can also be called the intercept (offset) in the linear equation and move the activation function to the left or right. Bias is an additional input to the neuron. It ensures that when all inputs are 0, there is still a value to pass an activation function in the neuron.

$$z = \sum_j \omega_j x_j + b, \tag{6.5}$$

where ω is the weight, b presents the bias and subscript j offers layer index. The output z equals the weighted sum from the last layers plus a bias.

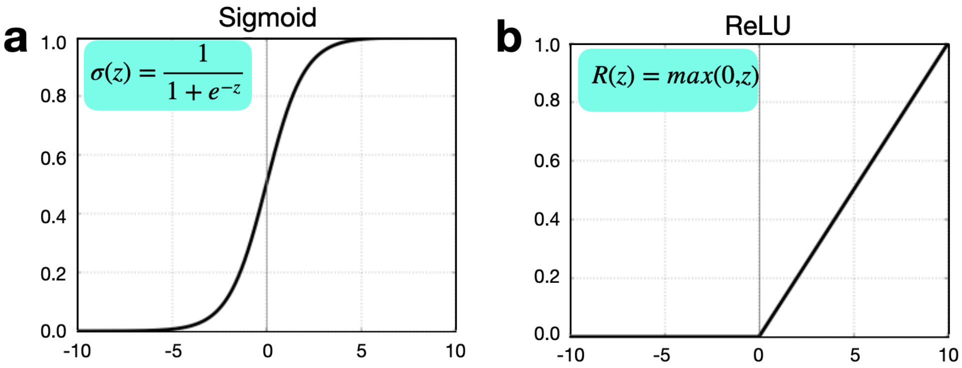

Figure 6.3: **Sigmoid function and rectified linear unit (ReLU). (a)** The effect of $\sigma(z)$ is similar to a "compression function", which compresses the range of previously unbounded output from 0 to 1. Conversely, when z towards positive number, e^{-z} approaches 0 and$\sigma(-z)$ approaches 1 at this time. **(b)** ReLU will pass all positive values but will change all negative values to 0. Relu will make the output of some neurons be 0, which causes the sparsity of the network and reduces the interdependence of parameters, alleviating the occurrence of over-fitting problems.

6.2.2 Activation function

In artificial and biological neural networks, a neuron produces more than the sum of input value it receives. A step inside is similar to the ratio of the action potential to the brain, called the activation function. The activation function accepts the previous weighted sum as input, then reforms it before the final output. The activation function is responsible for introducing nonlinear features to the neural network also required almost differentiable everywhere. Many activation functions have been proposed. Here, we will only describe two famous functions in detail: sigmoid and ReLU.

The sigmoid function is the oldest and most popular activation function. Its definition is:

$$\sigma(x) = \frac{1}{1+e^{-z}} \tag{6.6}$$

The variable z equals the weighted sum of the last layers then is assigned as an input to the sigmoid function. The advantage of the sigmoid is that the output range is limited, avoiding data diverges in transmission. The corresponding weaknesses are that its derivative is close to 0 when z is a relatively large positive or small negative value.

The sigmoid function may seem complicated and arbitrary, but it has an effortless shape when we plotted it as a function of z in Fig. 6.3.

We can see that the effect of $\sigma(z)$ is similar to a "compression function", which compresses the range of previously unbounded output from 0 to 1. When z= 0, $\sigma(0)$ is equal to 1/2. When z is extensive to negative , e^{z} in the denominator increases exponentially, and $\sigma(z)$ approaches 0. Conversely, when z towards positive number, e^{-z} approaches 0 and$\sigma(-z)$ approaches 1 at this time. The sigmoid function is continuously differentiable and quite simple, $\sigma(z)' = \sigma(z)(1-\sigma(z))$. We will use its differential in the later section.

Another activation function is the rectified linear unit (ReLU). Its definition is:

$$\sigma(z) = max(0, z), \tag{6.7}$$

ReLU will pass all positive values as they are, but will change all negative values to 0. Relu will make the output of some neurons be 0, which causes the sparsity of the network and reduces the interdependence of parameters, alleviating the occurrence of over-fitting problems. A sigmoid function or a ReLu function are commonly chosen. We could also use other functions depending on the model required.

6.2.3 Forward propagation

Forward propagation is the process of feeding the input value to the neural network and obtaining an output called the predicted value. Sometimes we also call a feedforward neural network. We feed the input value to the first layer of the neural network, where does not perform any operations. The second layer receives the value of the first layer, performs multiplication and activation function, and then passes it to the next layer. The subsequent layers repeat the same process as the second layer. Ultimately, we get the output value from the last layer.

We establish a neural network to accomplish a logical OR gate to understand how the neural network works. OR gate is a logic gate that realizes logical OR in digital logic, and its function is shown in the Table. 6.1. As long as at least one of the two inputs is high (1), the output is high (1); if both inputs are low (0), the output is low (0). This small neural network contains two layers and four neurons as Fig. 6.4 to realize OR gate. The input layer contains variables X_1, X_2 and one bias (b) totally three neurons. We involve the active function as $\sigma(z)$, which includes a non-linear connection in this simple case. The weight values are easily achieved according to the logic of the OR gate. Eq. 6.8 explain the detail of the forward propagation computation process.

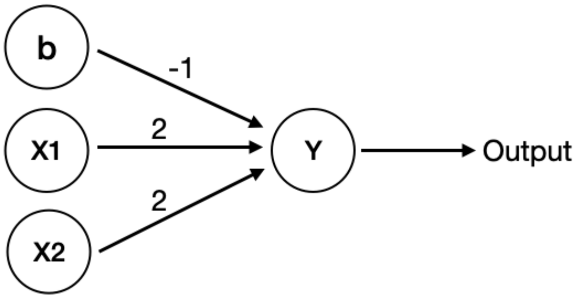

Figure 6.4: OR gate Neural networks.

X1	X2	Output
0	0	0
0	1	1
1	0	1
1	1	1

Table 6.1: OR gate

$$\begin{gathered} Y = \sigma(2X_1 + 2X_2 - 1) \\ \sigma(z) \begin{cases} Y = 1, & z > 0, \\ Y = 0, & z \leq 0, \end{cases} \end{gathered} \tag{6.8}$$

The above example is one of the most straightforward cases, only considering two layers. Next, we go through a standard neural network that contains three layers (input layer, hidden layer and output layer) shown in Fig. 6.5. Where x_1, x_2 and x_3 present the input value, subscript shows the index of an input value. $\omega_{\mathrm{ji}}^{(k)}$ present the weight between each neuron, subscript j and i indicate the neuron index for subsequent layer and current layer. The superscript presents the layer index. The b^k shows the bias or offset of the k_{th} layer, some people also named b^k as x_0^k. The mid product $Z_i^{(k+1)}$ is the linear combination of multiply weights plus a bias, which is input to the active function $\sigma()$ and producing the neuron value of sequence layer $a_i^{(k+1)}$. The computational process combines a linear function and a non-linear function.

Meanwhile, $a_i^{(2)}$ is the output of the first layer also the second layer's input. Then the same procedure is repeated from the second layer to the third until it reaches the final layer. In this thesis, the superscript generally presents the layer index, and the subscript shows the neuron index.

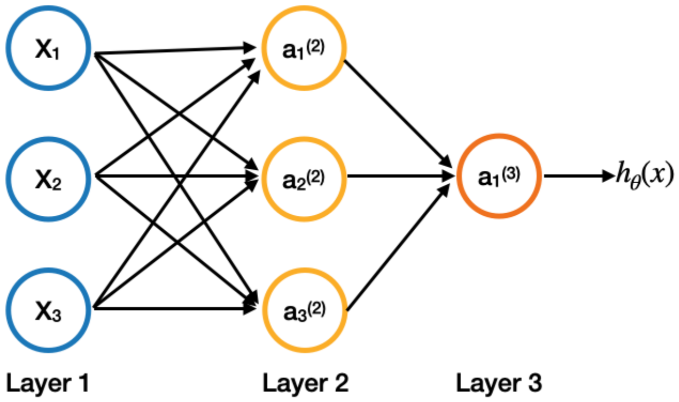

Figure 6.5: **Forward propagation.** The process of obtaining an output through layers of neurons from the input of the neural network (including operations such as weighted summation, bias addition, activation function).

$$Z_1^{(2)} = \sum_i \omega_{\mathrm{i}} x_i + b_i = \omega_{11}^{(1)} x_1 + \omega_{12}^{(1)} x_2 + \omega_{13}^{(1)} x_3 + b^{(1)} \tag{6.9}$$

$$a_1^{(2)} = \sigma(Z_1^{(2)}) \tag{6.10}$$

$$Z_2^{(2)} = \sum_i \omega_{\mathrm{i}} x_i + b_i = \omega_{21}^{(1)} x_1 + \omega_{22}^{(1)} x_2 + \omega_{23}^{(1)} x_3 + b^{(1)} \tag{6.11}$$

$$a_2^{(2)} = \sigma(Z_2^{(2)}) \tag{6.12}$$

$$Z_3^{(2)} = \sum_i \omega_{\mathrm{i}} x_i + b_i = \omega_{31}^{(1)} x_1 + \omega_{32}^{(1)} x_2 + \omega_{33}^{(1)} x_3 + b^{(1)} \tag{6.13}$$

$$a_3^{(2)} = \sigma(Z_3^{(2)}) \tag{6.14}$$

$$Z_1^{(3)} = \omega_{11}^{(2)} a_1^{(2)} + \omega_{22}^{(2)} a_2^{(2)} + \omega_{23}^{(2)} a_3^{(2)} + b^{(2)} \tag{6.15}$$

$$a_1^{(3)} = \sigma(Z_1^{(3)}) \tag{6.16}$$

These equations show the forward propagation process from input to output layers in a three-layer network, and the complex problems require more hidden layers within the same framework.

We could also visualise process from $\mathrm{L_{th}}$ -1 layer to the $\mathrm{L_{th}}$ via matrix elements, assuming in the $\mathrm{l_{th}}$ layer contains of k neurons and layer $\mathrm{L_{th}}$ -1 consist of n neurons, the output matrix a^l is expressed as matrix elements as:

$$\begin{bmatrix} a_0^l \\ \vdots \\ a_k^l \end{bmatrix} = \sigma \left(\begin{bmatrix} \omega_{0,0} & \cdots & \omega_{0,\mathrm{n}} \\ \vdots & \ddots & \vdots \\ \omega_{0,0} & \cdots & \omega_{\mathrm{k,n}} \end{bmatrix} \begin{bmatrix} a_0^{l-1} \\ \vdots \\ a_k^{l-1} \end{bmatrix} + \begin{bmatrix} b_0 \\ \vdots \\ b_k \end{bmatrix} \right) \tag{6.17}$$

After the computation of the forward propagation, the final output value is prognosticated by the neural network, called the predicted value. Then, we calculate a cost function, the same way as a linear regression, which is the deviation between the predicted and actual values. In order to decrease the value of the cost function and optimise the neural network model, we need the backpropagation algorithm by calculating the derivative of each neuron's weight.

6.2.4 Backpropagation

Backpropagation is a standard optimization algorithm together with gradient descent to train artificial neural networks. It calculates the partial derivative of the cost function to the weight of each neuron. Then, gradient descent is fed back to the optimization method to minimize the cost function by renewing the weights.

$$\frac{\partial J}{\partial \omega^{(l)}} = \frac{\partial J}{\partial a^{(L)}} \frac{\partial a^{(L)}}{\partial Z^{(L)}} \frac{\partial Z^{(L)}}{\partial a^{(L-1)}} \frac{\partial a^{(L-1)}}{\partial Z^{(L-1)}} \frac{\partial Z^{(L-1)}}{\partial a^{(L-2)}} \cdots \frac{\partial a^{(l)}}{\partial Z^{(l)}} \frac{\partial Z^{(l)}}{\partial \omega^{(l)}} \tag{6.18}$$

It uses the chain rule as Eq. 6.18 to calculate the partial derivative of the cost function to the weight in layer (l), and L presents the number of the total layer. We first calculate the derivative of the cost function in the last layer. We then use these values to calculate the derivative of the penultimate layer and repeat this process until the $\mathrm{l_{th}}$ layer. It calculates the partial derivative of the cost function to each weight from the last layer up to the first. Then same as linear regression, we subtract the derivative (gradient) of weight from the current weight value to get a new weight in each iteration. Unlike the simple linear regression method, it implements gradient descent to all neurons via differential calculus rather than only one parameter (θ_1). In this way, we are constantly approaching the local minimum. The detail of the calculation to calculate partial derivative is shown as:

$$\frac{\partial J}{\partial \omega^l_{\mathrm{ji}}} = a_i^{(l-1)} \sigma'(z_j^{(l)}) \frac{\partial J}{\partial a_j^{(l)}}, \tag{6.19}$$

with:

$$\frac{\partial J}{\partial a_j^{(l)}} = \begin{pmatrix} \sum_{\mathrm{j}=0}^{n_{l+1}-1} \omega_{\mathrm{ji}}^{(l+1)} \sigma'(z_j^{(l+1)}) \frac{\partial J}{\partial a_j^{(l+1)}} \\ \text{or} \\ 2(a_j^{(L)} - y_j) \end{pmatrix} \tag{6.20}$$

After obtaining the derivatives of weight, we obtain the new optimized weights via the gradient descent algorithm:

$$\omega_{\mathrm{ji}+1}^{l} := \omega_{\mathrm{ji}}^{l} - \alpha \frac{\partial}{\partial \omega_{\mathrm{ji}}^{l}} J \tag{6.21}$$

where J is the cost function, n_l is the number of neurons in the l_{th} layer, L is the total layer number and l is the index of layer, $\sigma'()$ is the derivative of the active function.

6.2.5 Supervised and unsupervised learning

Machine learning could classify as supervised or unsupervised learning. A supervised learning scenario uses a sample of a known category (labelled sample, the corresponding category is known) to prepare an optimal model, then uses the trained model to map unknown inputs to achieve the required output performance. In summary, the machine is enlightened with a part of the known classification and labelled samples. It uses the learned features to classify and label the unclassified and unlabeled samples. The classification and regression methods are commonly chosen in supervised machine learning. The classification method is generally used to divide various things into discrete predictions, such as facial recognition and crystal determination. The regression method is used to predict continuous, specific values.

Unsupervised learning is training on unmarked samples. It is essentially a statistical method that can discover some potential joints in unlabeled data. Such as clustering, the machine will try to put the things with high similarities together.

The difference between the above two is that supervised learning uses labelled sample sets, while unsupervised learning applies only to unlabeled sample sets. There are also mixed ways of learning called semi-supervised learning. It could be training with two sample sets, one is labelled, and the other is unlabeled. A combination of labelled and unlabeled samples generates a suitable model.

6.2.6 Convolutional Neural Network

Convolutional Neural Network (CNN) is a feed-forward artificial neural network. Its artificial neurons can respond to a part of the surrounding units in the coverage area and have excellent performance in image processing. A convolutional neural network consists of convolutional layers and fully connected layers. This structure enables convolutional neural networks to use the input data's two-dimensional structure or higher dimension. Compared with other deep learning architecture, convolutional neural networks can give better image and speech recognition results. It can also be optimised with backpropagation algorithms. CNN needs to consider fewer parameters, making it an attractive deep learning structure.

CNN has become a research hotspot in the field of speech analysis and image recognition. Its weight-sharing network structure makes it more similar to a biological neural network, reducing the complexity and weights of the network model. This advantage is more pronounced when the input of the network is a multi-dimensional image. The image can be directly used as the network's input, avoiding the complicated feature extraction and data reconstruction process in traditional recognition algorithms. In the fully-linked neural network architecture, neurons can form connections in the lower and upper layers, expanding the number of parameters. For example, for a 1000*1000 pixel image, ten fully-connected neurons in the first hidden layer will have 10^7 weights. However, not all neurons in the output and input layers need to be connected in CNN, but through the ”convolution kernel” as an intermediary. The same convolution kernel is shared in all images, and the image still retains the original positional relationship after the convolution operation. The parameters from the image input layer to the hidden layer mainly depend on kernel size and instantly lessened a few orders. A CNN is a multi-layer perceptron specially designed to recognise two-dimensional shapes. This network structure is highly invariant to translation, scaling, tilt, or other forms of deformation.

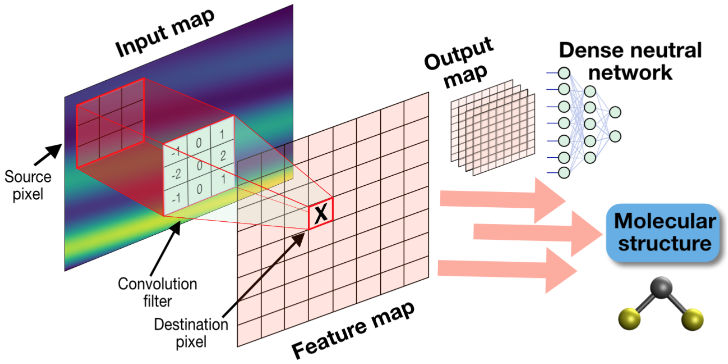

Figure 6.6: **Schematic of convolutional neural network (CNN) process.** The CNN uses a filter (white 3x3 grid) to extract features from the source pixel of the input map (see 3x3 grid) to generate a destination pixel. The feature map is generated by the filter convolved across every source pixel of the input map. Various types of filters are used that generate a collection of features maps that are then passed through fully connected dense layers to reach the output layer, which ultimately provides the predicted molecular structure.

CNN is essentially an input-to-output mapping, which can learn many mapping relationships between input and output without requiring any precise mathematical expressions. The advantage is that the weight sharing strategy reduces the parameters that need to be trained. The exact weight allows the filters to detect the characteristics of the signal without being affected by the position of the signal, making the trained model more effective in generalisation; meanwhile, pooling can reduce the network.

Other neural networks commonly employed in physics includes Recurrent neural network (RNN) and Generative Adversarial Network (GAN). RNN can handle long-term time correlation and description of dynamic time behaviour combining different Long Short-Term Memories (LSTMs). RNN transfers the time sequence data in its network cyclically to accept a broader range of time series structure input. GAN is an unsupervised learning method that lets two neural networks contest against each other. It is composed of a generative network and a discriminant network. The generation network is randomly sampled from the latent space as input, and its output results need to imitate the training set samples fully. The discriminant network is to distinguish the output of the generating network is actual or not. The generation network wants to deceive the discrimination network as much as possible. The two networks confront each other and constantly adjust their parameters. The ultimate goal is to make the discriminating network unable to judge whether the output of the generated network is accurate. GAN is often used to generate fake and natural pictures and movies, reducing the data's noise.

6.3 ML-LIED

It is challenging to retrieve complex molecular structures with X-ray and electron diffraction due to locating a global extremum in the multi-dimensional solution space. A small few atoms system quickly finds a convergence but is intractable for the extensive complex system. For example, in the relativistic 3.7 MeV ultrafast electron diffraction (UED) pump-probe time-resolved 1,3-cyclohexadiene ring-opening experiment, even the high kinetic energy electrons provide adequate special resolution. However, the transient process is still blurred and could not identify the complex transient isomers. Laser-induced electron diffraction (LIED) is a strong field variant of the laser-based UED method. It self-images singular molecular structures with their electron combined picometre and femtosecond spatiotemporal resolution. As we mentioned in the Chapter 4, LIED often uses the quantitative rescattering (QRS) theory or Fourier transform (FT) method to retrieve the molecular structures. The QRS method quickly failed to identify a unique solution in the multi-dimensional solution via chi-square fit for large and complex molecules. It is also impossible to calculate all possible structures due to the manifold degrees of freedom. FT-LIED is a remedy method to reduce the problem's dimensionality. However, a multi-peak identification procedure is required to identify internuclear distance, and it becomes ambiguous when the bond distances are close, which generally happens in large molecules.

Here, we present a remedy method for retrieving large and complex molecules using an ML algorithm for LIED. It can accurately predict the three-dimensional (3D) molecular structure with a sufficiently reduced database. It also avoids the use of chi-square fitting algorithms, multi-peak identification procedures, and ab initio calculations. We will predict a single accurate molecular structure on three molecules: acetylene (C_2H_2), carbon disulfide (CS_2) and a complex 3D system, (+)-Fenchone ($C_{10}H_{16}O$) to demonstrate our ML model's capability. The C_2H_2 and CS_2 data has been published previously. The big complex molecule such as fenchone with 27 atoms is firstly retrieved via the ML-LIED technique. The CNN with the regression method quantitatively predicts the geometrical parameters of the molecule with a sufficiently reduced interpolated database. ML model predicts the structure by establishing the relationship between molecular configurations and their corresponding two-dimensional differential cross sections (2D-DCSs) from a database. Using 2D-DCSs of ML algorithm benefits the full range of molecular interference signal instead of typically used 1D signal. The CNN is capable of discriminating subtle features of measured DCSs and interpolating amidst pre-calculated samples to provide a meaningful configuration to measured data. These features of ML CNN are essential to identify complex molecular structures since it is simply impossible to calculate all possible molecular configurations with an adequate structural resolution due to the manifold degrees of freedom. A sufficiently reduced database is performed to avoid computational expenses. Training on a sufficiently reduced database with considering the variation of a few crucial groups of atoms and a molecule-wide global change, endeavouring to let the machine himself perceive the relationship of the input database. The CNN methods have become accessible for the posed problem of LIED, and we find this to overcome standing limitations with more simple methods. Machine learning and LIED technique pave a new way to retrieve the static large and complex molecular structures.

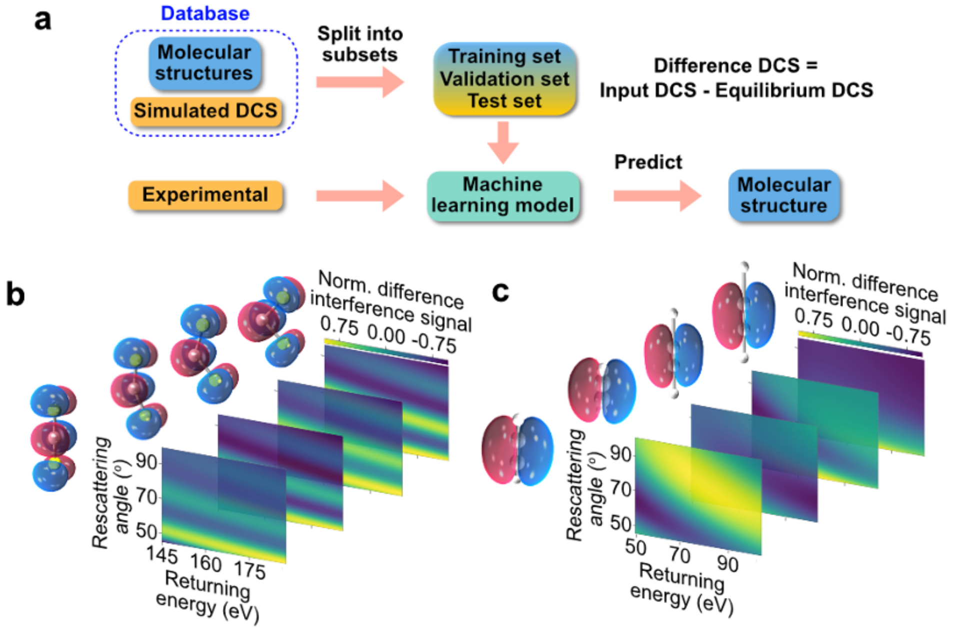

Figure 6.7: **Machine learning schematic.** **(a)** The input dataset comprises thousands of molecular structures and their normalised difference 2D-DCS maps, splitting into three subsets as training, validation, and test set to validate the machine learning model. Next, input the experimental 2D-DCS map to predict the molecular structure that most likely contributes to the measured interference signal. **(b)** and **(c)** 2D-DCS plots for different structures of CS_2 and C_2H_2, respectively. Individual molecular configurations exhibit unique fringe patterns that vary with the molecular geographic information.

6.3.1 Machine learning scheme for LIED

A machine learning schematic in Fig. 6.7, launching with generating a database carrying thousands of possible molecular structures presented by the three-dimensional (3D) cartesian coordinate. For C_2H_2 and CS_2, we calculate 40,000 - 80,000 possible the corresponding 2D-DCS map for each structure using the independent atomic model (IAM) by counting the electron elastic scatters on the molecule. The 2D-DCSs vary with the returning energy (the electron's energy returns to the target ion) and rescattering angle (the angle between the returning beam and the rescattering beam). The measured DCS comprises the (i) incoherent sum of scattering from individual atoms of the molecule, σ_{atom}, and (ii) the coherent scattering signal, σ_{coherent} relaly on molecular interference; this gives $\sigma_{\text{tot}} = \sigma_{\text{atom}} + \sigma_{\text{coherent}}$. Information about the molecule, i.e. its nuclear configuration, is reflected by the position of fringes or features and their functional form, i.e. the slope and dependence of the scattering cross-section on angle and energy.

Subsequent, a slowly varying background has been subtracted from the 2D-DCS maps to enhance different structures' differences. Following standard practice in scattering physics, we subtract a reference structure or an empirically fitted slowly varying and non-oscillating curve from the measured signal. The function type does not alter the information content. Its only purpose is to reduce the incoherent slowly varying background, thus enhancing the interference signal [185]. The interference structure we measure is the doubly differential elastic electron scattering cross-section which we reduce, according to established procedures, to a molecular interference signal. Also, the choice of reference structure does not have to resemble any a priori structure as it only serves to reduce the incoherent background. For simplicity, we use the DCS from the equilibrium structure as a background for a known molecular system. This procedure manages to evident fringe patterns in the resulting difference 2D-DCS maps.

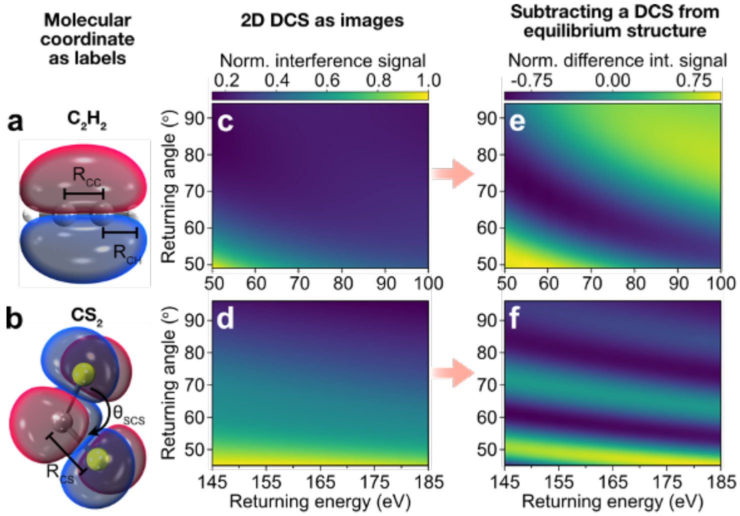

Figure 6.8: **Elastic scattering of molecules as the input of ML model.** **(a)** - **(b)** Molecular coordinate for CS_2 and C_2H_2 as labels in the supervised learning. **(c)** - **(d)** Close inspection of the absolute 2D-DCS maps of CS_2 and C_2H_2. **(e)** - **(f)** Corresponding the difference 2D-DCS maps. The fringe patterns are more visible.

Close inspection of the absolute 2D-DCS maps of CS_2 and C_2H_2 reveal subtle differences between the two molecules in Fig. 6.8. We enhance these subtle differences by subtracting the respective equilibrium molecular structure from all the calculated 2D-DCS maps in our database. Each 2D-DCS in the database and molecular equilibrium structure is divided by its corresponding maximum value to normalise between 0-1. Next, all normalised 2D-DCSs subtract a normalised 2D-DCS of the equilibrium structure, then re-normalise the discrepancies between -1 and +1 through Eq. 6.22 to obtain a difference map.

$$Nor = 2\frac{X - min(X)}{max(X) - min(X)} - 1 \tag{6.22}$$

with $max()$ indicate maximum value and $min()$ indicate minimum value of input array X.

Fig. 6.8 c-d show the raw 2D-DCS maps for C_2H_2 and CS_2, respectively, they look similar to one another. Enhanced existing subtle differences (visible fringe patterns) through subtraction and normalisation are shown in Fig. 6.8 e and f. We could observe a distinctive contrast compared with the raw 2D-DCS maps.

Fig. 6.7 b and c shows exemplary two small molecules 2D-DCS maps for different structures of CS_2 and C_2H_2, respectively. The individual molecular configuration exhibits unique fringe patterns, which vary upon altering the geomatical information of the molecule. Making it significantly easier for the machine algorithm to determine the relationship between the input database.

The input dataset comprises thousands of molecular structures and their normalised difference 2D-DCS maps, splitting into three sets to train, validate, and test the model. (See Fig. 6.7a) The training set trains the ML model to determine the relationship between the 3D molecular structures and their corresponding 2D-DCS maps. The validation set is not directly accessed to train the model but to determine the model's accuracy during the training in each iteration and to determine the hyperparameters for the model, ensuring that the trained model is not overfitting or underfitting. After the training, the test set concludes the model's quality and reliability. Once the model is validated, the molecular structure contributes the most to the measured interference signal predicted by inputting an experimental 2D-DCS to our ML model.

6.3.2 Convolutional neural network training of ML algorithm

Our ML algorithm utilizes a CNN to capture subtle features of 2D-DCSs in the input database. The architecture of CNN is comprised of convolutional layers and fully connected layers. A convolution filter convolutes across an input 2D-DCS map, a schematic of which is shown in Fig. 6.6. It works by extracting features from the input 2D-DCS map using a convolution filter (see white 3×3 grid) to generate a destination pixel. The filter is convoluted across every source pixel of the input map to generate destination pixels in the corresponding feature map.

The CNN uses a variety of different filters as shown in Fig. 6.9a. The filters produce distinct feature maps that maintain prominent subtle features in the 2D-DCS map, making the image recognition process more effective, generating a collection of feature maps after the convolution process. The feature maps possess distinct subtle features of input 2D-DCS map by convoluting various filters, subsequently employed as an input to the fully connected neural network (see Fig. 6.9b). In our ML algorithm, the CNN code is based on the TensorFlow frame comprised of three convolutional layers and 30 fully connected layers. The first convolutional layer included 32 filters with kernel size 5 x 5. 32 filters with kernel size 3 x 3 are utilized in the second layer. The third convolutional contains 32 filters with kernel size 3 x 3. The number of neurons in the fully connected layers ranged from 1024 to the predicted atomic number. A batch size of 120 was used, and

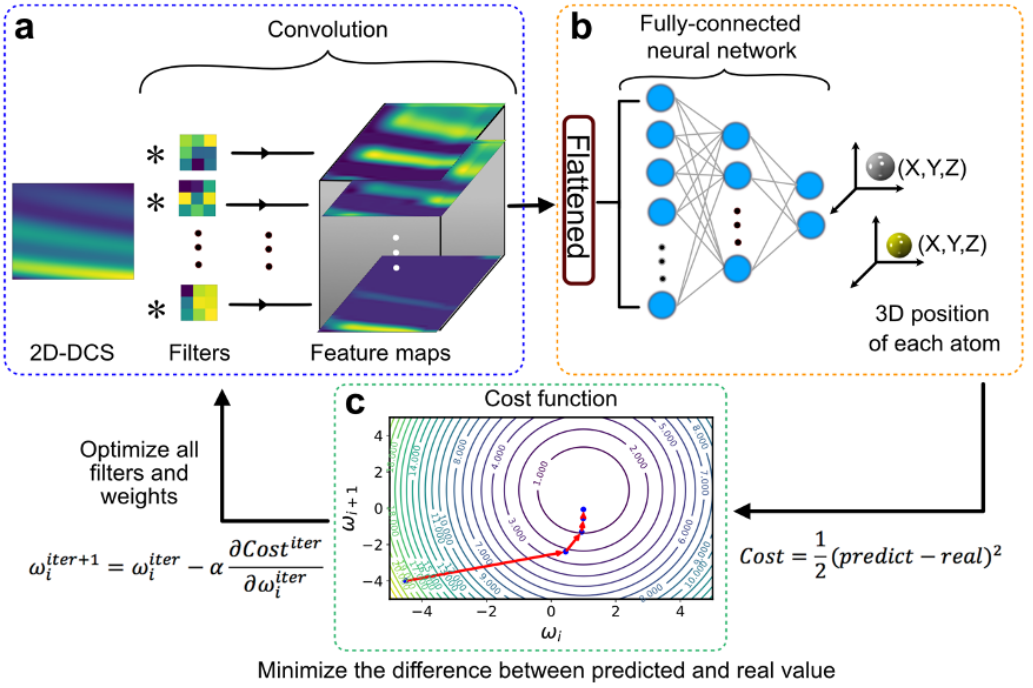

Figure 6.9: **CNN training of ML algorithm to predict molecular structure.** **(a)** Two-dimensional differential cross-section (2D-DCS) convolved with different filters to produce a collection of feature maps. (b) The feature maps are first flattened into a 1D array and then multiplied by the weights between each neuron of all layers in the fully-connected neural network to forecast each atomic position in the molecule. (c) A schematic contour plot of the cost function varies as two weights (ω_i and $\omega_{\mathrm{i+1}}$). The two weights are randomly initialized at the beginning. During five iterations, the value of the cost function decrease is observed, which indicates the predicted values are close to the actual value meanwhile the model is optimized.

batch normalization was applied to avoid overfitting. Then use Root Mean Square Prop (rmsprop) optimizer with a learning rate of 0.0001 to iteratively optimal the ML model.

The neural network typically supports a 1D array as input. We first need to flatten the 3D array of collection of features maps to a 1D array. Then, we multiply each neuron's weight in the first layers. The predicted value of the atomic position is calculated via forwarding propagation through the fully connected neural network. Then, we use backpropagation and grading descent algorithms to minimize the cost function and renew all parameters in the ML model at each iteration. The cost function is defined by the square root difference of the predicted and actual values of the atom's position. A schematic contour plot in Fig. 6.9 shows the cost function varies as two weights (ω_i and $\omega_{\mathrm{i+1}}$) with five iterations. The blue dot shows the value of the cost function, red arrows indicate the gradient descent direction of the cost function, and the length of the arrows exhibit the step size of each iteration, also called the learning rate. The two weights are randomly initialized at the beginning. During five iterations, the value of the cost function decrease is observed, which means the predicted values are close to the actual value meanwhile the model is optimized. In reality, our CNN model contains thousands of parameters like weights, biases and filters instead of only two weights. All the parameters are simultaneously updated at each iteration to reduce the cost function.

6.3.3 Training and evaluation of machine learning model.

We need to evaluate the accuracy of the ML model during and after the training process. The mean absolute error (MAE) is used to visualise the model's accuracy to achieve, known as the prediction error, which counts the absolute difference between predicted and actual value. The input dataset contains thousands of pairs, where a pair corresponds to a molecular structure and their simulated DCS. When a pair is inputted into the ML model, the DCS is used as an input for the ML model to calculate a predicted molecular structure. Comparing the calculated predicted structure and the actual structure from the pair gives the error of our ML model. The average absolute difference between the predicted and actual value of structures for all pairs in the sub-set provides MAE of training, validation and test set.

$$\text{MAE} = \text{avg}|\text{predicted value - actual value}| \tag{6.23}$$

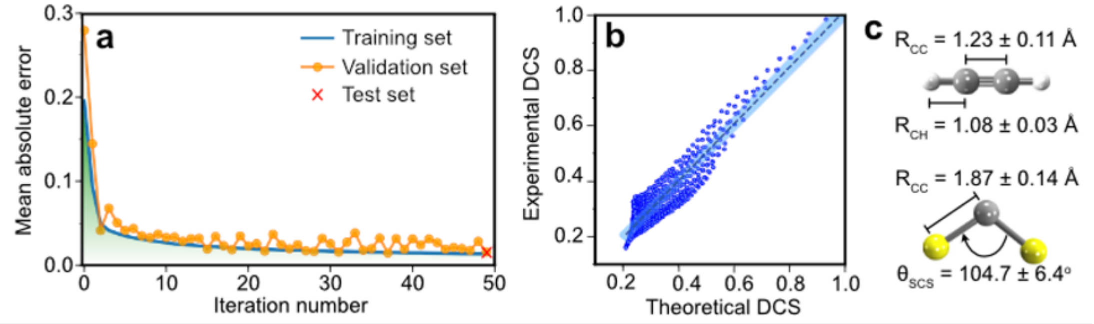

Figure 6.10: **Evaluating machine learning results during and after the training process.** **(a)**The mean absolute error (MAE) achieved with the raising of iteration number for the training and validation set, which converges to a constant value around 0.016 at end. The a red cross indicates the MAE for the test set. **(b)** A strong correlation map between predicted theoretical and experimental 2D-DCS is achieved with a Pearson correlation coefficient of 0.94.

Fig. 6.10a shows that MAE decreased with the raising of iteration number for the training and validation set. Here the iteration in this thesis indicates epoch typically used in the ML audience, referring to the whole database being iterated through the neural network once. The MAE finally converges to a constant value around 0.016 for the training and validation set. A tiny and similar MAE for both sets confirms the model is well-trained and not overfitted or under fitted. After reaching a converged MAE, we use the test set as a third independent data to evaluate the ML's reliability, getting a value of MAE around 0.015 shown a red cross in Fig. 6.10a, achieving a good agreement comparing the value at the end of the training process for the training and validation set.

Three MAE values confirm predicted ability of our ML model is accurate and reliable. The entire training costs one-two hours running on the Google cloud GPU (NVIDIA® Tesla® V100).

Next, we use a normalised measured difference 2D-DCS map as an input to get the predicted measurement's molecular structure, requiring less than one minute of calculation time. The normalisation procedure of the measured difference map is the same as simulated DCSs through Eq. 6.22, calculated from the normalised experimental 2D-DCS (divided by maximum) subtracted by a normalised theoretical 2D-DCS of the equilibrium structure. The normalisation procedure ensures that the DCS value of the experiment and simulation are in the same order, avoiding a fitting factor (called the β factor in QRS) typically used in the fitting routine. Input a normalised measured difference 2D-DCS map to the well trained ML model will produce a predicted molecular structure, which is then used to calculate its corresponding theoretical 2D-DCS to re-evaluate prediction reliability. Figure 6.10b illustrate the correlation map between the corresponding predicted theoretical and experimental DCS after the normalisation. A Pearson correlation value of 0.94 is obtained, proving that both DCSs are strongly correlated and the predicted measured structure is reliable.

6.3.4 Predicting measured molecular structure with machine learning.

We use our ML model to predict the geomatical information of CS_2 and C_2H_2 from the experimental DCS trained on five separate occasions. Figure 6.11 shows the structural parameters of the predicted structures (green circles) along with the structure retrieved by the QRS model (blue dashed line) together with its area of uncertainty (blue shaded area). We obtain predicted structures for C_2H_2 (CS_2) of $R_{CC}=1.23 \pm 0.11$ Å and $R_{CH}=1.08 \pm 0.03$ Å ($R_{CS}=1.87 \pm 0.14$ Å and $\theta_{SCS}=104.7 \pm 6.4^o$) which agrees well with the corresponding values retrieved by the QRS method, as shown in Table 6.2. The predicted structures retrieved by each of the five ML models slightly vary because the neural network uses a random number generator to select the input-target pairs of data and randomly initialise each neuron's weight, bias, and filters. Training with randomly starting conditions for the neurons ensures that each training occasion is independent. If the variance of each output is too large, it indicates the ML model either is overfitting or produces the greatest possible prediction error.

Table 6.2: Machine learning C_2H_2 and CS_2 predicted structures

	Parameter	Equilibrium	QRS	ML
C_2H_2	R_{CC}(Å)	1.20	1.24 ± 0.04	1.23 ± 0.11
	R_{CH}(Å)	1.06	1.10 ± 0.03	1.08 ± 0.03
CS_2	R_{CS}(Å)	1.86	1.86 ± 0.23	1.87 ± 0.14
	θ (^{o})	180	104 ± 20.2	104.7 ± 6.4

Here, the relatively consistent values of predicted structures from five separate occasions with low variance and low bias ensure the reliability of the predicted values. The ML model predicted error and the experimental statistical error are two main contributions of the uncertainty in the algorithm. The model predicted error is calculated from the MAE of the test set. It computed the absolute difference of the actual and predicted value of the structural information from the test set. Since our experimental data follows a Poisson distribution, the experimental error is calculated as a variance of the Poisson distribution, which is a square root of our experimental data. We add or subtract the square root of the DCS value to the experimental DCS as $DCS - \sqrt{DCS}$ to $DCS + \sqrt{DCS}$. Considering this range as an input will give us different predicted molecular structures. The displacement between different predicted molecular structures contributes to our experimental error shown as:

$$\text{Error}_{\text{exp}} = |f_{(\text{DCS}+\sqrt{\text{DCS}})} - f_{\text{DCS}}| + |f_{(\text{DCS}+\sqrt{\text{DCS}})} + f_{\text{DCS}}| \tag{6.24}$$

Thus, the total error is the sum of the model predicted error, the experimental statistical error and variant of multi-training occasions.

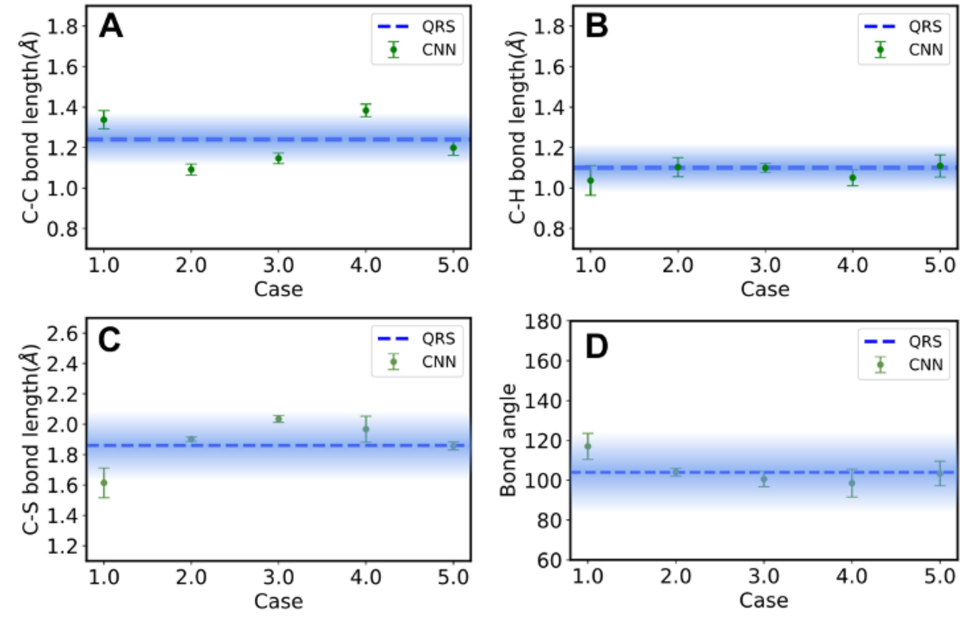

Figure 6.11: **Predicted molecular structures by machine learning.**The predicted (green dots) and QRS retrieved (blue dashed line) C_2H_2 structure along its (A) C-C and (B) C-H bond lengths. The ML model was trained fives to ensure the accuracy and reliability of predicted results. The shaded blue region indicates the area of uncertainty for the QRS retrieved structure. The predicted and QRS retrieved CS_2 structure along the (C) C-S bond length and (D) SCS bond angle.

6.3.5 Predicting (+)-Fenchone molecular structure.

We demonstrate proof of principle of ML-LIED with simple small 1D and 2D molecules and compared to the previous methodology. We find an excellent agreement with previous result. Now, we go beyond the previous method using our ML framework to extract the large and complex structure as (+)-Fenchone ($C_{10}H_{16}O$; 27 atoms) molecule. Ideally, for retrieving large complex structures, we need to calculate the variation of all atoms in the molecule within an extensive database. However, it is calculation expensive to traversal all possibilities. Total calculation time scales as $n_{\text{steps}} * 3^{n}_{\text{atoms}}$, considering each atom has three-fold freedoms, n_{atoms} is the number of atoms and n_{steps} is the number of steps per atom. Using a single-core 1.6 GHz computer needs 5 minutes to generate a 2D-DCS map. A complex system contains 20 atoms with five steps that need calculation time up to 1.4×10^{9} hours. Here, the ML has the emphatic benefit of interpolating and learning among the coarse grid of the pre-calculated database and taking into account a manifold of degrees of freedom in the solution space.

Hence, we establish a sufficiently reduced database with 120 000 structures that only considers the changes of 4 essential groups and a molecule-wide global change in the structure. Meanwhile, hydrogen atoms are ignored due to a lower elastic electron scattering cross-section contribution. We only consider the stretching and shrinking along the C-O bond direction in the first group due to the double bond connection. In the second and fourth groups, the variation of bond length and bond angle for C-CH_3 methyl connection are considered. For group 3, we mainly consider rotation. Also, all bond lengths identically the stretching and shrinking are included. Following such a reduced database, we train the ML model to determine the relationship between the molecular structures and their correspondence DCSs. This proposition drastically depreciates computational time.

Figure 6.12a shows the MAE reduced as iteration number rises with training and validation sets. We are training more iteration numbers because of the more complexity of the input data. Four groups of the atoms training are shown in the inset of Fig. 6.12a. Both training and validation sub-sets achieve around MAE value around 0.02, demonstrating that the ML model could be successfully trained on a large molecule. Figure 6.12b shows a strong correlation between an experimental and a theoretical 2D-DCS from a predicted molecular structure in a correlation map with the Pearson correlation coefficient of 0.94. The varied seven atoms in the four groups of (+)-Fenchone in 3D cartesian positions are shown in Fig. 6.12c. The green circles exhibit the predicted structures using the ML model, and red triangles show the corresponding equilibrium ground-state neutral molecular structure. The error bar is calculated from the sum of the predicted model error, the experimental statistical error and variant of multi-training occasions. We notice that the predicted structure only shows a slight deviation from the molecular equilibrium structure, which is involuntarily caused by the LIED laser field's presence. The predicted molecular structure and their index of atom number are shown in Fig. 6.12d. The green shadow area presents uncertainty of predicted structural information. Thus, we have successfully retrieved (+)-Fenchone molecular structure combined with ML algorithm and LIED technique.

6.3.6 Induced error of the IAM approximation

In a perfect world in which theory and experiment exactly match and there is no noise in measurements nor approximations in simulations. Nevertheless, this never happens, and we have to deal with imperfections and overcome limitations as best as possible.

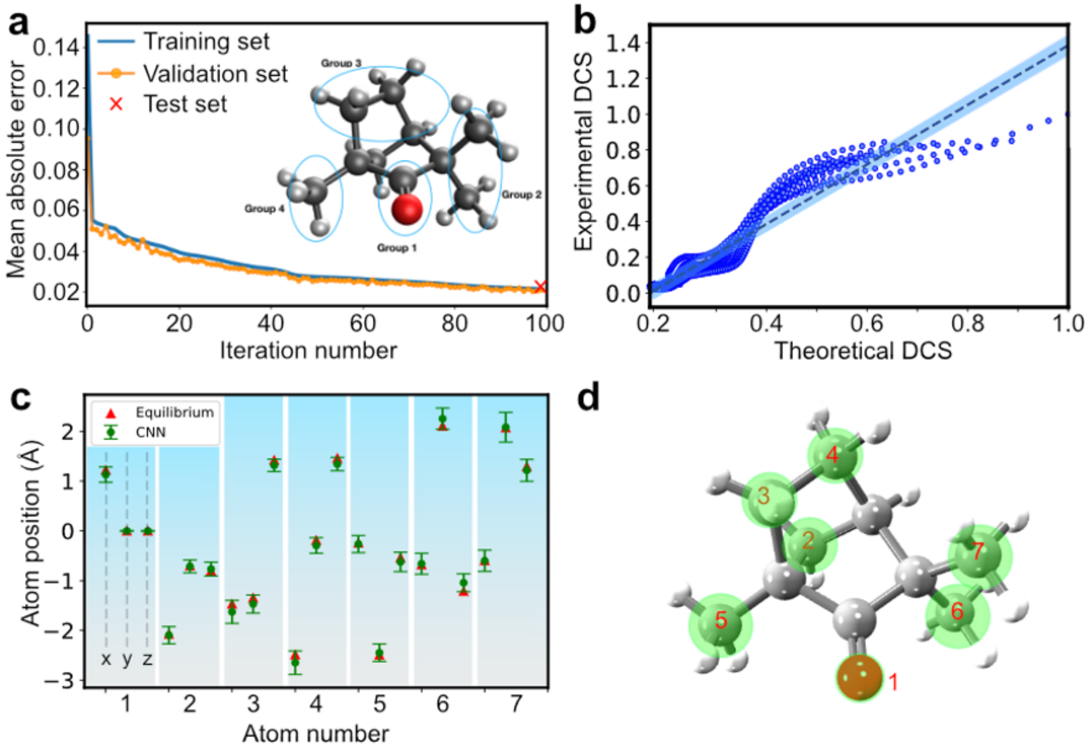

Figure 6.12: **Extracted (+)-Fenchone molecular structure by machine learning.** **(a)** Mean absolute error (MAE) at each iteration using training and validation sets of simulated data. The red cross indicates the MAE of the test set. The inset shows a schematic of the algorithm training on the four groups of the (+)-Fenchone molecule. **(b)** shows a correlation map between an experimental and a theoretical 2D-DCS from a predicted molecular structure. **(c)** The ML predicted seven atoms of (+)-Fenchone in 3D cartesian coordinate with the green circles, and red triangles show the corresponding equilibrium ground-state neutral molecular structure. **(d)** The Schematic of ML predicted molecular structure and their index of atom number. The green shadow area indicates an uncertainty area.

How much error would the IAM impart in such a hypothetical case? We are using the program ELSEPA [186] to calculate elastic electron scattering. The code uses relativistic partial wave calculations for scattering by a local central interaction potential in the static field approximation, with an approximate local exchange interaction and a term taking polarizability into account. Further, the code makes use of the muffin tin potential and local density approximation. Quantification of the error using the IAM depends on momentum transfer range, i.e., impact angle and energy. Within the approximations by theory and the experimental uncertainties, we estimate errors in bond length due to the IAM in the typical LIED momentum transfer range may range from a few per cent, up to 10% for the worst cases. The previous work which have shown such good agreement [187, 144, 188, 189, 190]. Concerning the error would the IAM approximation induce, the intrinsic error caused by the IAM does not get compensated for by the IAM. However, the huge database of structures for CNN reduces possible errors by providing a much larger solution space than what was available previously. It allows being sensitive to a larger number of parameters that are compared. For instance, an evolutionary algorithm, steepest descent, or temperature annealing methods severely constrain the degrees of freedom they can handle. I.e., nearly any approach, therefore, has to simplify the problem. Even for a triatomic molecule, such methods use the projected 1D values of a 3D structure rather than the 3D solution space. This is exactly the proposed CNN for this problem which has much more relaxed constraints and better converges.

6.3.7 Discussion

Our work establishes an ML-based framework to surmount present constraints in structural retrieval from diffraction measurements. The difficulty with present methods is the necessity to match an experimental diffraction pattern with a pre-simulated structure and the remarkably inadequate scaling of pattern matching methods with the rapidly growing degrees of freedom of complex molecules—the requirement to pre-calculate many molecular configurations in different orientations and with high resolution. Further, identifying a global extremum in a multi-dimensional solution space is a challenging problem. These issues are tractable for a simple few molecular systems where dimensionality could be degraded significantly. However, it is not ductile for large and complex molecular structures.

To succeed in the unfavourable scaling of the problem, we first examine our machine learning ability that predicts the molecular structure of C_2H_2 and CS_2 with published data. Then, we break through the limitation of the previous method using our ML algorithm successful in predicting the large and complex as (+)-Fenchone molecular structure. We train ML models with an interpolated database, including thousands spanning an extensive array of possible molecular structures and their corresponding simulated 2D-DCSs. Once the ML is validated, the experimental DCS has used an input to predict the molecular structure of the measurement. A tiny MAE obtained during and after the training process and a strong correlation between experimental and simulated data demonstrate the ability of ML algorithm could extract structural information from experimental LIED data. Our novel ML method offers several advantages compared with other methods: (i) Comparing with least-square fitting, chi-square fitting and Lookup table (LUT) method that traversal the all points in the database to find out the best fitting point. The ML may not run as fast as these methods due to the time consumption of training the model to find the relationship between input databases. It is not different for a few atoms simple system. However, a more extensive and complex system cannot calculate all possible structures due to the expensive calculation. It will be restricted to apply a fitting routine to retrieve molecular structure. Alternatively, we could train the ML model with a sufficiently reduced interpolated database to let the machine himself learn the relationship of the input dataset to predict the geomatical information of the molecule. (ii) ML-LIED can predict the 3D position of each atom in the molecule, providing significantly more structural information than other LIED and UED methods that rely on the Fourier transform of the measured interference signal, which are typically restricted to 1D radial distributions. Large and complex molecular structures contain a larger number of peaks in the radial distribution due to the many more two-atom combinations in the larger molecule. Thus, this leads to the significant overlap and blurring of closely lying internuclear distance peaks in multi-peak features of the 1D radial distribution, making structural retrieval quite challenging. (iii) ML-LIED is superior to QRS-LIED in reducing the required computational for structural identification in time-resolved pump-probe measurement. A series of experimental 2D-DCSs will be generated for different pump-probe time delays in such a measurement. For QRS-LIED, the chi-square fitting procedures need to be performed repeatedly for each measured 2D-DCS data which is time-consuming. With ML-LIED, once the ML model is validated, the molecular structures can be predicted for each input experimental 2D-DCS map, avoiding the high computational cost of repeated chi-square fittings as in time-resolved QRS-LIED. (iv) Using 2D-DCSs as input instead of 1D distribution, the 1D data is always applied in the previous method, maximising the confidence to identify a complex system by utilising the complete interference signal; (v) No prior information or biased structure determination procedures are required. There may be several potential constraints in the ML model. First, there must be a clear and unique pattern in the difference 2D-DCS mapping so that the ML model can learn the relationship. Second, in the future time-resolved pump-probe LIED measurement, ”unpumped” ground state and ”pumped” transient state molecular structure may contribute to the overall LIED signal. The ML model must be adjusted and trained based on the presence of the combined total signal from two or more molecular structures.

As mentioned earlier, advantages and manageable constraints will provide essential applications for ML-LIED. Using a sufficiently reduced database to predict the 3D structure of relatively large and complex molecules while other models like fitting based or Fourier transform-based UED may fail.

The ML algorithm also has more opportunities to identify the contribution of two or more molecular structures to the total measured interference signal. For example, in time-resolved isomerisation or ring-opening reactions, changes in molecular structure will cause subtle changes in the measured 2D-DCS. The convolutional neural network of our ML model could be a potential candidate to capture these subtle feature changes and predict the molecular structure of the measurement. Therefore, the combination of machine learning algorithm and LIED technique provides new opportunities to determine the large and complex molecular structures.

Chapter 7

Conclusions and Perspectives

Contents

7.1 Main conclusions

The interaction between light and matter is state of the art to explore the laws of the microscopic world. Modern light and matter interaction research have directly benefited from the invention and development of lasers. In this thesis, we study the intense (> 10^{13} W/cm^2) ultrafast (<100 fs) mid-IR waveforms that interact with molecular gas-phase targets with a reaction microscope. The high repetition rate optical parametric chirped pulse amplification laser system creates a deep tunnelling ionization regime (quasi-static conditions) that are favourable for classical descriptions of experimental results. On the other hand, the ultra-short electron beam driven by the long-wavelength laser own higher energy, and its corresponding shorter De Broglie wavelength provides higher spatial resolution for the LIED method. The reaction microscope detection system can capture the 3D momentum of all interacted particles with complete coincidence. The setup enables the identification of the interesting fragments and their correspondence electrons, thus providing an authentic 3D view of strong-field interactions.

The prerequisite for detecting and controlling ultrafast dynamics is to obtain a ”probe” with adequate spatial and temporal resolution. The currently developed ultrafast probes can be divided into two categories: the first category is ”ultrafast optical probes”, attosecond light pulses generated from high-order harmonics through the interaction of intense femtosecond lasers with atomic and molecular gases. The second category is ”ultrafast electron beam probes”, on which our research is based. Through the intense femtosecond laser and atomic and molecular gas interaction, the electron beam generated by laser-driven atomic or molecular ionization has ultra-short time characteristics, which can be used for attosecond time-resolved microscopic process research.

- **Imaging an isolated water molecule using a single electron wave packet.**

Knowledge of how the nuclear framework of molecules couple and respond to external fields provide essential insights into field-driven changes in molecular structure typically observed in strong-field physics. To obtain such insights requires the capacity to directly image the entire molecular structure with atomic resolution in real-time. Image the geometric structure and dipole moment of the water, can help us visualize the mechanisms of biologically essential processes like protein folding dynamic affected by the solvation shell. In Chapter 4, we report on the directly retrieved molecular structure of an isolated H_2O^+ cation exposed to an intense external laser field without a priori knowledge of molecular structure nor the use of retrieval algorithms or ab initio calculations. We resolve the field-driven symmetric stretching of the O-H bond in H_2O^+ using Fourier transform (FT) the variant of LIED (FT-LIED) [143, 144] with picometre and femtosecond spatio-temporal resolution. In FT-LIED, the geometric structure can be directly retrieved without any prior knowledge or the use of retrieval algorithms. It is crucial since structural information is typically indirectly retrieved using microwave and rotational spectroscopy [145, 146], which, in contrast, require ab initio calculations to interpret the measured data.

Direct electrons escape the laser field without rescattering, possessing kinetic energy up to $2U_\mathrm{p}$. Whilst the rescattered electrons collide with the parent's ion attaining energy from $2U_\mathrm{p}$ to $10U_\mathrm{p}$. By analyzing rescattered electrons isolated by the energy range with the Fourier variant of the LIED technique, we trace the field strengths induced ultrafast stretching of a field-dressed H_2O^+ cation in its ground electronic state with combined picometre and femtosecond resolution. We show that the laser intensity from 2.5 V/Å to 3.8 V/Å, which mimics the same order liquid water experienced in natural conditions, internuclear distance stretches to 14%–35% (ROH) and 17%–35% (RHH) compared with the equilibrium field-free H_2O^+ ground-state structure. The correspondence dipole moment of H_2O^+ up to 3.15 D are significantly higher than the field-free neutral H_2O and H_2O^+ cation values. Moreover, we also demonstrate that LIED is sensitive to hydrogen scattering as few techniques could capture the hydrogen motion.

- **High-density molecular jets of complex neutral organic molecules with Tesla valves**

The study of large, isolated organic molecules in the gas phase is a standing challenge, given that these molecules typically exist either in the liquid or solid phase at room temperature and ambient pressure. The samples can be heated and introduced to an ultra-high vacuum environment which generates a gaseous sample, but their vapour pressure is still too low for measurement (below 1 mbar). Currently, it is challenging to deliver dense molecular jets of neutral complex molecules without ionizing or exciting the target.

Chapter 5 presents a remedy based on a novel gas delivery system utilizing a series of micro-sized no-moving parts Tesla valves to generate molecular jets of neutral complex molecules. The Tesla valve is a passive one-way valve with a fixed geometry to ensure a stream flows preferentially in one direction. The other direction will have tremendous resistance or even no flow.

We prove the utility of the new gas delivery system on the strong-field ionization of cis-stilbene molecules as a test case for complex organic molecules with a vapour pressure of less than 1 mbar. It accomplishes a comparatively long measurement time (> 6 hours) using only a 1.5ml liquid sample, causing it possible to achieve strong-field ionization measurements on such large and complex low vapour pressure molecules. We design a bubbler delivery system to maximize the evaporation of the target liquid sample, and the Tesla valve ensures that the vapour flows in one direction. The target sample will easily be stuck and positioned around the delivery system without the Tesla valve. Secondly, compared with the tesla valve's absence, we achieved an order of magnitude increase in the cis-stilbene molecular ions portion to the total detected ion signal. It points to the possibility of achieving LIED measurement considering the measurement time and the signal-to-noise ratio of our cis-stilbene signal. We systematically examined the experimental conditions affecting the ion signal using the Tesla valve bubbler, such as laser power, carrier gas backing pressure and reservoir temperature. We show that the molecular ion signal ratio can be maximized by measuring under the following conditions: (i) relatively low peak laser intensity; (ii) high helium back pressure; (iii) high reservoir temperature.

Flow simulations quantitatively illustrate the working principle of unidirectional flow with the Tesla to mitigate counter flow and clogging of the delivery nozzle. The simple but effective gas-delivery system will benefit a wide range of experiments since it will enable measurements on already difficult-to-measure molecular samples with low vapour pressures.

- **Machine learning for laser-induced electron diffraction imaging of molecular structures**

  Research at the intersection of physics and machine learning has provided many spectacular advances due to the capacity to solve complex problems with advanced numerical algorithms. LIED imaging presents such a complex problem since retrieving nuclear coordinates requires equating to finding the global minimum in a complex multi-dimensional solution landscape. Chapter 6 presents a remedy based on a specific implementation of a convolutional neural network (CNN). The solution is based on a pre-calculated and sufficiently large ensemble of structural solutions, which the network can identify as matching the measured structure.

  We firstly examined our ML framework to retrieve small systems with LIED and showed the application to 1D linear symmetric molecule acetylene (C_2H_2) and 2D planar molecule carbon disulfide (CS_2). Demonstrating proof of principle ML-LIED with simple small 1D and 2D molecules compared to the previous methodology, which agrees with previous publications.

  We prime calculate thousands of possible corresponding two-dimensional differential cross sections (2D-DCSs) maps for each structure using the independent atomic model (IAM) by counting the electron elastic scatters on the molecule. Next, training a CNN to determine the relationship between molecular structures and correspondence simulated 2D-DCS diffraction patterns from the prepared database. After the ML model is validated, the measured molecular structure can be predicted by inputting an experimental 2D-DCS. Meanwhile, we also present a strong correlation between experimental and simulated 2D-DCSs and show that the accuracy and reliability of the predicted molecular structure. We contrast these findings against several previously measured structures and all are retrieved with the highest fidelity through the ML framework.

With the successful examination of the smaller molecules' retrieval, we use our ML framework to study the configuration of a large, complex and chiral molecule (+)-fenchone ($C_{10}H_{16}O$; 27 atoms), measured with LIED. Such a large and complex 3D molecule will require an unrealistic 1.4×10^9 h of calculation time with five variations in a standard fitting routine. Here, we establish a sufficiently reduced interpolated database that only considers the changes of four essential groups and a molecule-wide global change in the structure. Meanwhile, hydrogen atoms are ignored due to a lower elastic electron scattering cross-section contribution. This proposition drastically depreciates computational time. The ML has the emphatic benefit of interpolating and learning among the course grid of the pre-calculated database and taking into account a manifold of degrees of freedom in the solution space.

The machine learning algorithm overcomes convergence issues and drastically depreciates computational time for the complex system to predict three-dimensional (3D) molecular structures measured with LIED. In summary, we present a new approach to overcome scaling issues in image retrieval that impede further advances in ultrafast structural dynamics research and impact the larger area of diffracting imaging. The method is scalable to complex and large molecular structures and overcomes present scaling issues of multi-peak fitting and search routines in high-dimensional solution spaces. The implementation of CNN for diffraction imaging is shown to retrieve molecular structures accurately and applies to scattering or diffraction imaging, independent of the exact implementation with X-rays or electrons. ML combined with LIED provides a new general solution to overcome standing problems and a new opportunity to determine the structure of large molecules.

7.2 Future research

Studying the fundamental physical process induced by the intense femtosecond laser with atoms and molecules plays an indispensable role in understanding the interaction mechanism between light and matter. In recent years, with the emergence and maturity of mid-infrared long-wavelength intense laser and free-electron laser technology, the research of strong-field atomic physics has expanded to the limits of ”long-wavelength” and ”short-wavelength”. Under long-wavelength and strong fields, dipole approximation will no longer be properly applicable, and the introduction of Lorentz force and magnetic field may cause some new ionization phenomena.

On the other hand, as the research system gradually expands to complex molecules, clusters and even solid systems, physical effects such as polyatomic centre interference, molecular spatial orientation, multi-body effects, etc will be involved in the ionization process. Physical pictures of the strong field are based on simple atomic and molecular systems, such as tunnel ionization and electron rescattering images. Whether it can effectively deal with the many-body effects in complex systems and describe the strong-field ionization dynamics of complex molecules, clusters and even solid systems remains to be further studied.

At the same time, the ultrashort electron beam probe driven by an intense laser field will continue to promote people's understanding of the ultrafast dynamics of atoms and molecules on the sub-femtosecond time scale. This thesis successfully retrieved static large, complex organic molecules such as (+)-Fenchone well prepared in the experiment setup and retrieval algorithms which paved the way to image complex molecular dynamics.

Next, UV pump-probe time-resolved complex photon-induced molecular dynamics will be investigated, such as isomerization, ring-opening, dissociation and tautomerization. Although static equilibrium structures are well-known, the transition structure and reaction pathway are still unclear, involving structural rearrangements in molecules that typically span 10 fs to 1 ps time scale. It is particularly noteworthy, as it suggests that we can initiate an ultrafast change in the geometric structure of a polyatomic molecule as well as record a high-resolution snapshot of the structural change with a laser pulse. Coupling a few-cycle LIED pulse with a separate pump pulse will enable an actual ”molecule movie” of isomerization reactions in biomolecular photoswitches to be recorded. Such reactions play an essential role in the correct functioning example, the human eye.

Acronyms

ADK Ammosov, Delone and Krainov (model)

AMO atomic, molecular and optical (physics)

AR anti-resonant

ATI above-threshold ionization

aug-cc-PVTZ correlation consistent-polarized valence double zeta

AUO Attoscience and Ultrafast Optics (group)

CASSCF complete active space self-consistent field

CEP carrier-envelope phase

CERN European Organization for Nuclear Research

CFD constant fraction discriminator

CFD computational fluid dynamics

CNN convolutional Neural Network

COLTRIMS cold target recoil ion momentum spectroscopy

DCS classical trajectory Monte Carlo

DFG difference-frequency generation

DFT density functional theory

DLA delay line anodee

EWP electron wave packet

FROG frequency-resolved optical gating

FFT Fast Fourier transform

FT Fourier transform

FWHM full-width half-maximum

GAN Generative Adversarial Network

GUI graphical user interface

HATI high-energy ATI

HHG high harmonic generation

HOMO highest occupied molecular orbital

HHG high harmonic generation

IAM independent atom model

ICFO Institute of Photonic Sciences (catalan: Institut de Ciències Fotòniques)

KER kinetic energy release

KFR Keldysh, Faisal and Reiss (model)

KLM Kerr-lens mode-locking

KNbO3 Potassium niobate

LCLS Linac Coherent Light Source

LIED laser-induced electron diffraction

LSTMs Long Short- Term Memories

ML machine learning

MBS multi-branch system (stream server)

MCF molecular contrast factor

MCP multi-channel plate (detector)

MeV Mega-electron-Volt

mid-IR mid infrared

MPI multi-photon ionization

MPIK Max-Planck-Institut fur Kernphysik, Heidelberg, Germany

NSDI non-sequential double ionization

OPA optical parametric amplification

OPCPA optical parametric chirped pulse amplification

OpenFOAM Open Source Field Operations and Operations

RANS Reynolds Average Navier-Stokes

PD photo diode

PPLN periodically poled lithium niobate

PPT Perelomov, Popov and Terent'ev (model)

QRS quantitative re-scattering (theory)

QS quasi-static

ReLU rectified linear unit

ReMi reaction microscope

RNN Recurrent neural network

RWP returning wave packet

SFI strong-field ionization

SFA strong-field approximation

SHG second-harmonic generation

SIMPLE semi-implicit method for calculating the pressure correlation equation

SMM simple man's model

TDC time-to-digital converter

TDSE time-dependent Schrödinger equation

TI Time-of-flight spectrometer

ToF tunneling ionization

UED ultrafast electron diffraction

UHV ultrahigh-vacuum

XFELs X-ray Free Electron Lasers

XRD X-ray diffraction

1D one-dimensional

2D two-dimensional

3D three-dimensional

- -

Appendix

The atomic unit is a system of units widely used in atomic physics, especially when studying the properties of electrons. It is based on:

$$\hbar = e = m_e = 4\pi\epsilon_0 = 1 a.u. \tag{7.1}$$

This simplifies many theoretical expressions and makes numerical calculations more convenient. The table below summarizes the basic quantities and physical constants of the SI unit system and their respective conversion factors. In this thesis, atomic units are used unless otherwise stated.

Table 7.1: Atomic unite to SI unit

physical quantity	definition	1 a.u. correponds to
mass	electron mass m_e	9.10938×10^{-31} kg
charge	elementary charge e	1.60218×10^{-19}As
length	Bohr radius a_0	5.29177×10^{-11} m
energy	$E_h = m_e e^4/\hbar^2$	$4.3597443 \times 10^{-18} J$ 27.21 eV
angular momentum	$\hbar$	1.0545726×10^{34}J s $6.58211928 \times 10^{-16}$ eV s
time	$t = \hbar/E_h$	$2.41888433 \times 10^{-17}$ s ≈24.2 as
velocity	$v_0 = a_0/t$	2.18769×10^{6} m/s
momentum	$p_0 = m_e v_0$	$1.99285174 \times 10^{-24}$ kg m/s
angular frequency	$\nu = v_0/a_0$	4.13414×10^{16} Hz
electric field	$E = e/(4\pi\epsilon_0 a_0)$	5.14221×10^{11} V/m
intensity	$I = E^2$	6.4364091×10^{19} W/m2
laser intensity	$I_{\text{laser}} = 0.5\epsilon_0 c E^2$	3.5094451×10^{20} W/m2
proton mass m_p	1836.15 a.u.	1.672621×10^{-27} kg
velocity of light c	137.04 a.u.	2.99792×10^{8}m/s

List of Publications

- **Xinyao Liu**, Kasra Amini, Aurelien Sanchez, Blanca Belsa, Tobias Steinle, and Jens Biegert, “Machine learning for laser-induced electron diffraction imaging of molecular structures” Commun Chem 4, 154 (2021).
- Moniruzzaman Shaikh*, **Xinyao Liu***, Kasra Amini*, Tobias Steinle, and Jens Biegert, “High density molecular jets of complex neutral organic molecules with Tesla valves”, Review of Scientific Instruments 92, 104103 (2021)
- Aurelien Sanchez, Kasra Amini, Wang, SuJu, Tobias Steinle, Blanca Belsa, Jiri Danek, Anh-Thu Le, **Xinyao Liu**, Robert Moshammer, Thomas Pfeifer, Martin Richter, Joachim Ullrich, Stefanie Gräfe, C. D. Lin, Jens Biegert, “Molecular structure retrieval directly from laboratory-frame photoelectron spectra in laser-induced electron diffraction” Nat Commun 12, 1520 (2021).
- Blanca Belsa, Kasra Amini, **Xinyao Liu**, Aurelien Sanchez, Tobias Steinle, Johannes Steinmetzer, Anh-Thu Le, Robert Moshammer, Thomas Pfeifer, Joachim Ullrich, Robert Moszynski, Chii-Dong Lin, Stefanie Gräfe, Jens Biegert, Laser-induced electron diffraction of the ultrafast umbrella motion in ammonia Structural Dynamics 8, 014301 (2021).
- **Xinyao Liu**, Kasra Amini, Tobias Steinle, Aurelien Sanchez, Moniruzzaman Shaikh, Blanca Belsa, Johannes Steinmetzer, Anh-Thu Le, Robert Moshammer, Thomas Pfeifer, Joachim Ullrich, Robert Moszynski, C. D. Lin, Stefanie Gräfe, and Jens Biegert “Imaging an isolated water molecule using a single electron wave packet”, J. Chem. Phys. 151, 024306 (2019)

List of Figures

List of Tables

Bibliography

[1] Mitchell Leslie. The man who stopped time, 2001.

[2] Ahmed H Zewail. Femtochemistry: Atomic-scale dynamics of the chemical bond. *The Journal of Physical Chemistry A*, 104(24):5660–5694, 2000.

[3] TH MAIMAN. Stimulated optical radiation in ruby. *Nature*, 187(4736):493–494, 1960.

[4] FJ McClung and RW Hellwarth. Giant optical pulsations from ruby. *Applied Optics*, 1(101):103–105, 1962.

[5] Jean-Claude Diels and Wolfgang Rudolph. *Ultrashort laser pulse phenomena*. Elsevier, 2006.

[6] Francesca Calegari, Giuseppe Sansone, Salvatore Stagira, Caterina Vozzi, and Mauro Nisoli. Advances in attosecond science. *Journal of Physics B: Atomic, Molecular and Optical Physics*, 49(6):062001, 2016.

[7] Dongping Zhong and Ahmed H Zewail. Femtosecond real-time probing of reactions. 23. studies of temporal, velocity, angular, and state dynamics from transition states to final products by femtosecond-resolved mass spectrometry. *The Journal of Physical Chemistry A*, 102(23):4031–4058, 1998.

[8] Jie Yang, Xiaolei Zhu, Thomas JA Wolf, Zheng Li, J Pedro F Nunes, Ryan Coffee, James P Cryan, Markus Gühr, Kareem Hegazy, Tony F Heinz, et al. Imaging cf3i conical intersection and photodissociation dynamics with ultrafast electron diffraction. *Science*, 361(6397):64–67, 2018.

[9] Benjamin Wolter, Michael G Pullen, A-T Le, Matthias Baudisch, K Doblhoff-Dier, Arne Senftleben, Michael Hemmer, C Dieter Schröter, Joachim Ullrich, Thomas Pfeifer, et al. Ultrafast electron diffraction imaging of bond breaking in di-ionized acetylene. *Science*, 354(6310):308–312, 2016.

[10] YH Jiang, Artem Rudenko, Oliver Herrwerth, L Foucar, M Kurka, KU Kühnel, Matthias Lezius, Matthias F Kling, Jeroen van Tilborg, Ali Belkacem, et al. Ultrafast extreme ultraviolet induced isomerization of acetylene cations. *Physical review letters*, 105(26):263002, 2010.

[11] GS Voronov and Nikolai B Delone. Ionization of the xenon atom by the electric field of ruby laser emission. *Soviet Journal of Experimental and Theoretical Physics Letters*, 1:66, 1965.

[12] JL Hall, EJ Robinson, and LM Branscomb. Laser double-quantum photodetachment of i-. *Physical Review Letters*, 14(25):1013, 1965.

[13] M Protopapas, Christoph H Keitel, and Peter L Knight. Atomic physics with super-high intensity lasers. *Reports on Progress in Physics*, 60(4):389, 1997.

[14] F Fabre, Guillaume Petite, Pierre Agostini, and M Clement. Multiphoton above-threshold ionisation of xenon at 0.53 and 1.06 μm. *Journal of Physics B: Atomic and Molecular Physics*, 15(9):1353, 1982.

[15] Guillaume Petite, F Fabre, Pierre Agostini, Michele Crance, and Michelle Aymar. Nonresonant multiphoton ionization of cesium in strong fields: Angular distributions and above-threshold ionization. *Physical Review A*, 29(5):2677, 1984.

[16] Louis-Andre Lompré, Anne L'Huillier, Gerard Mainfray, and Claude Manus. Laser-intensity effects in the energy distributions of electrons produced in multiphoton ionization of rare gases. *JOSA B*, 2(12):1906–1912, 1985.

[17] Farhad HM Faisal. *Theory of multiphoton processes.* Springer Science & Business Media, 1987.

[18] Pierre Agostini, F Fabre, Gérard Mainfray, Guillaume Petite, and N Ko Rahman. Free-free transitions following six-photon ionization of xenon atoms. *Physical Review Letters*, 42(17):1127, 1979.

[19] E Karule. Two-photon ionisation of atomic hydrogen simultaneously with one-photon ionisation. *Journal of Physics B: Atomic and Molecular Physics*, 11(3):441, 1978.

[20] P Kruit and FH Read. Magnetic field paralleliser for 2π electron-spectrometer and electron-image magnifier. *Journal of Physics E: Scientific Instruments*, 16(4):313, 1983.

[21] P Kruit, J Kimman, Harm G Muller, and MJ Van der Wiel. Electron spectra from multiphoton ionization of xenon at 1064, 532, and 355 nm. *Physical Review A*, 28(1):248, 1983.

[22] W Xiong, François Yergeau, See-Leang Chin, and Pierre Lavigne. Multiphoton ionisation of rare gases by a co2 laser: electron spectroscopy. *Journal of Physics B: Atomic, Molecular and Optical Physics*, 21(7):L159, 1988.

[23] P Agostini, P Breger, A L'huillier, HG Muller, G Petite, A Antonetti, and A Migus. Giant stark shifts in multiphoton ionization. *Physical review letters*, 63(20):2208, 1989.

[24] RR Freeman and PH Bucksbaum. Investigations of above-threshold ionization using subpicosecond laser pulses. *Journal of Physics B: Atomic, Molecular and Optical Physics*, 24(2):325, 1991.

[25] Philip H Bucksbaum, Richard R Freeman, M Bashkansky, and Thomas J McIlrath. Role of the ponderomotive potential in above-threshold ionization. *JOSA B*, 4(5):760–764, 1987.

[26] RR Freeman, PH Bucksbaum, H Milchberg, S Darack, D Schumacher, and ME Geusic. Above-threshold ionization with subpicosecond laser pulses. *Physical review letters*, 59(10):1092, 1987.

[27] LV Keldysh et al. Ionization in the field of a strong electromagnetic wave. *Sov. Phys. JETP*, 20(5):1307–1314, 1965.

[28] M Okunishi, Toru Morishita, G Prümper, K Shimada, CD Lin, S Watanabe, and K Ueda. Experimental retrieval of target structure information from laser-induced rescattered photoelectron momentum distributions. *Physical review letters*, 100(14):143001, 2008.

[29] K Burnett, VC Reed, and PL Knight. Atoms in ultra-intense laser fields. *Journal of Physics B: Atomic, Molecular and Optical Physics*, 26(4):561, 1993.

[30] Farhad HM Faisal. Multiple absorption of laser photons by atoms. *Journal of Physics B: Atomic and Molecular Physics*, 6(4):L89, 1973.

[31] Howard R Reiss. Effect of an intense electromagnetic field on a weakly bound system. *Physical Review A*, 22(5):1786, 1980.

[32] Thomas Brabec and Ferenc Krausz. Intense few-cycle laser fields: Frontiers of nonlinear optics. *Reviews of Modern Physics*, 72(2):545, 2000.

[33] AM Perelomov, VS Popov, and MV Terent'Ev. Ionization of atoms in an alternating electric field. *Sov. Phys. JETP*, 23(5):924–934, 1966.

[34] Maxim V Ammosov. Tunnel ionization of complex atoms and of atomic ions in an altemating electromagnetic field. *Sov. Phys. JETP*, 64:1191, 1987.

[35] PB Corkum, NH Burnett, and F Brunel. Above-threshold ionization in the long-wavelength limit. *Physical review letters*, 62(11):1259, 1989.

[36] Paul B Corkum. Plasma perspective on strong field multiphoton ionization. *Physical review letters*, 71(13):1994, 1993.

[37] U Mohideen, MH Sher, HWK Tom, GD Aumiller, II OR Wood, RR Freeman, J Boker, and PH Bucksbaum. High intensity above-threshold ionization of he. *Physical review letters*, 71(4):509, 1993.

[38] L Arissian, C Smeenk, F Turner, C Trallero, AV Sokolov, DM Villeneuve, A Staudte, and PB Corkum. Direct test of laser tunneling with electron momentum imaging. *Physical review letters*, 105(13):133002, 2010.

[39] LD Landau. Quantum mechanics 2nd edn (moscow: Fizmatlit) landau ld and lifshits em 1965 quantum mechanics, 1963.

[40] BM Smirnov and MI Chibisov. The breaking up of atomic particles by an electric field and by electron collisions. *Sov. Phys. JETP*, 22(585):23, 1966.

[41] Vladimir S Popov. Tunnel and multiphoton ionization of atoms and ions in a strong laser field (keldysh theory). *Physics-Uspekhi*, 47(9):855, 2004.

[42] Douglas R Hartree. The wave mechanics of an atom with a non-coulomb central field. part i. theory and methods. In *Mathematical Proceedings of the Cambridge Philosophical Society*, volume 24, pages 89–110. Cambridge university press, 1928.

[43] NB Delone and Vladimir P Krainov. Energy and angular electron spectra for the tunnel ionization of atoms by strong low-frequency radiation. *JOSA B*, 8(6):1207–1211, 1991.

[44] Nikolaj B Delone, Vladimir Pavlovich Krainov, and EM Yankovsky. Atoms in strong light fields. *Springer series in chemical physics*, 28, 1985.

[45] Vladimir P Krainov. Ionization rates and energy and angular distributions at the barrier-suppression ionization of complex atoms and atomic ions. *JOSA B*, 14(2):425–431, 1997.

[46] Bambi HuP, Jie Liu, and Shi-gang Chen. Plateau in above-threshold-ionization spectra and chaotic behavior in rescattering processes. *Physics Letters A*, 236(5-6):533–542, 1997.

[47] J Chen, J Liu, and SG Chen. Rescattering effect on phase-dependent ionization of atoms in two-color intense fields. *Physical Review A*, 61(3):033402, 2000.

[48] SV Popruzhenko. Keldysh theory of strong field ionization: history, applications, difficulties and perspectives. *Journal of Physics B: Atomic, Molecular and Optical Physics*, 47(20):204001, 2014.

[49] MV Frolov, NL Manakov, AA Silaev, and NV Vvedenskii. Analytic description of high-order harmonic generation by atoms in a two-color laser field. *Physical Review A*, 81(6):063407, 2010.

[50] MV Frolov, DV Knyazeva, NL Manakov, Ji-Wei Geng, Liang-You Peng, and Anthony F Starace. Analytic model for the description of above-threshold ionization by an intense short laser pulse. *Physical Review A*, 89(6):063419, 2014.

[51] Niranjan Shivaram, Henry Timmers, Xiao-Min Tong, and Arvinder Sandhu. Attosecond-resolved evolution of a laser-dressed helium atom: interfering excitation paths and quantum phases. *Physical review letters*, 108(19):193002, 2012.

[52] Shih-I Chu and Dmitry A Telnov. Beyond the floquet theorem: generalized floquet formalisms and quasienergy methods for atomic and molecular multiphoton processes in intense laser fields. *Physics reports*, 390(1-2):1–131, 2004.

[53] N Douguet, TN Rescigno, and AE Orel. Carbon-k-shell molecular-frame photoelectron angular distributions in the photoisomerization of neutral ethylene. *Physical Review A*, 88(1):013412, 2013.

[54] I Barth, L Friedland, O Gat, and AG Shagalov. Quantum versus classical phase-locking transition in a frequency-chirped nonlinear oscillator. *Physical Review A*, 84(1):013837, 2011.

[55] Walter Gordon. Der comptoneffekt nach der schrödingerschen theorie. *Zeitschrift für Physik*, 40(1-2):117–133, 1926.

[56] Daniil M Wolkow. Über eine klasse von lösungen der diracschen gleichung. *Zeitschrift für Physik*, 94(3-4):250–260, 1935.

[57] DM Volkov. Electron in the field of plane unpolarized electromagnetic waves from the standpoint of the dirac equation. *Zh. Eksp. Teor. Fiz*, 7:1286–1289, 1937.

[58] Vladimir Borisovich Berestetskii, Evgenii Mikhailovich Lifshitz, and Lev Petrovich Pitaevskii. *Quantum Electrodynamics: Volume 4*, volume 4. Butterworth-Heinemann, 1982.

[59] W Becker, Felix Grasbon, R Kopold, DB Milošević, GG Paulus, and Herbert Walther. Above-threshold ionization: From classical features to quantum effects. *Advances in Atomic Molecular and Optical Physics*, 48:35–98, 2002.

[60] N Bleistein and RA Handelsman. Asymptotic expansions of integrals, ser, 1986.

[61] GF Gribakin and M Yu Kuchiev. Multiphoton detachment of electrons from negative ions. *Physical Review A*, 55(5):3760, 1997.

[62] Maciej Lewenstein, Ph Balcou, M Yu Ivanov, Anne L'huillier, and Paul B Corkum. Theory of high-harmonic generation by low-frequency laser fields. *Physical Review A*, 49(3):2117, 1994.

[63] C Figueira de Morisson Faria, H Schomerus, and W Becker. High-order above-threshold ionization: The uniform approximation and the effect of the binding potential. *Physical review a*, 66(4):043413, 2002.

[64] DB Milošević, GG Paulus, D Bauer, and W Becker. Above-threshold ionization by few-cycle pulses. *Journal of Physics B: Atomic, Molecular and Optical Physics*, 39(14):R203, 2006.

[65] SV Popruzhenko, VD Mur, VS Popov, and D Bauer. Strong field ionization rate for arbitrary laser frequencies. *Physical review letters*, 101(19):193003, 2008.

[66] Min Li, Ji-Wei Geng, Hong Liu, Yongkai Deng, Chengyin Wu, Liang-You Peng, Qihuang Gong, and Yunquan Liu. Classical-quantum correspondence for above-threshold ionization. *Physical review letters*, 112(11):113002, 2014.

[67] Ji-Wei Geng, Liang Qin, Min Li, Wei-Hao Xiong, Yunquan Liu, Qihuang Gong, and Liang-You Peng. Nonadiabatic tunneling ionization of atoms in elliptically polarized laser fields. *Journal of Physics B: Atomic, Molecular and Optical Physics*, 47(20):204027, 2014.

[68] T Nubbemeyer, K Gorling, A Saenz, U Eichmann, and W Sandner. Strong-field tunneling without ionization. *Physical review letters*, 101(23):233001, 2008.

[69] NI Shvetsov-Shilovski, SP Goreslavski, SV Popruzhenko, and W Becker. Capture into rydberg states and momentum distributions of ionized electrons. *Laser physics*, 19(8):1550–1558, 2009.

[70] NI Shvetsov-Shilovski, D Dimitrovski, and LB Madsen. Ionization in elliptically polarized pulses: Multielectron polarization effects and asymmetry of photoelectron momentum distributions. *Physical Review A*, 85(2):023428, 2012.

[71] Richard Phillips Feynman. Space-time approach to quantum electrodynamics. *Physical Review*, 76(6):769, 1949.

[72] Pascal Salières, B Carré, L Le Déroff, F Grasbon, GG Paulus, H Walther, R Kopold, W Becker, DB Milošević, A Sanpera, et al. Feynman's path-integral approach for intense-laser-atom interactions. *Science*, 292(5518):902–905, 2001.

[73] NI Shvetsov-Shilovski, Manfred Lein, LB Madsen, E Räsänen, C Lemell, J Burgdörfer, DG Arbó, and K Tőkési. Semiclassical two-step model for strong-field ionization. *Physical Review A*, 94(1):013415, 2016.

[74] P Agostini and LF DiMauro. Atoms in high intensity mid-infrared pulses. *Contemporary Physics*, 49(3):179–197, 2008.

[75] eg PA Franken, Alan E Hill, CW Peters, and Gabriel Weinreich. Generation of optical harmonics. *Physical Review Letters*, 7(4):118, 1961.

[76] A McPherson, G Gibson, H Jara, U Johann, Ting S Luk, IA McIntyre, Keith Boyer, and Charles K Rhodes. Studies of multiphoton production of vacuum-ultraviolet radiation in the rare gases. *JOSA B*, 4(4):595–601, 1987.

[77] Jeffrey L Krause, Kenneth J Schafer, and Kenneth C Kulander. High-order harmonic generation from atoms and ions in the high intensity regime. *Physical Review Letters*, 68(24):3535, 1992.

[78] Pierre Agostini and Louis F DiMauro. The physics of attosecond light pulses. *Reports on progress in physics*, 67(6):813, 2004.

[79] Ferenc Krausz and Misha Ivanov. Attosecond physics. *Reviews of modern physics*, 81(1):163, 2009.

[80] P áB Corkum and Ferenc Krausz. Attosecond science. *Nature physics*, 3(6):381–387, 2007.

[81] Carsten Winterfeldt, Christian Spielmann, and Gustav Gerber. Colloquium: Optimal control of high-harmonic generation. *Reviews of Modern Physics*, 80(1):117, 2008.

[82] Emily A Gibson, Ariel Paul, Nick Wagner, Ra'anan Tobey, David Gaudiosi, Sterling Backus, Ivan P Christov, Andy Aquila, Eric M Gullikson, David T Attwood, et al. Coherent soft x-ray generation in the water window with quasi-phase matching. *Science*, 302(5642):95–98, 2003.

[83] Eiji J Takahashi, Tsuneto Kanai, Kenichi L Ishikawa, Yasuo Nabekawa, and Katsumi Midorikawa. Coherent water window x ray by phase-matched high-order harmonic generation in neutral media. *Physical Review Letters*, 101(25):253901, 2008.

[84] Eleftherios Goulielmakis, Martin Schultze, M Hofstetter, Vladislav S Yakovlev, Justin Gagnon, M Uiberacker, Andrew L Aquila, EM Gullikson, David T Attwood, Reinhard Kienberger, et al. Single-cycle nonlinear optics. *Science*, 320(5883):1614–1617, 2008.

[85] Jiro Itatani, Jérôme Levesque, Dirk Zeidler, Hiromichi Niikura, Henri Pépin, Jean-Claude Kieffer, Paul B Corkum, and David M Villeneuve. Tomographic imaging of molecular orbitals. *Nature*, 432(7019):867–871, 2004.

[86] Anne L'Huillier, LA Lompre, G Mainfray, and C Manus. Multiply charged ions induced by multiphoton absorption in rare gases at 0.53 μm. *Physical Review A*, 27(5):2503, 1983.

[87] David N Fittinghoff, Paul R Bolton, Britton Chang, and Kenneth C Kulander. Observation of nonsequential double ionization of helium with optical tunneling. *Physical review letters*, 69(18):2642, 1992.

[88] Barry Walker, Brian Sheehy, Louis F DiMauro, Pierre Agostini, Kenneth J Schafer, and Kenneth C Kulander. Precision measurement of strong field double ionization of helium. *Physical review letters*, 73(9):1227, 1994.

[89] M Yu Kuchiev. Ati as a source for multiply charged ion production in a laser field. *Journal of Physics B: Atomic, Molecular and Optical Physics*, 28(23):5093, 1995.

[90] Ullrich Eichmann, Martin Dörr, W Becker, M Dammasch, and Wolfgang Sandner. Collective multi-electron tunneling ionization in strong fields. In *AIP Conference Proceedings*, volume 525, pages 199–210. American Institute of Physics, 2000.

[91] Th Weber, Matthias Weckenbrock, Andre Staudte, Lutz Spielberger, Ottmar Jagutzki, Volker Mergel, Feras Afaneh, Gunter Urbasch, Martin Vollmer, Harald Giessen, et al. Recoil-ion momentum distributions for single and double ionization of helium in strong laser fields. *Physical review letters*, 84(3):443, 2000.

[92] Robert Moshammer, Bernold Feuerstein, Wolfgang Schmitt, Alexander Dorn, Claus D Schröter, Joachim Ullrich, Horst Rottke, Christoph Trump, Michael Wittmann, Georg Korn, et al. Momentum distributions of ne n+ ions created by an intense ultrashort laser pulse. *Physical review letters*, 84(3):447, 2000.

[93] Richard Kopold, Wilhelm Becker, Horst Rottke, and Wolfgang Sandner. Routes to nonsequential double ionization. *Physical review letters*, 85(18):3781, 2000.

[94] Bernold Feuerstein, Robert Moshammer, Daniel Fischer, Alexander Dorn, Claus D Schröter, Jens Deipenwisch, JR Crespo Lopez-Urrutia, Cornelia Höhr, Paul Neumayer, Joachim Ullrich, et al. Separation of recollision mechanisms in nonsequential strong field double ionization of ar: the role of excitation tunneling. *Physical review letters*, 87(4):043003, 2001.

[95] A.-T. Le M. Baudisch M. Hemmer A. Senftleben C. D. Schröter J. Ullrich R. Moshammer CD Lin M. G. Pullen, B. Wolter and J. Biegert. Laser-induced electron diffraction to image molecular structure. *Optics and Photonics News*, December 2015.

[96] Junliang Xu, Zhangjin Chen, Anh-Thu Le, and CD Lin. Self-imaging of molecules from diffraction spectra by laser-induced rescattering electrons. *Physical Review A*, 82(3):033403, 2010.

[97] Zhangjin Chen, Anh-Thu Le, Toru Morishita, and CD Lin. Quantitative rescattering theory for laser-induced high-energy plateau photoelectron spectra. *Physical Review A*, 79(3):033409, 2009.

[98] William Henry Bragg and William Lawrence Bragg. The reflection of x-rays by crystals. *Proceedings of the Royal Society of London. Series A, Containing Papers of a Mathematical and Physical Character*, 88(605):428–438, 1913.

[99] Henry Gwyn Jeffreys Moseley. Xciii. the high-frequency spectra of the elements. *The London, Edinburgh, and Dublin Philosophical Magazine and Journal of Science*, 26(156):1024–1034, 1913.

[100] Gérard A Mourou and Victor Yanovsky. Relativistic optics: a gateway to attosecond physics. *Optics and photonics news*, 15(5):40–45, 2004.

[101] S-W Bahk, Pascal Rousseau, TA Planchon, Vladimir Chvykov, Galina Kalintchenko, Anatoly Maksimchuk, GA Mourou, and Victor Yanovsky. Generation and characterization of the highest laser intensities (10 22 w/cm 2). *Optics letters*, 29(24):2837–2839, 2004.

[102] Arthur L Schawlow and Charles H Townes. Infrared and optical masers. *Physical Review*, 112(6):1940, 1958.

[103] Willis E Lamb Jr. Theory of an optical maser. *Physical Review*, 134(6A):A1429, 1964.

[104] LE Hargrove, Richard L Fork, and MA Pollack. Locking of he–ne laser modes induced by synchronous intracavity modulation. *Applied Physics Letters*, 5(1):4–5, 1964.

[105] RL Fork, CV Shank, C Hirlimann, R Yen, and WJ Tomlinson. Femtosecond white-light continuum pulses. *Optics letters*, 8(1):1–3, 1983.

[106] David E Spence, P Np Kean, and Wilson Sibbett. 60-fsec pulse generation from a self-mode-locked ti: sapphire laser. *Optics letters*, 16(1):42–44, 1991.

[107] J Aus Der Au, D Kopf, F Morier-Genoud, M Moser, and U Keller. 60-fs pulses from a diode-pumped nd: glass laser. *Optics letters*, 22(5):307–309, 1997.

[108] DJ Ripin, C Chudoba, JT Gopinath, JG Fujimoto, EP Ippen, U Morgner, FX Kärtner, V Scheuer, G Angelow, and T Tschudi. Generation of 20-fs pulses by a prismless cr 4+: Yag laser. *Optics letters*, 27(1):61–63, 2002.

[109] Philipp Wagenblast, Richard Ell, Uwe Morgner, Felix Grawert, and Franz X Kärtner. Diode-pumped 10-fs cr 3+: Licaf laser. *Optics letters*, 28(18):1713–1715, 2003.

[110] Franz X Kärtner and Franz X Kärtner. *Few-cycle laser pulse generation and its applications*, volume 95. Springer Science & Business Media, 2004.

[111] Donna Strickland and GerardMourou. Compression of amplified chirped optical pulses. *Optics Communications*, 55(6):447–449, 1985.

[112] Eiichi Matsubara, Keisaku Yamane, Taro Sekikawa, and Mikio Yamashita. Generation of 2.6 fs optical pulses using induced-phase modulation in a gas-filled hollow fiber. *JOSA B*, 24(4):985–989, 2007.

[113] Akira Suda, Masatoshi Hatayama, Keigo Nagasaka, and Katsumi Midorikawa. Generation of sub-10-fs, 5-mj-optical pulses using a hollow fiber with a pressure gradient. *Applied Physics Letters*, 86(11):111116, 2005.

[114] Muhammad Nurhuda, Akira Suda, Katsumi Midorikawa, Masatoshi Hatayama, and Keigo Nagasaka. Propagation dynamics of femtosecond laser pulses in a hollow fiber filled with argon: constant gas pressure versus differential gas pressure. *JOSA B*, 20(9):2002–2011, 2003.

[115] Samuel Bohman, Akira Suda, Tsuneto Kanai, Shigeru Yamaguchi, and Katsumi Midorikawa. Generation of 5.0 fs, 5.0 mj pulses at 1khz using hollow-fiber pulse compression. *Optics letters*, 35(11):1887–1889, 2010.

[116] SE Harris, MK Oshman, and RL Byer. Observation of tunable optical parametric fluorescence. *Physical Review Letters*, 18(18):732, 1967.

[117] Robert W Boyd. *Nonlinear optics*. Academic press, 2020.

[118] Giulio Cerullo and Sandro De Silvestri. Ultrafast optical parametric amplifiers. *Review of scientific instruments*, 74(1):1–18, 2003.

[119] Stefan Witte and Kjeld SE Eikema. Ultrafast optical parametric chirped-pulse amplification. *IEEE Journal of Selected Topics in Quantum Electronics*, 18(1):296–307, 2011.

[120] A Dubietis, G Jonušauskas, and A Piskarskas. Powerful femtosecond pulse generation by chirped and stretched pulse parametric amplification in bbo crystal. *Optics Communications*, 88(4-6):437–440, 1992.

[121] IN Ross, P Matousek, M Towrie, AJ Langley, and JL Collier. The prospects for ultrashort pulse duration and ultrahigh intensity using optical parametric chirped pulse amplifiers. *Optics Communications*, 144(1-3):125–133, 1997.

[122] Benjamin Wolter. Electron re-collision dynamics in strong mid-ir fields for diffraction imaging of molecular structure and its fragmentation. 2018.

[123] Benjamin Erk. *Fragmentation dynamics of small molecules upon multiple ionization by x-ray free-electron laser pulses*. PhD thesis, Ruprecht-Karls-Universität Heidelberg, 2013.

[124] WC Wiley and Ii H McLaren. Time-of-flight mass spectrometer with improved resolution. *Review of scientific instruments*, 26(12):1150–1157, 1955.

[125] Tobias Unruh, Jürgen Neuhaus, and Winfried Petry. The high-resolution time-of-flight spectrometer toftof. *Nuclear Instruments and Methods in Physics Research Section A: Accelerators, Spectrometers, Detectors and Associated Equipment*, 580(3):1414–1422, 2007.

[126] JM Budarz, MP Minitti, DV Cofer-Shabica, B Stankus, Adam Kirrander, JB Hastings, and PM Weber. Observation of femtosecond molecular dynamics via pump–probe gas phase x-ray scattering. *Journal of Physics B: Atomic, Molecular and Optical Physics*, 49(3):034001, 2016.

[127] Jie Yang, Markus Guehr, Theodore Vecchione, Matthew S Robinson, Renkai Li, Nick Hartmann, Xiaozhe Shen, Ryan Coffee, Jeff Corbett, Alan Fry, et al. Diffractive imaging of a rotational wavepacket in nitrogen molecules with femtosecond megaelectronvolt electron pulses. *Nature communications*, 7(1):1–9, 2016.

[128] beam MeV-UED. beam MeV-UED. `https://lcls.slac.stanford.edu/instruments/mev-ued/specifications/`. [Online; accessed 19-Sep-2021].

[129] Ray C Dudek and Peter M Weber. Ultrafast diffraction imaging of the electrocyclic ring-opening reaction of 1, 3-cyclohexadiene. *The Journal of Physical Chemistry A*, 105(17):4167–4171, 2001.

[130] Lingyu Ma, Haiwang Yong, Joseph D Geiser, Andrés Moreno Carrascosa, Nathan Goff, and Peter M Weber. Ultrafast x-ray and electron scattering of free molecules: A comparative evaluation. *Structural Dynamics*, 7(3):034102, 2020.

[131] Bradley J Siwick, Jason R Dwyer, Robert E Jordan, and RJ Dwayne Miller. An atomic-level view of melting using femtosecond electron diffraction. *Science*, 302(5649):1382–1385, 2003.

[132] U Heugen, G Schwaab, E Bründermann, M Heyden, X Yu, DM Leitner, and Martina Havenith. Solute-induced retardation of water dynamics probed directly by terahertz spectroscopy. *Proceedings of the National Academy of Sciences*, 103(33):12301–12306, 2006.

[133] Federico Sebastiani, Stefan LP Wolf, Benjamin Born, Trung Quan Luong, Helmut Cölfen, Denis Gebauer, and Martina Havenith. Water dynamics from thz spectroscopy reveal the locus of a liquid–liquid binodal limit in aqueous caco3 solutions. *Angewandte Chemie International Edition*, 56(2):490–495, 2017.

[134] Luyuan Zhang, Lijuan Wang, Ya-Ting Kao, Weihong Qiu, Yi Yang, Oghaghare Okobiah, and Dongping Zhong. Mapping hydration dynamics around a protein surface. *Proceedings of the National Academy of Sciences*, 104(47):18461–18466, 2007.

[135] Sudipta Kumar Sinha, Sudip Chakraborty, and Sanjoy Bandyopadhyay. Thickness of the hydration layer of a protein from molecular dynamics simulation. *The Journal of Physical Chemistry B*, 112(27):8203–8209, 2008.

[136] Simon Ebbinghaus, Seung Joong Kim, Matthias Heyden, Xin Yu, Udo Heugen, Martin Gruebele, David M Leitner, and Martina Havenith. An extended dynamical hydration shell around proteins. *Proceedings of the National Academy of Sciences*, 104(52):20749–20752, 2007.

[137] Richard N Zare. Laser control of chemical reactions. *science*, 279(5358):1875–1879, 1998.

[138] George C Schatz, Mitchell C Colton, and John L Grant. A quasiclassical trajectory study of the state-to-state dynamics of atomic hydrogen+ water. fwdarw. hydroxyl+ molecular hydrogen. *The Journal of Physical Chemistry*, 88(14):2971–2977, 1984.

[139] Kim A Sharp, Bhupinder Madan, Eric Manas, and Jane M Vanderkooi. Water structure changes induced by hydrophobic and polar solutes revealed by simulations and infrared spectroscopy. *The Journal of Chemical Physics*, 114(4):1791–1796, 2001.

[140] GT Gao, KJ Oh, and Xiao Cheng Zeng. Effect of uniform electric field on homogeneous vapor–liquid nucleation and phase equilibria. ii. extended simple point charge model water. *The Journal of chemical physics*, 110(5):2533–2538, 1999.

[141] Dong Hyun Jung, Jung Hwan Yang, and Mu Shik Jhon. The effect of an external electric field on the structure of liquid water using molecular dynamics simulations. *Chemical physics*, 244(2-3):331–337, 1999.

[142] Shun-Ping Shi, Quan Zhang, Li Zhang, Rong Wang, Zheng-He Zhu, Gang Jiang, Yi-Bei Fu, et al. Geometrical structures, vibrational frequencies, force constants and dissociation energies of isotopic water molecules (h 2 o, hdo, d 2 o, hto, dto, and t 2 o) under dipole electric field. 2011.

[143] Junliang Xu, Cosmin I Blaga, Kaikai Zhang, Yu Hang Lai, CD Lin, Terry A Miller, Pierre Agostini, and Louis F DiMauro. Diffraction using laser-driven broadband electron wave packets. *Nature communications*, 5(1):1–6, 2014.

[144] M. G. Pullen, B. Wolter, A. T. Le, M. Baudisch, M. Sclafani, H. Pires, C. D. Schröter, J. Ullrich, R. Moshammer, T. Pfeifer, C. D. Lin, and J. Biegert. Influence of orbital symmetry on diffraction imaging with rescattering electron wave packets. *Nature Communications*, 7(1):11922, 2016.

[145] JB Hasted. Liquid water: Dielectric properties. In *The Physics and Physical Chemistry of Water*, pages 255–309. Springer, 1972.

[146] G Brasen, M Leidecker, W Demtröder, T Shimamoto, and H Kato. New vibrational analysis of the 1 b 2 (1 δ u) state of cs 2. *The Journal of chemical physics*, 109(7):2779–2790, 1998.

[147] Joachim Ullrich, Robert Moshammer, Alexander Dorn, Reinhard Dorner, L Ph H Schmidt, and H Schmidt-Bocking. Recoil-ion and electron momentum spectroscopy: reaction-microscopes. *Reports on Progress in Physics*, 66(9):1463, 2003.

[148] Alan V Oppenheim, John R Buck, and Ronald W Schafer. *Discrete-time signal processing. Vol. 2.* Upper Saddle River, NJ: Prentice Hall, 2001.

[149] Attila G Császár, Gábor Czakó, Tibor Furtenbacher, Jonathan Tennyson, Viktor Szalay, Sergei V Shirin, Nikolai F Zobov, and Oleg L Polyansky. On equilibrium structures of the water molecule. *The Journal of chemical physics*, 122(21):214305, 2005.

[150] Jaime Suárez, L Méndez, and I Rabadán. Nonadiabatic fragmentation of h 2 o+ and isotopomers. wave packet propagation using ab initio wavefunctions. *Physical Chemistry Chemical Physics*, 20(45):28511–28522, 2018.

[151] CG Ning, B Hajgató, YR Huang, SF Zhang, K Liu, ZH Luo, S Knippenberg, JK Deng, and MS Deleuze. High resolution electron momentum spectroscopy of the valence orbitals of water. *Chemical Physics*, 343(1):19–30, 2008.

[152] Simon Petretti, Alejandro Saenz, Alberto Castro, and Piero Decleva. Water molecules in ultrashort intense laser fields. *Chemical Physics*, 414:45–52, 2013.

[153] TR Huet, CJ Pursell, WC Ho, BM Dinelli, and T Oka. Infrared spectroscopy and equilibrium structure of h2o+ (x 2 b 1). *The Journal of chemical physics*, 97(9):5977–5987, 1992.

[154] Kirk A Peterson, David E Woon, and Thom H Dunning Jr. Benchmark calculations with correlated molecular wave functions. iv. the classical barrier height of the h+ h2→ h2+ h reaction. *The Journal of chemical physics*, 100(10):7410–7415, 1994.

[155] Harry H Ku et al. Notes on the use of propagation of error formulas. *Journal of Research of the National Bureau of Standards*, 70(4):263–273, 1966.

[156] Shenghai Wu, Yangqin Chen, Xiaohua Yang, Yingchun Guo, Yuyan Liu, Yan Li, Robert J Buenker, and Per Jensen. Vibronic transition moments and line intensities for h2o+. *Journal of Molecular Spectroscopy*, 225(1):96–106, 2004.

[157] Frank J Lovas. Microwave spectral tables ii. triatomic molecules. *Journal of Physical and Chemical Reference Data*, 7(4):1445–1750, 1978.

[158] Sifiso M Nkambule, Åsa Larson, Samantha Fonseca dos Santos, and Ann E Orel. Theoretical study of the mechanism of h 2 o+ dissociative recombination. *Physical Review A*, 92(1):012708, 2015.

[159] Giacinto Scoles. *Atomic and molecular beam methods*. Oxford university press, 1988.

[160] Cornelia G Heid, Victoria Walpole, Mark Brouard, Pablo G Jambrina, and F Javier Aoiz. Side-impact collisions of ar with no. *Nature chemistry*, 11(7):662–668, 2019.

[161] Michael D Morse. Supersonic beam sources. *Experimental methods in the physical sciences*, 29:21–47, 1996.

[162] Sebastiaan YT Van De Meerakker, Hendrick L Bethlem, and Gerard Meijer. Taming molecular beams. *Nature Physics*, 4(8):595–602, 2008.

[163] Uzi Even. The even-lavie valve as a source for high intensity supersonic beam. *EPJ Techniques and Instrumentation*, 2:1–22, 2015.

[164] David R Lide. *CRC handbook of chemistry and physics*, volume 85. CRC press, 2004.

[165] TQ Truong and NT Nguyen. Simulation and optimization of tesla valves. *Nanotech*, 1:178–181, 2003.

[166] SF De Vries, D Florea, FGA Homburg, and AJH Frijns. Design and operation of a tesla-type valve for pulsating heat pipes. *International Journal of Heat and Mass Transfer*, 105:1–11, 2017.

[167] AY Nobakht, M Shahsavan, and A Paykani. Numerical study of diodicity mechanism in different tesla-type microvalves. *Journal of applied research and technology*, 11(6):876–885, 2013.

[168] Piyush R Porwal, Scott M Thompson, D Keith Walters, and Tausif Jamal. Heat transfer and fluid flow characteristics in multistaged tesla valves. *Numerical Heat Transfer, Part A: Applications*, 73(6):347–365, 2018.

[169] K Mohammadzadeh, EM Kolahdouz, E Shirani, and MB Shafii. Numerical investigation on the effect of the size and number of stages on the tesla microvalve efficiency. *Journal of Mechanics*, 29(3):527–534, 2013.

[170] Scott M Thompson, BJ Paudel, T Jamal, and DK Walters. Numerical investigation of multistaged tesla valves. *Journal of Fluids Engineering*, 136(8), 2014.

[171] JP Maier and DW Turner. Steric inhibition of resonance studied by molecular photoelectron spectroscopy. part 2.—phenylethylenes. *Journal of the Chemical Society, Faraday Transactions 2: Molecular and Chemical Physics*, 69:196–206, 1973.

[172] OpenCFD. Release OpenFOAM® v2006. `http://www.openfoam.com.` [Online; accessed 19-Sep-2021].

[173] Michael J Pratt et al. Introduction to iso 10303—the step standard for product data exchange. *Journal of Computing and Information Science in Engineering*, 1(1):102–103, 2001.

[174] Warren S McCulloch and Walter Pitts. A logical calculus of the ideas immanent in nervous activity. *The bulletin of mathematical biophysics*, 5(4):115–133, 1943.

[175] BWAC Farley and W Clark. Simulation of self-organizing systems by digital computer. *Transactions of the IRE Professional Group on Information Theory*, 4(4):76–84, 1954.

[176] Nathaniel Rochester, J Holland, L Haibt, and WJIToiT Duda. Tests on a cell assembly theory of the action of the brain, using a large digital computer. *IRE Transactions on information Theory*, 2(3):80–93, 1956.

[177] Frank Rosenblatt. The perceptron: a probabilistic model for information storage and organization in the brain. *Psychological review*, 65(6):386, 1958.

[178] Stuart Dreyfus. The computational solution of optimal control problems with time lag. *IEEE Transactions on Automatic Control*, 18(4):383–385, 1973.

[179] Paul J Werbos. Applications of advances in nonlinear sensitivity analysis. In *System modeling and optimization*, pages 762–770. Springer, 1982.

[180] Carver Mead and Mohammed Ismail. *Analog VLSI implementation of neural systems*, volume 80. Springer Science & Business Media, 2012.

[181] Quoc V Le. Building high-level features using large scale unsupervised learning. In *2013 IEEE international conference on acoustics, speech and signal processing*, pages 8595–8598. IEEE, 2013.

[182] Ian Goodfellow, Yoshua Bengio, and Aaron Courville. *Deep learning*. MIT press, 2016.

[183] Serge Tabachnikov. *Arnold: Swimming Against the Tide*. American Mathematical Society., 2014.

[184] Shigeo Akashi. Application of entropy theory to kolmogorov—arnold representation theorem. *Reports on Mathematical Physics*, 48(1-2):19–26, 2001.

[185] István Hargittai and Magdolna Hargittai. *Stereochemical applications of gas-phase electron diffraction*. VCH, 1988.

[186] Francesc Salvat, Aleksander Jablonski, and Cedric J Powell. Elsepa—dirac partial-wave calculation of elastic scattering of electrons and positrons by atoms, positive ions and molecules. *Computer physics communications*, 165(2):157–190, 2005.

[187] Cosmin I Blaga, Junliang Xu, Anthony D DiChiara, Emily Sistrunk, Kaikai Zhang, Pierre Agostini, Terry A Miller, Louis F DiMauro, and CD Lin. Imaging ultrafast molecular dynamics with laser-induced electron diffraction. *Nature*, 483(7388):194–197, 2012.

[188] Michael G. Pullen, Benjamin Wolter, Anh-Thu Le, Matthias Baudisch, Michaël Hemmer, Arne Senftleben, Claus Dieter Schröter, Joachim Ullrich, Robert Moshammer, C. D. Lin, and Jens Biegert. Imaging an aligned polyatomic molecule with laser-induced electron diffraction. *Nature Communications*, 6(1):7262, 2015.

[189] Benjamin Wolter, Michael G Pullen, Matthias Baudisch, Michele Sclafani, Michaël Hemmer, Arne Senftleben, Claus Dieter Schröter, Joachim Ullrich, Robert Moshammer, and Jens Biegert. Strong-field physics with mid-ir fields. *Physical Review X*, 5(2):021034, 2015.

[190] Kasra Amini, Michele Sclafani, Tobias Steinle, Anh-Thu Le, Aurelien Sanchez, Carolin Müller, Johannes Steinmetzer, Lun Yue, José Ramón Martínez Saavedra, Michaël Hemmer, et al. Imaging the renner–teller effect using laser-induced electron diffraction. *Proceedings of the National Academy of Sciences*, 116(17):8173–8177, 2019.